

Copyright

by

Uttiya Chowdhury

2002

The Dissertation Committee for Uttiya Chowdhury  
certifies that this is the approved version of the following dissertation:

# **MOCVD Growth for UV Photodetectors and Light Emitting Diodes**

Committee:

---

Russell D. Dupuis, Supervisor

---

Joe C. Campbell

---

Nathan F. Gardner

---

John B. Goodenough

---

Leonard F. Register

# **MOCVD Growth for UV Photodetectors and Light Emitting Diodes**

by

**Uttiya Chowdhury, B.Sc.Engg., M.S.**

## **Dissertation**

Presented to the Faculty of the Graduate School of

The University of Texas at Austin

in Partial Fulfillment

of the Requirements

for the Degree of

**Doctor of Philosophy**

**The University of Texas at Austin**

December 2002

To my parents: Urna and Tapan

# Acknowledgments

I would like to express my gratitude to those who have helped make this work possible. First, I thank my advisor, Professor Russell Dupuis, for his guidance and for giving me the opportunity to participate in research in his laboratory. I would also like to thank Professor Joe Campbell and Professor Leonard Register for useful discussions throughout the years.

I have had the privilege of the guidance from some very knowledgeable researchers — I would like to thank Dr. Chris Eiting, Dr. Paul Grudowski, Dr. Adrian Holmes, Dr. Ki-Soo Kim, Dr. Ho-Ki Kwon, Dr. Damien Lambert, Dr. Joongseo Park, Dr. Jae-Hyun Ryou, Yuichi Sasajima, Dr. Bryan Shelton, Dr. Delphine Sicault, and Dr. Xuebing Zhang for the theoretical and operational knowledge they have shared with me. I would also like to mention the remaining members of the MOCVD research group with whom I have had the pleasure of working: Jin-Ho Choi, Jonathan Denyszyn, Mathilde Gobet, Richard Heller, Min-Soo Noh, Michael Wong, Dongwon Yoo, and Ting Gang Zhu. I especially appreciate the diligent assistance and sincere cooperation of the current members of the nitride team: Dr. Sicault, Michael, Ting

Gang, Jonathan, Jin-Ho, and Dongwon — without them, I could not have accomplished this dissertation.

I thank the staff at the Microelectronics and Engineering Research Building — Joyce Kokes, Donna Larson and Steve Moore in the purchasing and receiving department, Jean Toll in administrative department, and William Fordyce, James Hitzfelder, Jesse James, Terry Mattord, Elton Sakevitz, Steve Schaper and Robert Stephens in the maintenance department — for providing me with a seamless work environment while they handled all the ancillary activities. I also thank Dana Dupuis for her assistance with preparing this dissertation as well as all of my other publications.

Many collaborators have contributed to the body of the work presented here. Two research teams have contributed significantly to the success of the UV photodetector work presented here. Professor Joe Campbell and his students — Ariane Beck, Dr. Charles Collins, Xiangyi Guo, and Bo Yang have processed the epitaxial structures and given rapid feedback. The second team, the researchers at BAE Systems — Dr. Chris Cooke, Dr. Allen Hairston, Dr. Phil Lamarre, Dr. Marion Reine, and Dr. Kwok Wong have fabricated photodetector arrays of record performance besides also processing and testing discrete devices.

I am also indebted to Dr. Werner Götz, Dr. Michael Krames, and Dr. Ling Zhou of Lumileds Lighting, LLC for generous help with nitride light emitter work — by performing miscellaneous characterizations and by providing useful advice through hours of discussion they made a significant

difference in the final results.

Finally, I would like to thank my parents, Urna Chowdhury and Dr. Tapan K. Chowdhury and my sister Keya Chowdhury for their endless support and encouragement.

UTTIYA CHOWDHURY

*The University of Texas at Austin*

*December 2002*

# **MOCVD Growth for UV Photodetectors and Light Emitting Diodes**

Publication No. \_\_\_\_\_

Uttiya Chowdhury, Ph.D.

The University of Texas at Austin, 2002

Supervisor: Russell D. Dupuis

Due to a number of commercial, scientific and defense applications, there exists a high demand for solid-state ultraviolet (UV) light emitters and photodetectors. Group III-nitrides are very promising materials for fabrication of these because of their large direct bandgap and high thermal stability.

MOCVD growth of III-nitrides along with characterization of the material has been performed aimed towards development of UV optoelectronic devices. Photodetector arrays operating around 280 nm wavelength range have been fabricated from epitaxial structures grown and UV LEDs with wavelength shorter than 300 nm have been fabricated.

Technological challenges in improvement of these devices have been identified and roadmap for future research has been proposed.

# Contents

<b>Acknowledgments</b>	<b>v</b>
<b>Abstract</b>	<b>viii</b>
<b>List of Tables</b>	<b>xii</b>
<b>List of Figures</b>	<b>xiii</b>
<b>Chapter 1 Introduction to Group-III Nitrides</b>	<b>1</b>
1.1 Introduction . . . . .	1
1.2 Application of UV Optoelectronics . . . . .	4
1.3 Properties of Nitride Semiconductors . . . . .	5
1.4 Suitability of III-Nitride Semiconductors for UV Optoelectronics	10
1.5 Metalorganic Chemical Vapor Deposition . . . . .	12
1.6 Common Characterization Techniques . . . . .	18
1.6.1 Introduction . . . . .	18
1.6.2 X-Ray Diffractometry . . . . .	18
1.6.3 Transmission Electron Microscopy . . . . .	21

1.6.4	Photoluminescence . . . . .	23
1.6.5	Cathodoluminescence . . . . .	26
1.6.6	Hall-Effect Measurement . . . . .	28
1.6.7	Atomic Force Microscopy . . . . .	30
1.6.8	Secondary Ion Mass Spectroscopy . . . . .	31
<b>Chapter 2</b>	<b>Operating Principles of Relevant Devices</b>	<b>35</b>
2.1	Introduction . . . . .	35
2.2	$p - n$ Junction Diode . . . . .	36
2.3	Light Emitting Diode . . . . .	39
2.4	$p - i - n$ Photodetectors . . . . .	43
<b>Chapter 3</b>	<b>Review of Nitride Research</b>	<b>48</b>
3.1	Early Research in III-Nitrides . . . . .	48
3.2	Substrate Issues and Improvement of Material Quality . . . . .	56
3.3	Doping of III-Nitrides . . . . .	62
3.4	Nitride Photodetectors . . . . .	65
3.5	Nitride Light Emitting Diodes and Lasers . . . . .	68
<b>Chapter 4</b>	<b>Development of the SBD and UV LED</b>	<b>74</b>
4.1	Introduction . . . . .	74
4.2	Material Growth . . . . .	75
4.2.1	Growth Conditions . . . . .	75
4.2.2	Material Requirements . . . . .	76

4.2.3	Development of High-Quality AlGaIn . . . . .	79
4.2.4	Development of Low Resistivity AlGaIn:Si . . . . .	85
4.2.5	Other Issues Related to SBDs . . . . .	88
4.2.6	Superlattice Doping for <i>p</i> -type AlGaIn . . . . .	92
4.3	Solar-Blind Photodetectors . . . . .	95
4.4	Development of UV LEDs . . . . .	98
<b>Chapter 5 Recommendation for Future Research and Summary</b>		<b>112</b>
5.1	Photodetectors . . . . .	112
5.2	Light Emitters . . . . .	114
5.3	Summary . . . . .	115
<b>Bibliography</b>		<b>119</b>
<b>Vita</b>		<b>132</b>

# List of Tables

1.1	Properties of wurtzite III-nitride semiconductors. . . . .	10
4.1	Conditions used for MOCVD growth. . . . .	77
4.2	Performance characteristics of SBD. . . . .	102

# List of Figures

2.1	Charge density, electric field and conduction band as a function of position for a $p - n$ diode. . . . .	37
2.2	The separation of quasi-Fermi levels in a forward biased $p - n$ junction. In the $n$ -side diffusion region, the hole concentration is magnified 500-fold for convenience of visualization. . . . .	41
4.1	AFM image of a typical AlGaN surface on sapphire in $5\ \mu\text{m} \times 5\ \mu\text{m}$ scale (sample M2983). . . . .	79
4.2	SIMS profile of an SBD device showing low oxygen content (sample M2510). . . . .	80
4.3	TEM image of thick AlGaN layer in an SBD device showing dislocations and reduction of dislocation density with epitaxial growth (sample M2510) (Measurement by D. N. Zakharov and Z. L. Weber; Lawrence Berkeley National Laboratory). . . . .	81
4.4	Correlation of Al-content in AlGaN from different methods. . . . .	84

4.5	Variable temperature Hall-effect measurement on an AlGaIn:Si+ layer. (Measurement by W. Götz; Lumileds Lighting). . . . .	87
4.6	Optical transmittance measurements on various layers related to an SBD. The vertical scale is arbitrary. . . . .	90
4.7	XRD RSM around the (205) reciprocal space point for an as- grown SBD device sample. The X and Y axis units are distances in reciprocal space in inverse Å unit (sample M2510). . . . .	91
4.8	I-V characteristics for comparison of vertical resistivity reduc- tion in <i>p</i> -type AlGaIn SLS. . . . .	94
4.9	Voltage-current characteristics of a fabricated SBD device under dark and UV-illuminated conditions. . . . .	97
4.10	EQE spectra of fabricated SBD devices at different bias volt- ages. Inset shows corresponding responsivity spectra at zero volt bias. (Measurement by P. Lamarre, M. Reine, and K. Wong; BAE Systems). . . . .	99
4.11	Responsivity plot for a $256 \times 256$ SBD array. The color bar on the right hand side indicates responsivity in an arbitrary linear scale. (Measurement by A. Hairston, and C. Cooke; BAE Systems). . . . .	100
4.12	Plot of bias voltage and output power vs. device current for GaIn SQW LED. . . . .	101
4.13	EL spectra obtained from the fabricated GaIn SQW LED under different injection current densities. . . . .	104

4.14 Room temperature CL spectra of a thick $\text{Al}_{0.42}\text{Ga}_{0.58}\text{N} : \text{Si}$ — sample (sample M2983). . . . .	106
4.15 Plot of bias voltage and output power vs. device current for $\text{AlGaIn}$ DH LED emitting at 302 nm. . . . .	108
4.16 EL spectra of $\text{AlGaIn}$ DH LED emitting at 302 nm at 80 $\text{A}/\text{cm}^2$ excitation current density. . . . .	109
4.17 EL spectra at different injection current densities for $\text{AlGaIn}$ DH LED emitting at 290 nm. . . . .	111

# Chapter 1

## Introduction to Group-III Nitrides

### 1.1 Introduction

Semiconductor research at the present time is mostly concentrated in the study of silicon and related materials and III-V semiconductors (arsenides, phosphides, antimonides and nitrides of gallium, indium and aluminum). It has been true for quite some time that by sheer volume, silicon technology has dominated the semiconductor device marketplace. Partly due to the performance of this technology and partly due to the knowledge and technology established already by research worth significant amount of time and money, alternate semiconductors of greater promise have not been able to enter the marketplace. The main industrial interest in other semiconductors is thus

in fields where silicon technology cannot deliver — e.g. in the field of optoelectronics and electronic devices requiring speed, power or thermal stability beyond the capability of Si. Compound semiconductor research, particularly the research in the III-V semiconductors, is concentrated in addressing device markets currently inaccessible to Si technology. Direct-bandgap III-V semiconductors span the entire visible spectral range. In addition, intrinsic high carrier mobility and the ability to form a heterostructure give them a very big advantage in fabrication of high-speed/high-power electronic devices.

It goes without saying that of the human senses, vision is the most powerful and versatile. The ability to cater to the sense of vision is clearly the basis for the greatest number of applications of optoelectronics. Direct-bandgap semiconductors can easily produce photons by the recombination of an electron in the conduction band with a hole in the valence band. Compared to other sources of light, semiconductor emitters are much more convenient and attractive due to their spectral purity, speed, compactness, high efficiency, low-power consumption, low-voltage operation, etc. For the purpose of visible illumination, semiconductor optoelectronics can be used for indicator lights, color display panels, general-purpose illumination, photodetection, etc. Besides the applications in the visible spectra, due to high speed, ease of maneuverability and a variety of other reasons, industry has an endless list of applications for virtually all wavelength ranges of the photon spectra.

The III-V semiconductors have traditionally been divided into two parts — the conventional III-Vs are the arsenides, phosphides and antimonides while

the nitrides are treated separately due to differences in growth conditions, crystal structure and miscibility. The present status of the conventional III-V semiconductor technology is clearly far ahead of the III-nitrides largely because of the unavailability of substrates for homoepitaxy and difficulty in growth chemistry for the III-nitrides.

The conventional III-Vs have a relatively smaller bandgap than the nitrides. This small bandgap is associated, on one hand, with a high carrier mobility, and on the other hand, with a comparative chemical and structural unstability. These semiconductors are easily broken, chemically altered and etched. The small bandgap lend them useful for light-emitting applications from green to infrared and in high-speed electronic switching applications. The visible spectra on the blue side beyond green and the ultra-violet spectra are only addressed by the III-nitrides due to their large bandgap properties. Also, the III-nitrides are chemically and structurally much more stable making them suitable for high temperature and corrosive environments. Like most wide bandgap semiconductors, the nitrides exhibit superior radiation hardness compared to the other smaller bandgap counterparts such as GaAs and Si — allowing their use in demanding space applications.

Although the bandgap of the nitrides extends well into the red of the visible spectra, nitride research has traditionally not paid much attention to the part of the spectra from green to red due to the relative difficulty in nitride technology and ready availability of alternative conventional III-V technology.

## 1.2 Application of UV Optoelectronics

Electromagnetic radiation in the wavelength range of  $\sim 400$  nm to  $\sim 700$  nm in vacuum forms the visible range of the photon spectrum. Radiation of shorter wavelength, situated beyond the visible spectrum and spanning to the X-ray spectrum (roughly from 100 nm to 400 nm), forms the ultraviolet (UV) spectrum of light. Just like any other wavelength range of the optical spectra, light of the UV range finds a wide variety of applications in modern science and technology. While some of these applications such as curing of paint, developing of printing plates, germ decontamination, etc. are best addressed by high-power UV lamps such as mercury arc lamps, semiconductor UV optoelectronics are the ideal solution in many other areas due to smaller size, higher efficiency, longer life, and higher spectral purity.

UV light sources are attractive in applications requiring a small beam spot, such as laser printing and optical data storage, because of its shorter wavelength compared to visible light. Combined with suitable fluorescent material, a UV light source can be used to generate white light (of broad spectral range in the visible region) or light of a certain color (having a narrow spectral range). UV light source and detectors can be used in a variety of military or defense related applications including detection of biological agents from their fluorescence signature and detection of missiles from the UV emission of the exhaust plume.

For defense related purposes, one very important spectral range is the

solar-blind range in the 240 – 280 nm. Solar radiation energy of wavelength shorter than  $\sim 290$  nm is strongly absorbed by the terrestrial ozone layer and at Earth’s surface, a photodetection system operating in this spectral range will not see a huge background signal from the solar radiation. A photodetector array system sensitive to this band situated in the space beyond the ozone layer on the dark side of earth will be an extremely sensitive detection system for objects such as missiles, planes and rockets coming out of the environment. Also, line-of-sight space-to-space communication occurring beyond the ozone layer in this band would not be detectible from the Earth. Ground based line-of-sight communication systems based on UV lasers and detectors are also attractive for various military and commercial applications.

Apart from these, there are many commercial, scientific and military applications of compact solid-state UV light sources and high-efficiency UV photodetectors. As the technology matures, more applications and demand for UV optoelectronics are sure to be developed.

### 1.3 Properties of Nitride Semiconductors

Group-III nitrides (InN, GaN, AlN and their alloys) are semiconductors crystallizing in the wurtzite structure (space group 186:  $P6_3mc$ ) in their most stable form. In this form, all the binary and alloy III-nitrides are direct-bandgap materials with room-temperature bandgaps ranging from  $\sim 1.89$  eV for InN (corresponding to a vacuum wavelength  $\sim 656$  nm red luminescence)

to  $\sim 6.2$  eV for AlN (vacuum wavelength  $\sim 200$  nm, deep ultraviolet). The ratio of  $c$  to  $a$ -lattice constant varies for the system and is not equal to the ideal wurtzite ratio of 1.633 for any of the nitride alloys. The III-nitrides also crystallize in the zinc-blende structure — the zinc-blende energy gaps being slightly lower. Also, unlike in the wurtzite form, the zinc-blende form of AlN does not have a direct bandgap. The scope of the present work is solely confined to the study of nitrides in the wurtzite structure.

Due to the strong ionic component of the bond between the Group-III atom and the nitrogen atom, the III-nitrides are highly stable structurally and chemically. GaN and AlN display superior resistance to most chemicals and of conventional wet etchants are known to etch in hot KOH solution only. The chemical inertness can, on one hand, be advantageous because the device will be able to tolerate chemically harsh environments. However, this also makes processing steps much harder. Particularly, one very useful aspect of conventional III-V technology is the ability to selectively etch down to atomically smooth layers.

Electrical properties of III-nitrides have also been extensively studied. Unintentionally doped GaN is usually found to be  $n$ -type in the low  $10^{16}/\text{cm}^3$  concentration range although optimized growth conditions can yield semi-insulating material. The most common  $n$ -type dopant for GaN is Si. The only successful  $p$ -type dopant remains Mg, which is a very deep acceptor with an acceptor energy in the range of 200 meV in GaN. This leads to a room-temperature ionization of only about 1% of the acceptor atoms, requiring a

Mg concentration in the  $10^{20}/\text{cm}^3$  for a free hole concentration of  $10^{18}/\text{cm}^3$ . Higher free hole concentration in GaN has not been demonstrated — this is because beyond around  $10^{20}$ th concentration range, Mg atoms incorporate into interstitial positions acting as compensating donors. This leads to a reduction in free hole concentration. The mobility commonly found for Mg-doped GaN is around  $10 \text{ cm}^2/\text{V} - \text{sec}$ . *P*-type doping in AlGaN with high Al-composition is another big challenge in nitride technology because the depth of the acceptor level increases fast with Al-concentration making it virtually impossible to obtain a decent free hole concentration for fabrication of electronic devices.

Another interesting twist in Mg-doping of nitride semiconductors is that atomic hydrogen, a species abundant in the MOCVD growth environment, gets incorporated in the Mg-doped material and acts as a compensating donor, deactivating the Mg-dopant. This hydrogen must be driven out by annealing in a nitrogen environment (or by other means) to activate the Mg acceptors.

The wurtzite structure does not possess a center of inversion and, as a result, is compatible with piezoelectricity. The III-nitrides are piezoelectric, and the piezoelectric coefficient is quite large for the material system. The wurtzite structure has a unique rotation axis ( $6_3$ -screw in *c*-direction) and no mirror or inversion symmetry perpendicular to that axis. As a result, crystals in the wurtzite structure can have spontaneous polarization. The coefficients of spontaneous polarization are also large for the III-nitrides. Basically, in the *c*-direction, the material can be seen as alternating monolayers of Group-III species and N. Two such layers are grouped together with a distance equaling

one third the tetrahedral bond length, and the distance between two such plane-pairs is one and a third tetrahedral bond length. Since the Group-III species form a negative ion plane and the N atoms form a plane of positive ions, the system can be looked at as a stacking of dipoles in the  $c$ -direction. The dipole density gives rise to spontaneous polarization even in the absence of any strain. Under strain conditions, the layer distances change, giving additional polarization components. If the planes of epitaxy are perpendicular to the  $c$ -direction (which is the common case), the polarization becomes an important issue in device operation. Polarization can produce large built-in fields in layers which can be used both to a design advantage, and can also significantly limit design options in certain cases. Aspects of polarization in nitrides have been discussed in detail by Bernardini et al. [3], [4].

Until recently, native substrates for homoepitaxy of nitrides were not available at all. The substrates recently made available commercially are of small size, imperfect material quality and come at a prohibitive cost. Most of the epitaxial growth of III-nitrides is done on sapphire substrates because of its wide availability in high-quality, hexagonal symmetry, adequate material quality obtained, compatibility with high temperature, ease of handling and pregrowth cleaning, etc. However, due to the thermal and lattice mismatch between sapphire and the III-nitrides, growth has to be started with a thin polycrystalline nucleation layer which incorporates a high threading dislocation density into the material. A thick epi of 1 to 2  $\mu\text{m}$  thickness is therefore required to be grown to reduce the threading dislocation density to acceptable

limits before starting the growth of the device layers. Another limitation of sapphire substrates is that due to the large lattice mismatch, the nitride epilayers grow on them with a  $30^\circ$  rotation. This causes a misalignment between the cleavage planes of the nitrides and the sapphire substrates. As a result, when an epitaxial structure on sapphire is cleaved, the substrate actually cleaves while the epi is broken along the sapphire cleavage plane (known as break and cleave). This eliminates the possibility of formation of mirror facets by cleaving for edge emitting laser fabrication. The facets on an epilayer grown on sapphire must be fabricated by dry etching, which can be a challenging process.

Hexagonal SiC has a better lattice and thermal expansion coefficient match with the III-nitrides. SiC is also high-temperature compatible for use in the high-temperature CVD growth environment, and in high-power device applications. Additionally, SiC has a much higher thermal conductivity compared to sapphire, which makes heat dissipation for high-power devices a much simpler issue. SiC wafers are available in *n*-type form, allowing fabrication of backside contact directly to the substrate. It is also available in semi-insulating form (at a very prohibitive price) which is required for most electronic device applications. Due to the smaller lattice mismatch, the nitride layer grows on SiC with the *a*-axes aligned, eliminating the cleaving problem in the case of sapphire substrates. One problem for the SiC substrates, however, is that they are not UV-transparent, which makes light extraction or light introduction through the substrate a virtual impossibility for UV operation. Due to

Property	Unit	AlN	GaN	InN
Direct-bandgap energy	(eV)	6.2	3.39	1.89
Density of state eff. mass	( $m$ )	0.48	0.2	0.11
Longitudinal elastic constant	(dyn/cm <sup>2</sup> )	$4.42 \times 10^{11}$		
Transverse elastic constant	(dyn/cm <sup>2</sup> )	$2.65 \times 10^{11}$		
DC (rel.) diel. const.		8.5	8.9	15.3
High freq. (rel.) diel. const.		4.77	5.35	8.4
Polar optical phonon energy	(meV)	99.2	91.2	89.0
$c$ -lattice constant	(Å)	4.98	5.185	5.7
$a$ -lattice constant	(Å)	3.11	3.189	3.54
Thermal conductivity	(W/cm-K)	2.85	1.3	-
$\alpha$ -coeff. of thermal expn.	(ppm/°C)	4.5	5.6	-

Table 1.1: Properties of wurtzite III-nitride semiconductors.

surface wettability issues, GaN cannot be grown directly on SiC — a high-temperature AlN buffer layer is first required to be grown to provide adequate wetting. Since AlN is an insulator, a device fabricated on such a structure cannot be contacted from the backside. Backside contact has to be realized by specially optimized highly doped AlGaN buffer layers.

Some of the more relevant quantities for III-nitrides are listed in Table 1.1.

## 1.4 Suitability of III-Nitride Semiconductors for UV Optoelectronics

As mentioned before, Group III-nitrides (InN, GaN, AlN and their ternary and quaternary alloys) are direct-bandgap compound semiconductors, crystallizing in the wurtzite structure in the most stable form. The bandgap

ranges from 1.9 eV (656 nm wavelength) for InN to 3.39 eV (366 nm) for GaN to 6.2 eV (200 nm) for AlN, spanning a very wide spectral range from red to deep UV. Being direct-bandgap semiconductors, they can theoretically be used to fabricate light-emitting devices such as light-emitting diodes (LED) and lasers over this entire spectral range. Another reason that makes the III-nitride semiconductors attractive for device applications is their high bond strength. ZnSe-based II-VI semiconductors also have bandgaps suitable for short-wavelength optoelectronic devices but the bond strength in the II-VI wide-bandgap semiconductors is relatively low. The values of the bond energy are 2.3 eV/bond in GaN and 1.2 eV/bond in ZnSe. Due to stronger bonds, nitride based devices have the ability to operate in high-temperature environments and are compatible with high processing temperatures. In addition, the III-nitrides have a high thermal conductivity, which allows efficient heat dissipation from devices operating in high-current conditions (e.g. lasers and power transistors). They also have a high electron saturation velocity ( $v_s$ ), which is a useful property for a number of device applications such as field-effect transistors (FET) and  $p-i-n$  photodetectors, because the high  $v_s$  translates into higher device speed.

To design high-performance optoelectronic devices, the use of heterostructures is essential. Fabrication of a heterostructure, however, may be limited by alloy miscibility and lattice constant considerations. Low miscibility leads to difficulty in growth of homogeneous material and a high lattice mismatch leads to relaxation and material quality deterioration. The AlGaIn alloy sys-

tem is fully miscible, and the lattice mismatch between GaN ( $c$ -lattice constant  $c = 5.185 \text{ \AA}$ ) and AlN ( $c = 4.98 \text{ \AA}$ ) is small. As a result, much flexibility is available in the design of optoelectronic devices using the AlGaIn alloy system. As noted before, the bandgap of the AlGaIn alloys spans the spectral range from  $\sim 366 \text{ nm}$  to  $\sim 200 \text{ nm}$ . As a result, it is a very attractive material system for fabrication of UV light emitters and photodetectors.

## 1.5 Metalorganic Chemical Vapor Deposition

Developed by H. Manasevit et al., metalorganic chemical vapor deposition (MOCVD) is a vapor-phase process for producing an epitaxial film of semiconductor disposed on a single-crystal substrate. MOCVD is a proven technique for obtaining high-quality, high-purity epitaxial layers in a variety of material systems. Unlike other vapor-phase epitaxy (VPE) techniques, MOCVD utilizes metalorganics, such as trimethylgallium (TMGa), as sources for the Group-III element — Ga in this case. The Group-V element is usually a hydride such as ammonia ( $\text{NH}_3$ ). Typically, the hydride reacting with the metalorganic source in a hydrogen ambient under appropriate temperature and pressure conditions produces molecules of the required semiconductor material, which deposit on the substrate, giving an epitaxial layer. Modern MOCVD systems take advantage of sophisticated technologies such as computer control of process conditions, flow rates, pressures, and valves, as well as various in-situ monitoring, gas purification systems, etc.

The MOCVD growth system can basically be divided into four subsystems: gas delivery system, growth chamber, wafer load system and an exhaust system.

The gas delivery system can further be divided into two parts — one part for the hydride source and the other for the alkyls. The metalorganic sources are commonly available in solid or liquid form, in stainless steel bubbler containers. These bubblers are maintained at constant temperature by use of constant temperature baths. Above the alkyl level at the bottom of the bubbler, there exists a gas volume that contains the vapor of the alkyl at equilibrium with the solid or liquid alkyl source for a given temperature and pressure. The alkyl molecules for growth are collected from this volume, and during growth, some carrier gas (usually hydrogen or nitrogen) is bubbled through the alkyl to maintain the alkyl partial pressure. A pressure controller (PC) downstream from the bubbler maintains a constant pressure in the bubbler, and a mass flow controller (MFC) upstream from the bubbler is used to control the required molar flow of the alkyl into the growth chamber. The MFC and the PC are usually controlled electronically through analog output boards connected to small computer units. This allows precise control of alkyl molar flows with constant or time varying setpoints. The stainless steel tubes carrying the alkyl over to the growth chamber are heated with resistive heaters to prevent alkyl deposition on the tube walls. During reactor idle times, the lines are continuously purged with carrier gas bypassing the bubbler. The hydride sources usually come as a gas or vapor. They are used either in pure

form or diluted in some carrier gas such as hydrogen. These can therefore be plumbed directly into the injection block through appropriate MFC units. However, in order to achieve a higher purity level, in-line gas purifiers are often placed in the lines.

Both the alkyls and the hydrides are introduced into the chamber through pressure-balanced growth and vent injection blocks. Separate injection blocks for the hydrides and alkyls are used to prevent pre-reaction of the gases before they enter the reactor chamber. The growth and vent injection blocks are maintained at the same pressure by use of compensating push-flows controlled by the pressure differential between the two blocks. The vent injection lines bypass the chamber and direct the gas straight to the exhaust pump line while the growth injection lines direct the gas into the growth chamber. Thus, gas flowing through each source in the reactor system can be directed either to the reactor chamber or to the bypass or “vent” line. When needed, each source flow is switched from the vent line into the growth injector. Since the vent and the growth lines are pressure-balanced, this procedure reduces switching transients significantly.

The growth chamber is usually fabricated from stainless steel or quartz. A variety of configurations for the growth chamber are in use, all having their relative advantages, disadvantages and suitability to appropriate purposes. The main requirements of the growth chamber are a heating system to maintain the substrate temperature at the desired level, a gas flow system to direct the source gases onto the substrates under laminar flow conditions, and an

exhaust system capable of maintaining the chamber pressure as required. A laminar flow is required on top of the substrate because a turbulent flow will introduce all sorts of variations over the growth surface, and also make sharp interfaces between two types of layers virtually impossible. In addition, the boundary layer thickness established over the substrate by the flowing gas has to be uniform in order to maintain a uniform growth rate and composition over the substrate. One design to address this requirement is the rotating disk reactor. The rotating disk reactor is an approximation to the von Karmann pump, which is an infinite rotating disk in a semi-infinite volume of gas. The von Karmann pump is one case where the Navier-Stokes equation for flow can be solved in closed form to yield uniform boundary layer thickness over the entire disk when the frictional speed of pumping by the disk equals the gas flow rate.

A number of in-situ characterization tools are often attached to the growth chamber as accessories. These can include a residual gas analyzer for study of growth chemistry, a pyrometer for determination and control of true temperature, a reflectance monitor for determination of the growth rate, etc.

Since oxygen and moisture are usually very detrimental to the growth of common semiconductors, care should be taken not to expose the growth chamber to atmosphere. To accommodate this along with the requirement of loading and unloading substrates, some sort of loading mechanism is required. Common loading mechanisms are based on either a vacuum loadlock or a nitrogen purged glove-box.

The exhaust system of an MOCVD system is generally connected to a pump capable of high pumping speed at desired process pressure. Since a significant amount of solid byproducts are generated in the growth process, these are filtered-out before the gas gets to the pump. Also, in order to maintain a consistent growth chamber pressure, a butterfly valve, feedback-controlled by a pressure transducer on the chamber is typically used.

Like any other chemical vapor deposition (CVD) system, MOCVD can occur in one of two growth regimes — diffusion-controlled and kinetically controlled. Kinetic control is achieved when the reaction rate is limited by the growth temperatures, rather than by the rate of arrival of precursors at the surface. This mode of growth is usually not desired because this leads to high non-uniformity due to a small spatial variation of temperature. The desired diffusion-controlled growth is obtained when the reaction rate is controlled by the precursor arrival rate and the temperature is high enough to support a much higher growth rate already. More details on MOCVD growth mechanism can be found in [6].

Compared to the growth of conventional III-V materials, MOCVD growth of nitrides is problematic because of the involvement of ammonia. Ammonia is a corrosive substance requiring careful selection of materials for fabrication of the reactor chamber. Also, ammonia is a very stable compound requiring a high temperature for dissociation. Alternate nitrogen sources have been studied to eliminate the requirements of ammonia. However, the requirement of high-temperature is usually seen to persist in order to provide sufficient surface

mobility to the adsorbed molecules in order to create a high-quality crystal. Also, compared to the conventional III-V technology, a much higher ammonia flow is required, which complicates the obtaining of laminar flow.

Due to the unique chemistry involved in the growth of nitride semiconductors, MOCVD has proven to be the most suitable technology to date for growth of high-quality nitride films. The other competing technology for the growth of InAlGa<sub>N</sub> alloys is the molecular beam epitaxy (MBE) process. MBE as a growth technique for the nitrides has not seen as much success as MOCVD because growth temperatures in MBE are low and ammonia, a common source of nitrogen, is stable at low temperatures. Alternate nitrogen sources, including plasma cracking of ammonia, have been studied and recently MBE has also shown the ability to grow high-quality nitride material for electronic applications. Another problem faced in MBE growth of nitrides is that the crystal often grows with the N-face towards the surface which is known to give bad morphology and numerous other device problems. MOCVD growth on the other hand, occurs invariably with the Ga-face towards the growth surface. It is probably safe to say that to date, MOCVD is well ahead of MBE as a growth technique for the III-nitrides — particularly for light-emitting applications.

## 1.6 Common Characterization Techniques

### 1.6.1 Introduction

The study of semiconductor materials requires a number of characterization techniques. The variety of characterization techniques used to study III-nitrides in crystalline form is large, and even an overview of all these techniques can be daunting. Some of the more common techniques that have been used in the present study are described below.

### 1.6.2 X-Ray Diffractometry

X-ray diffractometry (XRD) is a very convenient characterization technique for all sorts of crystalline materials. Because of the periodic structure every crystal has, associated with it, a reciprocal space which is basically a three dimensional Fourier transform of the real-space periodicity. Like all other diffraction techniques, XRD probes the reciprocal space associated with a periodicity. In addition, the very short wavelength of an X-ray photon (typically,  $\lambda = 1.54\text{\AA}$ ) allows it to scan the reciprocal space points corresponding to a very short crystalline period ( $< 5\text{\AA}$ ). For single-crystal diffractometry, either the Bragg formalism, or the more elaborate Ewald sphere analysis is the most convenient description of the XRD technique. In the Ewald sphere approach, with the X-ray source and detector set at a certain angle, the system is basically probing a certain point in the reciprocal space of the crystal under

measurement given by the Laue equation:

$$\vec{k}_i - \vec{k}_r = \vec{G}$$

where  $\vec{k}_i$  is the wavevector of the incident beam,  $\vec{k}_r$  is the wavevector of the reflected beam and  $\vec{G}$  is the vector pointing towards the reciprocal space point being probed. A detailed analysis of these formulations can be found in many text books on solid-state physics [5].

For material characterization, a symmetric  $\omega - 2\theta$  XRD scan can be used to determine the  $c$ -direction lattice constant by use of the Bragg law:

$$\lambda = 2d \sin \theta$$

where  $\lambda$  is the X-ray wavelength,  $d$  is the periodicity of the structure being scanned, and  $\theta$  is the Bragg angle — the angle between the normal to the periodic planes and the source or the detector. If measured on a crystalline alloy of two components, the  $c$ -lattice constant can be used to determine alloy composition by use of Vegard's law. If the crystal structure consists of a short-period superlattice, then a long  $\omega - 2\theta$  scan with sufficient integration time can display peaks arising from the introduction of new points in the reciprocal space by the superlattice periodicity. Often the best way to analyze the  $\omega - 2\theta$  scan data of a structure is to compare with Takagi-Taupin dynamic XRD simulation data. Commercial software is now readily available to produce such simulation data, and also to automatically fit the measured data with a proposed structure by varying a number of structural descriptions such as alloy

composition, thickness, percentage relaxation, substrate bowing, etc. More detailed descriptions of dynamic XRD can be found in appropriate textbooks [7].

Given a perfectly periodic structure of 3D delta functions in an infinite array, then in the Fourier space, each of the reciprocal space points will also be perfect delta functions with infinite height and zero spread. However, when considering real crystal structures, these peaks in the reciprocal space will be broadened due to a number of factors such as finiteness of the crystal structure, presence of defects, etc. The spread in any reciprocal space point can thus be a good indication of the perfectness of the crystal, acting to indicate material quality. The full-width at half-maxima (FWHM) of an  $\omega - 2\theta$  scan or a rocking curve is often used to compare material quality in the nitride technology.

Also, by using of a triple axis XRD system, a number of consecutive  $\omega - 2\theta$  scans can be taken at small  $\omega$  changes which can be shown to yield a map of the reciprocal space centered around the point obtained by the center  $\omega$  and center  $2\theta$ . The spread of a reciprocal space peak (known as the mosaic spread) along with tilts can be studied much better in such a map. If measured around an asymmetric point in the reciprocal space, the position of a reciprocal space peak directly gives the  $a$  and  $c$ -lattice constants of the crystal. Also, if scanning a lattice-mismatched layered structure, this information can be used to determine whether a layer grown on top of another is fully strained to the layer underneath or not.

Another useful characterization technique using X-ray is the glancing

incidence X-ray analysis (GIXA). This is not a diffractometry experiment, but simply is a reflectance measurement by use of X-ray photons. The reflectance data obtained can be simulated to obtain layer thickness from the oscillation period of the reflectance data and information about interfacial roughness can be obtained from the decay rate of reflectance. Since the X-ray wavelength is very short, the technique can be used to determine the thickness of very thin layers in the order of a few tens of nm-s.

Other than these standard uses of XRD, special characterization techniques have also been developed to study III-nitrides.

### **1.6.3 Transmission Electron Microscopy**

Transmission electron microscopy (TEM) is an electron microscopy technique under widespread use in the study of crystalline, polycrystalline, and amorphous material. In this technique, an electron beam of uniform current density is used to irradiate a thin specimen, and the electron intensity distribution after transmission through the sample is used for imaging. The electron intensity distribution varies due to the interaction of the electron beam with the material as the beam passes through it. Electrons interact strongly with condensed matter — the mechanism of interaction can be one of the following:

a) Elastic Scattering: Elastic scattering is an interaction between the imaging (high-energy) electrons and the nucleus of the atoms in the matter being imaged. Total energy and momentum is conserved. If the scattering angle is large, a large amount of energy is transferred to the nucleus, which

can even displace the atom.

b) Inelastic Scattering: Inelastic scattering is an interaction between the imaging electrons and the electron cloud of the material. Energy transfer occurs that can excite electrons to higher levels, which then can produce X-ray or Auger electrons by recombining to the lower energy eigenstates.

c) Diffraction: If the material under study is crystalline, then the periodic potential can diffract the Bloch wave of the incident electron.

The electron beam can be manipulated by use of magnetic lenses using the Lorenz force law:

$$\vec{F} = q(\vec{v} \times \vec{B})$$

Due to the difficulty in producing a very customized magnetic field pattern in an open-beam path, the focusing ability of such magnetic lenses is much inferior to the optical lenses that are commonly used for manipulation of light. This acts as a very fundamental limitation in all electron microscopy techniques.

For crystal structure imaging purposes, diffraction contrast is the most useful. Diffraction contrast can be used to image various lattice defects such as dislocations, stacking faults, phase boundaries, etc. In this mode, a section in the image is bright only if the zero-order diffraction spectra falls just on the objective aperture. If the image is taken from the primary beam, then the image is called the “bright field image” and if it is taken from one of the Bragg reflected beam spots, the image is called a “dark field image”. Correct interpretation of TEM images generally requires simulation using dynamical

diffraction theory.

Alternatively, if the interference of the primary beam and one of the diffraction spots is used for imaging, it is possible to image the crystal lattice structure. The technique can also be extended to the study of the surface by using reflection electron microscopy in glancing incidence mode.

More detailed description of TEM can be found in many textbooks on TEM and electron microscopy [8].

#### **1.6.4 Photoluminescence**

If a particle carrying high energy is incident on some material, the energy is usually absorbed by the formation of many possible lower energy particle forms. Shining high-energy electrons onto a material for example, can produce backscattered lower-energy electrons, Auger electrons, X-rays, thermal phonons, and many forms of photons.

Luminescence is the emission of light from a material caused by excitation by some form of energy. Typically, when some particle of appropriate energy is incident on the material, all or part of the energy is absorbed by electrons which make a transition from one eigenstate to another higher-energy state. The electron then, after an appropriate amount of time, makes a downwards transition to a lower eigenstate and, if the energy and momentum difference is appropriate, emits a photon to give up the difference in energy.

In the case of a semiconductor, in the “band” picture, the energy imparted by the incident particle is absorbed by an electron in the valence band,

which then makes a transition to the conduction band, creating a hole in the valence band. In the “bond” picture, the incident energy is high enough to break a chemical bond in the crystal, and the energy is again given up by the creation of a photon as the bond is formed again. Since the recombination process requires conservation of both energy and momentum, and since the momentum of a photon is exceedingly small, in an indirect-bandgap semiconductor, an optical transition cannot occur without the help of another particle (phonon), which acts to equate the momentum difference. Due to the involvement of an extra particle in the case of an indirect-bandgap semiconductor, the probability of an optical transition is reduced greatly, making luminescence measurement difficult. Since all the wurtzite III-nitrides are direct-bandgap semiconductors, luminescence measurements are very convenient for characterization.

One convenient form of excitation is by photons, e.g., in the convenient form of a laser beam. This technique is called photoluminescence (PL). If the energy of the laser photons is higher than the bandgap energy of the semiconductor, then they have a high probability of being absorbed. Beginning with a semiconductor in thermal equilibrium, then the steady-state shining of a laser containing a high photon flux will soon establish a high steady-state free carrier concentration in excess of thermal equilibrium. In terms of the Fermi-Dirac distribution, this can be seen as the excitation source causing the quasi-Fermi level in the locality of the excitation to be separated. Due to presence of high electron concentration  $n$  in the conduction band and high

hole concentration  $p$  in the valence band, we obtain a high spontaneous recombination probability which is proportional to the product  $pn$ . The light produced by this spontaneous recombination can be spectrally analyzed in an optical spectrometer, and sensed with a photomultiplier tube or other form of photodetector. An important piece of information such a spectra gives is an estimate of the bandgap energy of the material — which, if the material is a ternary alloy compound, allows the determination of alloy composition by correlating the bandgap dependence with composition.

Generally speaking, the probability of an electron recombining by emission of a photon is reduced by the presence of alternate “scattering” mechanisms. The same mechanisms that reduce the carrier mobility in a semiconductor thus contribute to the reduction of the bandedge luminescence. Thus, a bright bandedge luminescence is a sign of good material quality, relatively free of defect states. Also, if the material is to be used for optical device fabrication, then the photoluminescence measurement is a direct way to determine the suitability of the material for the device purpose. The width of a PL peak is also of consequence — it carries the signature of many things, from thermal scattering of electrons to alloy composition variations.

While in this ideal picture the luminescence occurs by recombination from the conduction band to the valence band, for real semiconductors, a number of other processes can occur. The recombination may involve either or both a donor level and an acceptor level. Some optically active deep energy level may also be involved. Also, the recombination may be associated with

the annihilation or generation of various other quasi-particles such as phonons or excitons. Careful analysis of the PL spectra allows identification of all these recombination processes. PL measurements are often performed at a reduced temperature to eliminate the effects of phonon scattering. The carriers are then “frozen” in states very close to the band edges, and if the PL spectra is scanned with a high-resolution system, many subtle features of the spectra can be accurately identified due to narrowing of luminescence peak.

Another useful form of PL measurement is time-resolved PL (TRPL) where the decay time of the different luminescence peaks is followed by use of a high speed photomultiplier tube or a streak camera coupled with a pulsing excitation laser source.

### **1.6.5 Cathodoluminescence**

Cathodoluminescence (CL) is a characterization technique similar to PL. CL systems are normally added as an accessory to a scanning electron microscopy (SEM) system. In a scanning electron microscope, a directed electron beam is scanned over a small area of a sample. High-energy electrons interact strongly with the solid material; they can be scattered either elastically or inelastically due to interaction with the nucleus or the bound electrons of the material. By interaction with the material, a variety of effects are produced by the electron beam — high-energy back-scattered electrons, low-energy secondary electrons, X-rays and cathodoluminescence. As the beam is scanning over the sample, any one of these signals can be amplified, and the amplified

signal can be plotted in the same way as the sample is being scanned to form an image of the sample surface. Commonly, the SEM image is formed by using the secondary electron intensity. This is a very useful technique for imaging surface features to magnifications as high as 100,000 or greater.

In CL, the focused or scanning beam of high-energy electrons is used as the excitation source instead of the laser excitation used in PL. The light produced is usually collected by a parabolic mirror and is fed to some photodetector (usually a photomultiplier tube) either directly or after selection of a certain wavelength in a spectrometer. Thus, in the scanning mode, either a panchromatic or a monochromatic CL image of a sample area can be obtained. Another mode of operation of a CL system is the spectral analysis of the luminescence with the electron beam focused at a certain point on the sample.

It is to be noted that with the electron beam focused at a certain point on the sample surface (either in scanning mode or in focused mode), the volume of material interacting with the electron beam is not infinitesimal. The incident electron may undergo multiple scattering events inside the sample before losing all its energy or before being directed back towards the surface and escaping. The maximum depth an electron beam with a given energy can get to is given by an expression developed by Kanaya and Okamaya:

$$d = \frac{0.0276 A \varepsilon_b^{1.67}}{Z^{0.89} \rho} \mu\text{m}$$

where  $\varepsilon_b$  is the beam energy in keV,  $\rho$  is the density of the material in gm/cc,

$Z$  is the atomic number and  $A$  is the atomic weight. As a result, depending on the material and beam energy, a certain volume of the material is taking part in the interaction. By varying the acceleration voltage, different interaction volumes can be selected from the material. This can often be useful for the study of different depths of a layered epitaxial structure. More details on electron microscopy can be found in various textbooks on the subject [9]. By use of a cryostat stage, CL can be performed at a reduced temperature also.

### 1.6.6 Hall-Effect Measurement

The Hall-effect measurement is a very useful electrical characterization technique that determines the carrier concentration and mobility in a semiconductor layer. This information is vital for the design of electronic devices because carrier conduction and injection is an integral part of the operation of virtually all devices. For epitaxially grown structures, the method is mostly used to study a layered structure where only one layer of known thickness is doped. It can also be used to study the 2-dimensional electron gas in a heterostructure.

For such purposes, the van-Der Pauw configuration is the most commonly used configuration. In this configuration, four ohmic contacts are made on the corners of a square shaped sample. Then, a constant current is applied through two opposite corners of the sample while a strong magnetic field is applied normal to the surface of the sample. The electrons or holes making up this current experience a force field in the direction determined by the cross

product of the carrier velocity (in the direction of current) and the magnetic field. As a result, a steady-state electric field is established in this direction, which can easily be determined by measuring the voltage drop at the two remaining contact points. This voltage is known as the Hall voltage. Detailed analysis of this method, along with the limits of validity and a more elaborate analysis by treating electrons as Bloch waves under semi-classical equations of motion instead of treating them as charged particles, can be found in most text books on solid state physics [5].

The expression determining the carrier concentration from the Hall voltage, current flow, and magnetic field strength is:

$$n = \frac{IB}{qV}$$

where  $n$  is the electron concentration,  $I$  is the current flowing,  $B$  is the magnetic flux density, and  $V$  is the Hall voltage measured. Since conductivity is given by

$$\sigma = -qn\mu_n$$

where  $\sigma$  is the conductivity and  $\mu_n$  is the electron mobility, the mobility can be determined from the knowledge of the conductivity as:

$$\mu_n = -\frac{\sigma}{qn}$$

The usefulness of the Hall-effect measurement extends further if the measurement can be done at varying temperatures. The temperature dependence of carrier concentration can yield information about the carrier activation energy

and whether special conduction mechanisms exist such as 2D electron gas, conduction through donor band, continuum of donor band with conduction band, etc. The temperature dependence of mobility can be used to determine predominant scattering mechanisms. For example, in common semiconductors, the two most important scattering mechanisms limiting mobility are phonon scattering and ionized impurity scattering. Phonon scattering has a  $T^{-3/2}$  dependence, and ionized impurity scattering has a dependence like  $T^{3/2}$ . By plotting mobility vs. temperature, the effects of these mechanisms can be easily identified.

### 1.6.7 Atomic Force Microscopy

Atomic force microscopy (AFM) is a non-destructive proximity scanning probe technique used to profile a small area of a sample surface to a very fine depth resolution. Unlike traditional microscopes, the size of the probe rather than diffraction effects (in electron or photon optics) generally limit their resolution.

A sharp tip mounted on a flexible cantilever is scanned over the sample surface of a few microns square area by piezoelectric drive circuitry. Measurement can be done either in contact mode or in tapping mode. In the tapping mode, the tip is vibrated at its resonant frequency and is scanned over the surface. Interaction with surface morphology causes a modulation in the vibration of the tip. The vertical motion of the tip flexes the cantilever, and the amount of deflection is detected by the reflection of a laser beam focused

on the back of the cantilever. As the tip is deflected, the reflection angle of the laser is changed, which is measured in a position sensitive photodetector system consisting of two side-by-side photodetectors.

The tip deflection information is then amplified and used to form an image by scanning in the same way as the surface is scanned by the tip. The data can be presented as a 2-dimensional height profile and can be processed to determine a variety of information such as surface roughness. The ideal step profile for epitaxial growth can be observed in an AFM image for good samples. Also, in the case of nitride samples, dark spots are often found in the image; they have been identified with the ends of threading dislocations. Counting the number of these dislocation points allows an easy determination of threading dislocation density without going through time consuming and difficult TEM procedures [1], [2]. Also, the position of threading dislocations relative to surface step edges has been proposed to allow for the identification of different types of threading dislocations.

### **1.6.8 Secondary Ion Mass Spectroscopy**

Secondary ion mass spectroscopy (SIMS) is another useful characterization technique, yielding depth profiling of the concentration of various atoms that are present in a relatively low concentration compared to the primary elements of the material being analyzed. In this method, a focused ion beam slowly sputters or removes surface material by producing physical damage by high energy ions to create a hole starting from the surface. The sputtered

atoms are analyzed in a mass spectroscopy system.

SIMS is clearly a destructive technique. A primary high-energy ion beam is impinged on the sample surface, and the kinetic energy transfer to the atoms in the material causes atoms to be ejected by breaking of bonds. The average number of atoms ejected per incident primary ion is called the sputtering yield. However, if the atom is ejected uncharged, it cannot be analyzed in a mass spectrometer — only an ion can be detected. Generally, of the atoms ejected, a known fraction (about 1%) come out as ions. The number of ions ejected per incident primary ion is called the secondary ion yield. After a sputter run, the secondary ion yield signal can be plotted against sputter time. This by itself does not contain the most useful information. The secondary ion yield has to be scaled to atomic concentration by comparing with previously run calibrations and the sputter time has to be scaled to depth by scaling with the depth of the hole found when the sputtering is completed. Ion-implanted samples are the most common for use as SIMS calibration samples. The secondary ion yield can depend very much on the primary ion species. For electro-positive elements (elements giving positive secondary ions)  $O_2^+$  offers a high secondary ion yield. For electro-negative elements,  $Cs^+$  is a popular choice giving a high secondary ion yield. So, if the set of elements to be profiled includes both electro-positive and electro-negative elements, then two sputter runs need to be made — once with  $O_2^+$  and again with  $Cs^+$ . Mass spectrometry is performed by separation of species by mass to charge ratio. The secondary ion beam is passed through a strong DC magnetic field whereby

the beam is deflected by a force:

$$\vec{F} = q(\vec{v} \times \vec{B})$$

Under a given force, ion beams of different ion masses will deflect by different amounts; and depending on the placement of the slits on the ion-counter on the deflected beam path, different ion species will be selectively counted.

It is important to consider the limitations of SIMS measurements. Selective or preferential sputtering can occur on a sample where some atoms are sputtered at a slower rate than others. In this case, the surface soon gets enriched by the atoms with slower sputter rate; and from then on, the steady state yield carries useful information. Secondary ion yield is strongly dependent on the matrix material (the host material or primary constituent material). Also, as sputtering occurs, the primary ions along with atoms from the surface can be implanted into the material, which on one hand causes damage and on the other hand can bury some atoms from upper layers further into the film. This can spread the profile of the species even if the species is present over a very narrow depth range. The beginning surface roughness imposes another limitation on the depth resolution of SIMS since at a certain point, the mass spectrometer is sensing the ion density from a depth range equal to the surface roughness. The surface can get even rougher as a result of the sputtering process. Another limitation of SIMS measurement is that any species that is abundant in nature (such as nitrogen, carbon, oxygen, etc.) are bound to be present at the surface in a significant concentration. If surface

cleaning or the vacuum created before beginning of sputtering is not adequate, then a profile of these species will show a high concentration at the surface, showing a gradual decay into the material caused by implantation of these species by the primary ions.

SIMS cannot give an accurate atomic concentration of atoms present in significant concentrations — such as the matrix elements. However, it is customary to get a secondary ion yield profile of the matrix elements along with the other elements. If the epitaxial structure contains some alloy layers of different compositions at different depths, then the secondary ion profile shows a corresponding reduction and increase as the alloy composition of that species changes.

## Chapter 2

# Operating Principles of Relevant Devices

### 2.1 Introduction

This section discusses the operating principles of the optoelectronic devices that are described in the later chapters. The most comprehensive device analysis accessible to a designer is the use of a self-consistent Schrödinger-Poisson method whereby the distribution of charge carriers is determined by solving the Schrödinger equation assuming a given potential distribution, and the potential with the presence of the carriers is determined by solving the Poisson equation. From a practical standpoint, the accuracy of even this analysis remains limited due to a number of practical issues, and corrections to take into account the many practical issues remain challenging. Also, often a

very good qualitative analysis can be achieved by the use of simpler arguments along with certain approximations.

Two types of devices will be described in this chapter — light emitting diodes (LEDs) and  $p-i-n$  photodetectors. Both of these are basically simple  $p-n$  diodes. In an LED, electrons injected from the  $n$ -side and holes injected from the  $p$ -side recombine in the depletion and diffusion regions. While the recombination can occur through many different mechanisms, in a direct bandgap material, the probability is high that the recombination will occur through an optical process, yielding one photon per recombination. On the other hand, in a  $p-i-n$  photodetector, photons are absorbed in the  $i$ -region, which generates an electron-hole pair (EHP). This EHP can be swept by the built-in field in the depletion region and contribute to a photo-current.

## 2.2 $p-n$ Junction Diode

A homojunction  $p-n$  diode can be viewed as being formed by mating two pieces of the same semiconductor, one doped  $p$ -type and the other doped  $n$ -type, on a plane. Since the Fermi level of the  $p$ -material is much lower than in the  $n$ -material before mating, electron transfer occurs to the  $p$ -side from the  $n$ -side and vice-versa for the holes. The free carrier transfer from one side to the other causes free-carrier depletion from the two sides of the junction to form a “depletion” region over which, to a good approximation, only uncompensated ionized dopant ions remain. The charge of the dopant

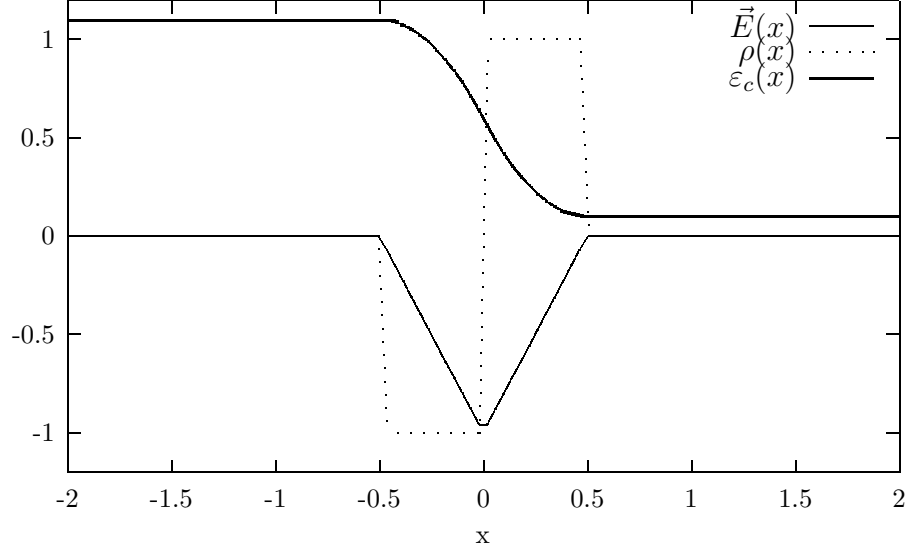


Figure 2.1: Charge density, electric field and conduction band as a function of position for a  $p - n$  diode.

ions creates a built-in electric field over the depletion region, which acts to equilibrate the Fermi level between the two sides in the connected structure. The electric field is found by integrating the charge density, and the energy in turn is found by integrating the electric field. A qualitative plot of the charge density, and the resulting built-in electric field and the energy-band diagram is shown in Figure 2.1. The metallurgical junction is at  $x = 0$  and on the left is the  $p$ -material. In a simple approximation, the charge density  $\rho(x)$  is constant in both the  $p$  and  $n$ -sides of the depletion region. The electric field is linear in each region and the band diagram bends parabolically from the two depletion edges meeting at the interface with the same slope from both sides.

If a positive voltage is applied on the  $p$ -side with respect to the  $n$ -material, the junction is forward biased. The tendency of this voltage will be to cause current-flow from the  $p$ -side to the  $n$ -side, which occurs by holes flowing from the  $p$ -side to the  $n$ -side and by electrons flowing in the opposite direction. It is to be noted in the band diagram that both of these carrier flows will see an “uphill” potential profile in the depletion region and the flow will be limited. However, the applied voltage acts to reduce this potential barrier, which results in an increased current-flow. This results in an exponential increase in the forward current as the forward bias is increased. As the current begins to rise, however, the ohmic drop in the bulk of the material before the depletion region begins to reduce the voltage available to counter the built-in field. This effect ultimately limits the reduction in built-in field and prevents the built-in field from ever being completely countered.

On the other hand, a negative bias voltage will tend to result in electrons flowing from the  $p$ -side to the  $n$ -side. While this flow sees no barrier (and in fact, the built-in field favors such a flow), there is a very low concentration of free electrons on the  $p$ -side and the current is essentially limited by primarily thermal generation of electrons.

These two pictures serve as an elementary description of the operation of a  $p-n$  diode and explain why a  $p-n$  diode will have a rapid current turn-on in the forward direction but will resist current-flow in the reverse direction. Elaborate descriptions of  $p-n$  junction diodes can be found in many text books on solid state electronics [10].

## 2.3 Light Emitting Diode

An LED is an electroluminescent device. Luminescence is produced by the recombination of electrically injected excess electrons and holes. The radiative recombination rate is directly proportional to the product  $pn$  of the free electron concentration,  $n$ , and the free hole concentration,  $p$ , for direct-bandgap semiconductors. In an indirect bandgap material, a radiative recombination between the conduction band minima (CBM) and valence band maxima (VBM) does not conserve total momentum due to separation of these regions in the  $k$ -space. As a result, the radiative recombination process in an indirect-bandgap semiconductor must involve some third particle for maintaining momentum conservation. The probability of radiative recombination is thus largely reduced and other competing mechanisms for recombination dominate for indirect bandgap semiconductors.

As mentioned above, in a direct-bandgap semiconductor, the radiative recombination rate is proportional to the product  $pn$ . In thermal equilibrium, this only equals  $n_i^2$  where  $n_i$  is the intrinsic concentration and its square is a quite small number — particularly for wide bandgap semiconductors at room temperature. This, however, can be greatly enhanced under non-equilibrium conditions. The non-equilibrium carrier concentrations are described by

$$\begin{aligned}n &= N_c e^{-(\epsilon_c - F_n)/kT} \\p &= N_v e^{-(F_p - \epsilon_v)/kT}\end{aligned}$$

where  $N_c$  and  $N_v$  are the effective density of states in the conduction and

valence bands,  $\varepsilon_c$  and  $\varepsilon_v$  are conduction and valence band energies, and  $F_n$  and  $F_p$  are quasi-Fermi levels for electrons and holes respectively. The product of the non-equilibrium free-carrier concentration thus is seen to rise exponentially from the thermal equilibrium value as the separation of the two quasi-Fermi levels is increased. This has a similar effect on radiative recombination rate.

In a forward biased  $p-n$  junction, a simplified analysis can be performed to get a good approximation of the excess carrier profile. Following these analyses, it can be found that the electron quasi-Fermi level stays almost flat over the  $n$ -side and the entire depletion region and similarly for the hole quasi-Fermi level. On the  $p$ -side of the depletion region, the electron quasi-Fermi level gradually drops down and merges with the hole quasi-Fermi level. This occurs over a region called the “diffusion region” with a slope characteristic of electron diffusion length in the  $p$ -material. As a result, over the entire depletion region, the quasi-Fermi levels are separated by an energy equaling the forward bias voltage times the electron charge,  $q$ , while outside the depletion region, the separation linearly decreases. Recombination in the depletion region and the diffusion regions thus are expected to produce luminescence in case of a direct-bandgap material. The principal region where electroluminescence is expected to occur is commonly referred to as the “active region” of an LED. The separation of quasi-Fermi levels in a forward biased  $p-n$  is shown in Figure 2.2 along with variation of valence and conduction bands.

The luminescence in a  $p-n$  junction diode can thus be seen as a result of the injection of holes in the depletion region and into the  $n$ -material from

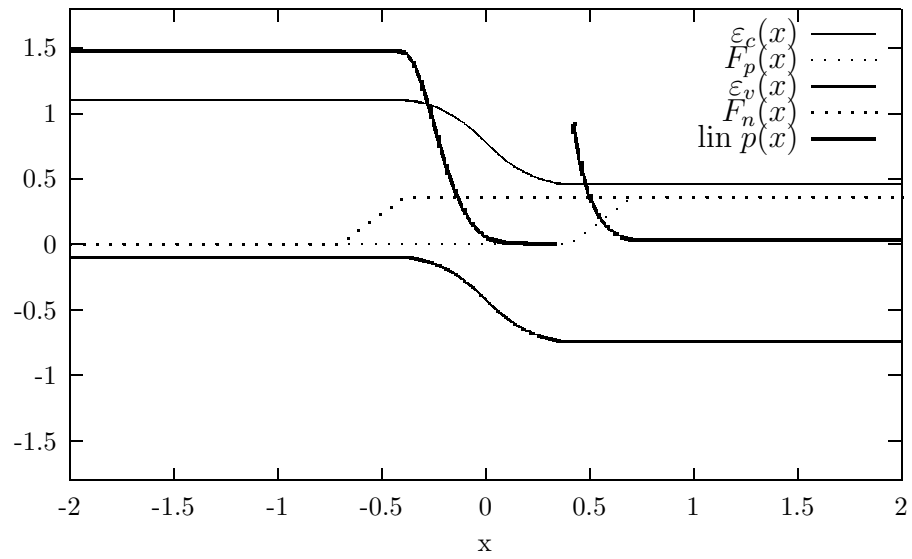


Figure 2.2: The separation of quasi-Fermi levels in a forward biased  $p - n$  junction. In the  $n$ -side diffusion region, the hole concentration is magnified 500-fold for convenience of visualization.

the  $p$ -side, and injection of electrons in the depletion region and the  $p$ -side diffusion region from the  $n$ -side under forward bias. Once the basic mechanism of electroluminescence in a  $p - n$  junction is understood in this way, practical considerations can be addressed. It is clearly desirable to enhance the volume over which the quasi-Fermi levels are separated. This is accomplished by introducing an intrinsic region between the  $p$  and the  $n$ -side, making it a  $p - i - n$  diode. The depletion region is then significantly lengthened because the entire  $i$  region will be depleted. Often, in order to take advantage of enhanced luminescence by doping, a lightly doped region can be used instead of the intrinsic region. The next major improvement can be made in the electronic structure by incorporating a double-heterostructure instead of a homojunction device. In this design, the lower bandgap lightly doped or intrinsic material is sandwiched between wider bandgap  $p$  and  $n$  material. The band-offset results in a significant increase in the carrier injection. Another advantage of double-heterostructure LED is the elimination of self-absorption. In a homojunction LED, the light produced at the junction has to pass through the bulk  $p$  and  $n$  material before being extracted. Since the bandgap of these regions is suitable for absorption of the electroluminescence photons, the number of output photons is significantly reduced. Due to the wider bandgap material used in the  $p$  and  $n$ -side of a double-heterostructure LED, the self-absorption effect is eliminated.

Another improvement over the double-heterostructure LED is the quantum-well LED. In this design, the active region contains one or a few narrow quan-

tum wells confined by a higher bandgap barrier material. The resulting quantum confinement of electrons and holes results in reduced scattering and increased radiative recombination probability due to increased dipole strength. Other miscellaneous improvements in the design of the LED structure are under use, many of which are material-system specific.

Another important aspect of LED design is extraction of light from the semiconductor material. Since the light has to emanate from the semiconductor material (high index of refraction) to air (unity refractive index) in most cases, total internal reflection limits the solid-angle over which light can be extracted from the device. A number of structural modification of the LED mesa, such as polishing to a conical or hemispherical shape, are under use to enhance light extraction.

## 2.4 $p - i - n$ Photodetectors

A  $p - i - n$  photodetector is a junction diode that produces current under excitation by photons of appropriate wavelength. We have noted in the description of the  $p - n$  diode that under reverse bias conditions, the current carried by the device is limited by the availability of electrons in the  $p$  material and availability of holes in the  $n$  material. Normally, these are limited by the thermal regeneration rate within the depletion region and a few diffusion lengths on both sides of the depletion region. The regeneration rate is quite low, particularly for wide-bandgap semiconductors at room temperature.

Semiconductor materials can absorb the energy of a photon by the transition of an electron from the valence band to the conduction band — i.e., by generation of an EHP. For band-to-band transitions, the minimum energy that the photon is required to have equals the bandgap energy of the semiconductor. Thus, if a  $p-n$  junction is illuminated with photons of energy equaling or exceeding the bandgap energy, an EHP is generated for each photon absorbed; and the carriers can be swept away according to the direction of the electric field in the depletion region and this carrier can contribute to the reverse current. This mechanism can be used for photodetection.

The  $I - V$  relation of a  $p-n$  diode can be divided into four quadrants. The first quadrant represents the forward bias condition; since under forward bias the current through the device is already high, the sensitivity of current to optical illumination is greatly reduced. In the third quadrant where the diode is reverse biased, the photocurrent is dependent on the optical regeneration rate and is normally independent of bias voltage in a simple model. By operating the diode in the third quadrant, and measuring current, the photon flux rate can easily be determined by scaling with previous calibration results. This is the photodetector mode of a  $p-n$  diode. In both the first and third quadrant, the device acts as a sink — dissipating power because both the voltage and current have the same signs. While the  $I - V$  relation of a diode does not enter the second quadrant, the  $p-n$  diode can operate in the fourth quadrant in the solar-cell mode. If a  $p-n$  diode is kept open circuited and is illuminated by optical flux, the photogenerated EHP separate to the  $p$

and  $n$ -sides to create an electric field measurable externally as voltage. This is known as the open-circuit voltage of the device and is limited to the value of the junction potential. Even as some current is extracted from the diode, if the photogeneration rate is higher than the extraction rate, the diode will be able to maintain a positive voltage while delivering current, thus acting as a source of power. This is the mode in which solar-cells or optical power generators work.

For a given semiconductor on which photons of a given energy are incident, the photon has a certain probability of absorption within a unit length. This probability is characterized by an absorption rate per unit length — given by the absorption coefficient  $\alpha$ . Considering band-to-band absorption only, the absorption rate becomes non-zero at the bandgap energy and goes up fast for higher-energy photons. For a simple  $p - n$  diode, the length over which photogeneration occurs is small and the absorption of a significant part of the photon does not occur over this small length. As a result, a  $p - i - n$  diode with an optimal  $i$ -layer thickness to be determined from the absorption coefficient is to be used.

For a photodetector, the most important quantity is the external quantum efficiency (EQE) at a given wavelength. Just like for the self-absorption effect in the case of the LED, the absorption of incident photons in the undepleted  $p$  and  $n$ -material is an undesirable effect in a photodetector because the carriers excited in these regions do not contribute to the photocurrent and act to reduce the EQE. It is desirable to introduce all the incident photons directly

at the  $i$  region. This is possible by use of heterostructures — if the thick  $p$  and  $n$ -type regions are made of wider-bandgap material, they will be transparent to the photons to be absorbed in the  $i$ -material. However, if it is designed in this way, the photodetector will not be sensitive to photons of energy larger than the bandgap energy of the wider bandgap material because those photons will be strongly absorbed in the bulk. Often detection of photons of much higher energy than the bandgap of the  $i$ -layer is required. Since at this much higher energy, the absorption coefficient is very large, only a very thin  $i$ -layer is used and also the thickness of the bulk layer on the illumination side has to be kept small. One example of this is the design of the UV-enhanced Si photodetector.

Another mode of operation of a  $p - i - n$  diode is in the avalanche breakdown regime. In this regime, one incident photon can create a number of EHPs by the avalanche multiplication process. Since each photon can create multiple carriers, an EQE higher than 100% is obtained in this mode. This amplification feature is known as avalanche gain. For operating in the avalanche mode, the  $i$ -layer thickness is to be selected such that the built-in field under desired reverse bias voltage equals the break-down field.

Similar to the problem of light extraction in the case of LEDs, simple optical considerations can increase the EQE for photodetectors also. For example, at each interface of different refractive index in the light path towards the absorption region, Fresnel reflection occurs, which reduces the photon flux actually reaching the absorption region. This problem can be partly reduced

by use of anti-reflection coatings.

In addition to these basic features, many other issues have to be taken into account to improve the performance of photodetectors. For example, the junction capacitance and series resistance should be minimized in order to reduce the  $RC$  time constant for improved speed. More details on the operation of  $p-i-n$  photodetectors can be found in various textbooks on electronic and optoelectronic devices [10], [11].

# Chapter 3

## Review of Nitride Research

### 3.1 Early Research in III-Nitrides

Although research in the III-nitrides has been going on for quite some time, major breakthroughs towards fabrication of electronic devices based on single-crystal epitaxial structures are quite recent. Synthesis of III-nitrides in powder form from ammonia and metallic precursors has been studied since the 1930s. Soon afterwards, researchers successfully developed GaN in single crystal needle forms by flowing ammonia gas over metallic rods. Single crystal AlN in needle form was also produced by flowing nitrogen gas over compacted AlN powder, and also by the sublimation method. The first single crystal epitaxial growth of III-nitrides was achieved in 1969 by Maruska et al. [12] using chloride vapor phase epitaxy (VPE). HCl gas was passed over metallic Ga, creating  $\text{GaCl}_3$  which reacted with ammonia to form a single-crystal GaN

film on a sapphire substrate. They also demonstrated that simultaneously transporting Zn or Mg metal with the HCl gas stream leads to incorporation of these dopants into the film. Early epitaxial efforts were based on variations of this technique and growth by MBE.

Dingle et al. [16] reported a study of the optical properties of unintentionally doped epitaxial VPE GaN in terms of absorption, reflection and luminescence. The same group also demonstrated first photopumped laser operation from GaN using GaN needles at reduced temperatures [17].

In this initial stage, material quality was seen to be quite unacceptable for device applications. The GaN films had a high background doping concentration and also a high defect density. The first major improvement in material quality was achieved by development of nucleation layer in 1983 by Yoshida et al. [13]. Using the MBE technique with sapphire substrates, they demonstrated that the quality of the GaN film was improved significantly by first growing an AlN nucleation layer. Soon afterwards, in 1986 the concept of a nucleation layer was used in GaN growth with MOCVD technology by Amano et al. [14]. They demonstrated a significant improvement in material quality of MOCVD-grown GaN if first a thin low-temperature layer of AlN is grown on the substrate before growing GaN at high temperature. Using atmospheric-pressure MOCVD technology, they observed that the material quality is strongly dependent on the low-temperature buffer layer (LTBL) thickness. Symmetric and asymmetric XRD FWHM, and PL peak intensity and FWHM were used to determine the material quality improvement. The

two-step growth was later modified to use a GaN LTBL by S. Nakamura [15] whereby a similar improvement of material quality and strong dependence on LTBL thickness was reported. It is interesting to note that to date, this two-step growth method using a GaN or AlN low-temperature buffer layer (LTBL) remains the standard method for the growth of high-quality GaN on sapphire substrates.

GaN films grown using these methods were found to be *n*-type. This result was obtained without the use of any intentional doping. Part of the nitride research community is of the opinion that the unintentional doping is due to unintentional oxygen and Si incorporation while others think this is due to a high density of nitrogen vacancy.

From the very beginning of nitride research, the unavailability of native substrates for homoepitaxy, along with the unavailability of alternate substrates for heteroepitaxy that possess the requisite properties, were identified as major limiting factors in material quality improvement. The most popular substrate for growth of III-nitrides has been sapphire, with SiC being the second most commonly used. The presence of hexagonal symmetry and a compatibility with the high temperature and corrosive chemistry used in the growth of III-nitrides, combined with the ability to grow on them material with adequate quality, have led to the prevalence of these two substrates.

Because of the large lattice mismatch between the nitrides and sapphire or SiC substrates, the epitaxial GaN film is expected to grow under a relaxed conditions at normal growth temperatures. However, as the layer is

cooled down to room temperature, due to the thermal-expansion-coefficient mismatch, most epitaxial nitride films are expected to be under some degree of strain. If grown to sufficient thickness, the epitaxial layer is often found to crack.

In order to determine growth properties in different crystalline directions, Madar et al. [18] grew GaN on a hemispherical sapphire substrate. Growth rate, surface morphology and crystal quality in different crystalline directions were studied. The authors observed that the best epitaxy was obtained with the (0001) surface, while growth on the (11 $\bar{2}$ 0) surface tilted towards the (1 $\bar{1}$ 00) axis by 10° to 20° gave reasonable quality and better surface morphology. Of the directions giving reasonable crystal quality, the highest growth rate was obtained on the (01 $\bar{1}$ 4) planes. During epitaxial growth, molecules tend to diffuse over the surface and nucleate at step edges present at the surface. For epitaxial growth, it is sometimes desirable to have a slightly off-axis substrate. This is because for an on-axis substrate, the spacing between surface steps is large, and molecules have to travel a large distance before nucleation. A slightly off-axis substrate decreases this spacing between surface steps. Hiramatsu et al. [19] studied the effect of growth on misoriented sapphire substrates. Growing on *c*-plane sapphire misoriented by 0°, 3°, 5° and 10° towards the [10 $\bar{1}$ 0] and [1 $\bar{2}$ 10] planes, the authors noted surface macrostep effects with CL and EL non-uniformities on layers grown on misoriented substrates. Grudowski et al. [20] also performed growth on misoriented substrates and observed improved luminescence properties with increased mis-

orientation. However, the defect related luminescence was also seen to increase with substrate misorientation.

Sasaki et al. [21] studied epitaxy on the (0001) Si-face and (0001) C-face of 6H SiC. The polarity of the nitride epitaxial layer was found to follow the polarity of the substrate — growth on the Si-face gave a Ga-terminated surface and growth on the C-face gave a N-terminated surface. Also, it was found that growth on the Si-face gave a smooth film while on the C-face, the film was found to be rough with hexagonal pyramidal features indicative of lateral growth and sparse surface nucleation. XRD FWHM was also found to be higher on films grown on the C-face.

Another important milestone in nitride research is the fabrication of AlGaIn/GaN heterostructures by Khan et al. [22]. Using the MOCVD technique with trimethylgallium, trimethylaluminum and ammonia as precursors, the researchers developed the first quantum-well structure in the nitride material system.

Intentional doping in GaN has been studied both in terms of the electrical properties and optical properties of doped films. Pankove et al. [23] developed the first electroluminescent device in GaN using an  $m-i-n$  Schottky diode with a Zn-doped  $i$ -layer. Since no hole injection occurs in a Schottky junction, the authors attributed the luminescence to a breakdown effect. The device emitted in the blue, and the blue emission was attributed to a deep level caused by the Zn-doping. In order to study the effect of doping on the optical properties of GaN, The same group also performed ion-implantation

of thirty-five elements in GaN, and studied their optical properties [24]. A dopant-related peak was reported to be obtained from Zn, Cd, Ca, As, Hg and Ag, while Zn was found to give the most efficient recombination center. The comparison of luminescence from Zn and Cd-doped samples grown by evaporation during chloride VPE was also investigated separately by Bergman et al. [25] and Lagerstedt et al. [26]. It was found in all of these three studies that Cd has a low solubility in GaN and therefore cannot produce sufficient compensation to produce high resistivity material for fabrication of  $m-i-n$  structures.

$n$ -type doping was found to be easily obtained by the incorporation of Si or Ge dopants. Cunningham et al. [27] presented a detailed study of the variation of the photoluminescence spectra with doping concentration in Ge-doped samples. After development of the technique to grow high-quality GaN by MOCVD using a GaN LTBL, Nakamura et al. [28] reported the growth of Si and Ge-doped GaN and discussed the effects of dopant flow on doping density, photoluminescence and XRD FWHM. Silane ( $\text{SiH}_4$ ) and germane ( $\text{GeH}_4$ ) were used as the dopant sources in this work.

Since GaN growth was estimated to have a large concentration of nitrogen vacancies, it was hoped that it would be possible to incorporate Group-IV elements in the N-sites, giving  $p$ -type doping [12]. While the work claimed reduction in electron concentration by both Si and Ge-doping, concluding that amphoteric doping is a possibility, difficulty in doing this was noted. Cunningham et al. [27] also observed a similar reduction in the the free carrier

concentration with Ge-doping.

While *n*-type doping was largely successful, the challenges of *p*-type doping were identified at an early stage. Since no dopant was seen to provide *p*-type conduction and Zn-related centers seemed to give the best luminescent properties, Zn-doping was studied extensively both in terms of growth characteristics and in terms of optical and other properties [29], [30], [31]. These studies have resulted mostly in compensated material because, on the one hand, the Zn acceptor level is deep, and incorporation was seen to spontaneously produce compensating *n*-type defects. One interesting proposal to remedy this was made by Desnica et al. [32]. A radioactive isotope of Ga, which spontaneously decays into Zn with a half-time of 78 hours, was proposed to be mixed with the non-radioactive Ga for growth of GaN. Since the radioactive Ga is chemically the same as its non-radioactive counterpart, it will essentially be incorporated in the Ga sites and subsequently decay into Zn, giving a high Zn concentration in the Ga site. No report of efforts to implement this practically has been found. It is interesting to note that a similar approach for Mg-doping by decay of radioactive Al is likely to be much more difficult. This is because the radioactive isotopes of Al that decay into Mg spontaneously have rather inconvenient half-times.  $^{24}\text{Al}$ ,  $^{25}\text{Al}$ , and  $^{26}\text{Al}$  decay into  $^{24}\text{Mg}$ ,  $^{25}\text{Mg}$ , and  $^{26}\text{Mg}$  with time constants of 2.07 sec, 7.17 sec and 10,000 years respectively.

Similar to Zn-doped GaN, the initial research on Mg doping yielded only high resistivity material and did not show any *p*-type conduction. Working on

Zn-doped GaN, Amano et al. [33] observed that low-energy electron-beam irradiation (LEEBI) increases the luminous efficiency of the sample permanently. While extending this work to Mg-doped samples, they found that LEEBI treatment converts highly doped, insulating GaN to  $p$ -type [34]. This was the first conclusive report of  $p$ -type conduction in this material system. The attention of the entire research community immediately shifted to Mg doping. In 1992, Van Vechten et al. [35] suggested that hydrogen passivation by formation of Mg:H complexes in the as-grown layer was responsible for the usual difficulty in achieving  $p$ -type conduction. Nakamura et al. [36] demonstrated in 1992 that the passivated Mg dopants can also be activated by annealing at atmospheric pressure in nitrogen environment at elevated temperatures  $\sim 900^\circ\text{C}$ . They also proposed that the effect of LEEBI or thermal annealing in a  $\text{N}_2$  environment was to drive out the passivating H atoms [37]. The discovery of Mg activation soon led both the Amano and Nakamura groups to fabricate  $p-n$  junction LEDs. Amano et al. [38] developed the first  $p-n$  junction LED in the nitrides and the  $p$ -material was activated by the LEEBI method. Soon afterwards, Nakamura et al. [39] also developed a  $p-n$  junction LED with GaN LTBL and anneal activated Mg dopants. Unlike the first group, they also presented detailed characteristics data of the LEDs, including power. At the present time, Mg is quite universally the dominant  $p$ -type dopant under use.

The development of  $p$ -type GaN essentially marked the starting point of modern nitride device research, making possible the development of various high-performance electronic devices, including injection lasers.

## 3.2 Substrate Issues and Improvement of Material Quality

It is safe to say that inadequate material quality, which is closely coupled to the unavailability of a native substrates for homoepitaxy, and  $p$ -type doping are the two biggest problems in the development of nitride materials. To a large degree, researchers have been surprised that nitride-based electronic devices have been so successful despite the high defect density inherent in the epitaxial material. Epitaxy of III-nitrides is unique in the sense that it is the only semiconductor system that has been commercialized exclusively using heteroepitaxial material. A wide variety of substrate materials has been studied for the growth of GaN including Si, ZnO, GaAs, GaP, MgAl<sub>2</sub>O<sub>4</sub>, MgO, LiGaO<sub>2</sub>, Hf, Zr, ZrN, etc. besides sapphire and SiC.

Due to heteroepitaxy, GaN epitaxial layers have to undergo a nucleation period over the substrate, and the first step towards the improvement of material quality was achieved by development of an LTBL by Amano et al. [14] and Nakamura [15]. Since growth occurs by the formation of initial nucleation islands and then by subsequent expansion and eventual coalescing of the islands, threading dislocations tend to form at the coalescing front and propagate into the film. Small angle twists and tilts among the islands are also very common. Hiramatsu et al. [40] have performed a detailed TEM study of the growth mechanism on AlN LTBL. The LTBL was determined to have an amorphous-like structure after deposition, which was found to crystallize

as temperature was raised to the temperature for GaN growth. The different stages of growth of GaN islands were also identified. Formation of threading dislocation and micropipe was also studied by Qian et al. [41] by use of scanning force microscopy and high resolution TEM.

As a result of the inherent nature of the heteroepitaxial growth mechanism, the GaN layers grown typically have a threading dislocation density of  $10^8$  /cm<sup>2</sup> to  $10^{10}$  /cm<sup>2</sup>. Comparing to a near zero threading dislocation density in commercially available high-quality Si substrates, this high density of threading dislocations on the one hand has caused surprise over the relative high performance of nitride devices, [42] and on the other hand, the high dislocation density signals the possibility of significant improvement of the technology through the improvement of the material quality.

Various research groups have proposed various techniques for improvement of material quality in epitaxially grown GaN. The density of threading dislocations reduces with increasing thickness; however, it is often found that due to accumulation of stress, the epilayers become cracked upon cool-down. Amano et al. [43] developed a multiple LTBL technique aimed towards the suppression of cracks. By placing a new AlN LTBL after every 1  $\mu m$  of GaN growth, the group was able to produce thick, crack-free GaN, and the threading dislocation density (TDD) was seen to go down with the addition of each LTBL. While AlN LTBLs were found to reduce the cracking, use of GaN BL was found to create a cracked epitaxial layer.

Of the growth technologies based upon heteroepitaxy, one approach

towards reduction of TDD is based on lateral growth. Selective-area lateral epitaxial overgrowth (SALEO) is one of the first techniques to use this idea. In this method, first a heteroepitaxial layer of GaN (or AlGa<sub>0.9</sub>N) is grown on a substrate, and then SiO<sub>2</sub> stripes of appropriate dimensions are laid on the nitride layer. A further regrowth of GaN is then carried out. During this regrowth, GaN first grows out of the windows between the oxide stripes. Then, since GaN cannot nucleate on the SiO<sub>2</sub> surface, driven by diffusion of source gas due to the resulting concentration gradient, lateral growth occurs. Under appropriate conditions and with long enough growth time, these laterally grown wings will coalesce. In this technique, since the threading dislocations tend to propagate vertically only, the laterally overgrown material is largely free of threading dislocations. As a result, only the material over the window and the material over the coalescence front will have a high density of defects. A second level of overgrowth can be performed, with the window placed over the wing material of the first overgrowth. This reduces the area of defective material, but the dislocation density at the final coalescence front cannot be eliminated, and device structures to be fabricated have to fit in so as to avoid this coalescence front.

The first report of selective area regrowth of wurtzite nitride was made by Kato et al. [44]. Using SiO<sub>2</sub> masks over GaN and Al<sub>0.1</sub>Ga<sub>0.9</sub>N, the group performed selective-area regrowth. Successful regrowth was obtained in the case of GaN and facet formation was observed. The AlGa<sub>0.9</sub>N, however, was found to nucleate on the SiO<sub>2</sub> mask in a polycrystalline form. The authors

proposed the reason for this to be a higher degree of chemical interaction between the Al species and the  $\text{SiO}_2$ . Park et al. [45] performed an extensive study of the dependence of overgrowth on different growth conditions such as stripe orientation, mask fill-factor, and growth temperature. Using MOCVD, under appropriate growth conditions, a flat-top surface and smooth vertical sidewalls were obtained for stripes oriented towards a  $\langle 1\bar{1}00 \rangle$  direction. Multilevel SALEO can also be performed with a relative rotation between mask directions, giving a significant reduction in area over which threading dislocations are present. Yu et al. [46] performed SALEO growth of GaN on both SiC and sapphire substrates; they reported on double-layer LEO with a  $90^\circ$  rotation between mask directions. Nakamura et al. [47] fabricated laser diodes on laterally overgrown substrates and obtained a significant increase in device lifetime.

The use of the oxygen-containing  $\text{SiO}_2$  mask in this technique is seen as undesirable because of the potential incorporation of oxygen. Some researchers used a  $\text{SiN}_x$  mask instead, which eliminated this problem. Another problem of SALEO is that as the lateral wings are growing, voids often form between them and the mask underneath, leading to a wavy surface morphology. To remedy this, a modification to the SALEO technique based on more complicated processing was developed, where the lateral wings grow without any contact underneath. This method is called pendeo-epitaxy because the lateral wings are effectively hanging (from the Greek word PENDEO=hang). In this technique, first a thick GaN layer is grown on appropriate substrate. Then,

usually, a patterned a dielectric mask (usually  $\text{SiN}_x$ ) and a metal mask are deposited on the epitaxial layer. The metal mask is then used to etch off the epitaxial layer upto the substrate. The metal mask is then removed, leaving the dielectric mask. The second step regrowth is then performed. In the case of SiC or Si substrates, the depositing GaN fails to wet the exposed substrate adequately and is forced to nucleate on the GaN posts. The wings usually coalesce with a slight difference in tilt angle. The first report of this technique was by Linthicum et al. [48]. Reduction of TDD was clearly observed using sectional TEM imaging. Another modification to this method was developed by Ashby et al. [49] where only one growth step is needed. In this method, the sapphire substrate was etched with trenches, and growth was performed on top of this etched substrate. GaN grown on top of the trenches begins to grow laterally under appropriate growth conditions and eventually coalesces.

The emerging technology of nitride native substrates is under development by various companies. Several efforts are in progress to commercialize the growth of bulk GaN and AlN substrates, which is expected to provide the ultimate in epitaxial material quality. Also, the availability of bulk substrate allows the use of either the N or the Ga-face for epitaxial growth, which can be useful for the control of polarization-related effects. However, the size, material quality and price of the bulk substrates available to date are not suitable for large-scale use. AlN grown by the sublimation method has been the most successful technology for the development of bulk AlN substrates so far. Slack et al. [50] reported on the sublimation growth of bulk AlN substrates from AlN

powder. Bulk AlN substrates hold two advantages over bulk GaN substrates. First, being of a larger bandgap, the substrate will be transparent to UV luminescence, allowing light collection from the backside; and secondly, since AlN has the smallest lattice constants of the nitrides, all other nitrides grown on AlN is expected to be under compression. When mismatch is unavoidable, it has been found that compressive strain is preferable to tensile strain for the reduction of defect density. Also, films under tensile strain have a tendency to form cracks.

Similar to bulk AlN substrate growth, attempts have been made towards the growth of bulk GaN crystals also. The most successful technique to date has been based on the high nitrogen pressure solution (HNPS) method.

Grzegory et al. [51] have published on the MBE growth of a GaN film over HNPS-grown substrates. The HNPS method uses a three-phase system consisting of liquid Ga, high pressure (1–2 GPa)  $N_2$ , and GaN crystal. Dissolution of  $N_2$  under these conditions leads to crystal growth. Another technique for the development of native GaN substrates is based on the growth of a thick epitaxial layer using hydride vapor-phase epitaxy (HVPE) over sapphire substrates and then separation by the use of high-power laser excitation. Kelly et al. [52] reported on the HVPE growth of GaN and subsequent laser lift-off. The separation was performed without the introduction of any cracks and the use of high temperature (600°C) for the lift-off environment allowed for the elimination of any bowing.

### 3.3 Doping of III-Nitrides

Doping of III-nitrides, particularly AlGa<sub>x</sub>N with a high Al concentration, is an important problem faced by the nitride research community. While *p*-type doping is clearly the more difficult side of this problem, the problem of doping *n*-type is also yet to be solved — at least for AlGa<sub>x</sub>N with high Al content. While studying Al<sub>x</sub>Ga<sub>1-x</sub>N grown on SiC substrates, Bremser et al. [53] noted that for  $0.12 \leq x \leq 0.42$ , controlled Si-doping was achievable. However, with  $x > 0.42$ , doped material was too resistive. This is peculiar because Si is a shallow donor for AlGa<sub>x</sub>N and significant discontinuity in resistivity for AlGa<sub>x</sub>N with varying Al content is not expected. Stampfl et al. [54] performed a detailed theoretical analysis of Si-doping of AlGa<sub>x</sub>N and proposed that in AlGa<sub>x</sub>N with high Al content, oxygen impurity can form a donor complex (DX) so that normal shallow donors, e.g. Si do not contribute to the free electron contribution. Also, for these compositions, an Al vacancy can act effectively to compensate any intentional *n*-type dopants such as Si. A variety of efforts have been expended to obtain a low resistivity *n*-type conduction in AlGa<sub>x</sub>N of high Al content because of its importance in order to extend device operation to the short wavelength side of the potential wavelength range of AlGa<sub>x</sub>N material. Adivarahan et al. [55] reported on the use of isoelectronic In doping along with Si which allows reduction of resistivity significantly. It was also noted that incorporation of a small amount of In allows growth of thick, highly Si-doped layers without causing cracks. Despite some success by

several researchers, it still remains to be seen how high in Al composition it is possible to go while maintaining a low resistivity  $n$ -type conductive AlGaIn layer.

While the problem with  $n$ -type doping has been difficult in this material system and the research community still holds out hope for it, it is not an exaggeration to say that obtaining a reasonable  $p$ -type conduction in AlGaIn with high Al content has been impossible. Also, contrary to the problem with  $n$ -type doping, the problem with  $p$ -type material is much more fundamental — the Mg acceptor level in the AlGaIn material system is quite deep. The depth of the acceptor level from the valence band edge is  $\sim 200$  meV for GaN and this goes deeper fast with addition of Al in the AlGaIn alloy [56]. As a result, at room-temperature, GaN or AlGaIn doped with acceptors (e.g. Mg) remains in the freeze-out region where activation of acceptors is incomplete and free hole concentration obtained remains very small. This low hole concentration leads to a high resistivity in  $p$ -type layers in devices as well as a low mobility and short minority carrier diffusion length in  $p$ -type material due to the need of excessive acceptor concentration to achieve a reasonable free-hole concentration and the difficulty in obtaining good hole injection for LED fabrication.

A number of approaches have been proposed and studied to obtain enhanced acceptor activation in this material system. Most notable of these are codoping, valence-band modulation by use of superlattices, and illumination with infrared (IR) luminescence. Codoping an acceptor along with some

other acceptor or even a donor has the potential of yielding low-resistivity  $p$ -type conduction by obtaining of higher acceptor solubility limit, by modifying acceptor ionization energy and by reducing the solubility of compensating hydrogen [57]. In two independent research efforts, Korotkov et al. [58] and Kipshidze et al. [59] reported the increase in  $p$ -type conductivity by codoping with O. Kim et al. [57] studied the codoping of Mg with Zn, and while the free hole concentration level achieved is below other reported free hole concentrations for Mg doping alone, Zn doping was seen to improve the free-hole concentration. Also, the codoping was found to give the additional benefit of lowering the specific contact resistance for common Pd/Au metallic contacts to  $p$ -type GaN.

Use of short-period superlattices (SLSes) has the potential to improve acceptor activation. Due to the modulation of the valence band because of the heterojunction and the piezoelectric field, parts of the valence band can be made to cross the Fermi level resulting in a high acceptor ionization. The use of SLSes to enhance the acceptor ionization was first proposed by Schubert et al. [60]. While in this analysis the researchers did not consider the polarization field, Kozodoy et al. [61] in a later publication mentioned that the polarization field will enhance the effect. Saxler et al. [62] performed a variable-temperature Hall-effect measurement and optical absorption measurements on GaN:Mg, AlGaIn:Mg and Mg-doped GaN/AlGaIn SLS and noted that reduction in the effective activation energy is obtained by use of SLS. While the Hall-effect measurement essentially measures conductivity parallel

to a surface, it is more important to achieve a reduction in the vertical conductivity for most electronic device applications, and it was questioned whether the presence of barriers for conduction in an SLS has an adverse effect on vertical conduction. By comparing the current-voltage (I-V) characteristics in a set of vertical conduction test structures, Zhu et al. [63] observed that the SLS structure also contributes to reduction of the vertical resistance.

Another approach proposed by some researchers involves the incorporation of an infrared (IR) lamp with nitride devices that will emit light that is absorbed by the nitride material. It is proposed that the IR photons will activate the holes from the acceptor level to the valence band [64]. Data on efforts to implement this in practice are yet to be published.

### 3.4 Nitride Photodetectors

A variety of photodetectors have been fabricated in the nitride material system. These include photoconductors,  $p-i-n$  photodiodes, Schottky photodiodes,  $p-i-n$  avalanche photodiodes and phototransistors. The early work on nitride-based photodetectors was based on GaN and was performed in the early 1990's. With the state of knowledge of the nitride materials at that time, fabrication of photodetectors using the material system was confined to various simple device structures. The first report of a photodetector based on the nitrides was made by Khan et al. [65]. These researchers used a high-resistivity GaN layer grown by a special technique to fabricate pho-

toconductors. The devices displayed sharp cut-off in detectivity below the GaN bandedge and also showed photoconductive gain. The same group also fabricated the first Schottky junction photodiode in the nitride material system [66]. One Schottky barrier and another ohmic contact were placed on a GaN:Mg layer, to form a Schottky diode. The devices were illuminated from the back-side (substrate-side). Using GaN, Chen et al. [67] from the same research group also fabricated the first  $p - n$  junction photodetector in this material system.

Due to a sharp cut-off in the detectivity at wavelengths longer than that corresponding to the GaN bandgap ( $\sim 365$  nm), all these devices were visible-blind. After the development of simple visible-blind photodetectors, the next challenges remained in the development of avalanche photodetectors and phototransistors in the visible-blind range and the development of solar-blind photodetectors.

Fabrication of avalanche photodetectors was found to be difficult because of the high leakage current and the micro-plasma breakdown in fabricated  $p - n$  junctions before the avalanche condition is achieved. The reason for this is that the material has a high TDD. Only one conclusive report of avalanche photodetector seems to be present in the literature. Yang et al. [68] demonstrated conclusive avalanche operation of a GaN  $p - i - n$  diode. The fabricated devices demonstrated an abrupt breakdown at  $\sim 105$  V and a highest gain of 23 was achieved. The development of GaN/AlGaN-based heterostructure phototransistors has also been reported [69], [70].

GaN-based photodetectors are however, not suitable for all purposes. Particularly, as mentioned before, “solar-blind” photodetectors insensitive to radiation of wavelengths shorter than  $\sim 290$  nm are of increasing interest. The defense industry is particularly interested in back-illuminated solar-blind imaging arrays to be flip-chip bonded to electronic circuitry.  $p-i-n$  diode structures are also preferred over Schottky junction detectors because  $p-i-n$  photodetectors can operate at low or zero bias voltage, obviating bulky power supplies.

Fabrication of these devices can be challenging. First, due to adduct formation between ammonia and trimethylaluminum (TMAI), AlGaN growth is seen to be highly dependent upon the growth pressure and temperature [71]. Incorporation of Al in the film depends on these factors, and material with high Al content, compositional uniformity, and quality becomes difficult to obtain. For a wide range of growth pressures, no or little Al incorporation occurs, limiting the growth conditions to a narrow pressure range. A high degree of compositional uniformity is often found to be difficult to achieve. Furthermore, obtaining a high quality AlGaN layer as well as the reduction of oxygen incorporation is often found to be inadequate for some device applications. In addition, the doping efficiency is low because, with increasing Al concentration in AlGaN, the dopant levels get deeper and material quality is seen to deteriorate [54]. Just like for the case of visible-blind photodetectors, in the photovoltaic form, SBDs can also be fabricated either using Schottky junction or  $p-n$  junction. Li et al. [72] reported the fabrication and prop-

erties of Schottky junction SBDs operation based on AlGaIn material. One advantage of Schottky junction devices is that problems with doping does not need to be addressed.

Various research groups have demonstrated back-illuminated solar-blind photodetectors (SBDs) [73], [74], [75], [76], [77]. The structure used is generally a  $p-i-n$  diode made of  $\text{Al}_{0.45}\text{Ga}_{0.55}\text{N}$  on a defect reduction window layer of  $\text{Al}_{0.60}\text{Ga}_{0.40}\text{N}$  grown on a sapphire substrate polished on both sides. An anti-reflective (AR) coating may be used on the backside of the substrate to reduce the loss of incoming light by Fresnel reflection. The desired properties for these photodetectors are, in order of priority, high external quantum efficiency at low or zero bias, high detectivity (this requires a low dark current density), high rejection of wavelengths longer than  $\lambda \sim 290$  nm, and high speed. The present work describes the next generation research on this field leading to fabrication of high-performance solar-blind imaging arrays.

### 3.5 Nitride Light Emitting Diodes and Lasers

The history of electroluminescent devices in the nitride semiconductors goes back to early 1970s. The first nitride-based electroluminescence device (i.e. an LED) was developed by Pankove et al. [23] using a Schottky barrier made on Zn-doped GaN. From this time until the development of  $p$ -type GaN by Amano et al. [34], the common approach used towards fabrication of nitride LEDs was use of Schottky junction with material doped with appropriate

impurities.

The next major step in nitride LED technology was the development of a GaN  $p - n$  homojunction LED by Amano et al. [38] made possible by the development of  $p$ -type GaN. After this development, significant work was dedicated by research groups all over the world towards development of an InGaN-based blue LED and laser. A number of groups reported development of InGaN-based blue LEDs and many steps of improvement of characteristics were reported. Progression of nitride-based light emitters in this time period was achieved largely by the Nitride Semiconductor Research Laboratory of Nichia Corporation. In 1994, Nakamura et al. [78] reported on InGaN/AlGaIn double-heterostructure (DH) blue LED with output of 1 cd. The InGaIn constituting the active region in this device was Zn-doped to improve luminescence. The same research group extended the device to slightly longer wavelength using higher In content  $\text{In}_{0.23}\text{Ga}_{0.77}\text{N}$  in the active layer. Development of blue-green LEDs based on InGaIn/AlGaIn DH with a high EQE of 2.4 % and a luminous intensity of 2 cd was developed [79]. The active region of these devices were doped with both Si and Zn to improve luminescence. These blue and green high performance LEDs were soon commercialized successfully. Intensive effort was dedicated to improve device performance and also to extend the wavelength of emission both to the longer wavelength side and to the shorter wavelength side. Nakamura [80] developed an InGaIn/AlGaIn DH based violet-blue LED. The same research group developed single quantum-well (SQW) structures emitting in blue, green and yellow [81], [82]. The use of

improved device structure significantly improved performance of the blue and green LEDs. Also, the yellow LED emitting at a peak wavelength of  $\sim 590$  nm reported in this work was the longest wavelength light emitter from the nitride system at that time. Going from blue towards yellow, clear reduction in output power was observed which was attributed to difficulty in obtaining good quality InGaN with high In content. These LED devices were to target the green to yellow LED market traditionally dominated by phosphide based semiconductor LEDs.

Among other efforts, Song et al. [83] developed InGaN-based MQW blue vertical resonant cavity LED by depositing  $\text{HfO}_2/\text{SiO}_2$  distributed Bragg reflector (DBR) on top. For bottom mirror, the epitaxial layer was first separated from the substrate by use of a pulsed excimer laser. Then, a high reflective indium-tin oxide (ITO) transparent contact was deposited on the backside and the structure was mounted on a copper substrate. Since the back-mirror fabrication in this method is quite process-intensive, an alternate design using an AlGaN/GaN DBR grown epitaxially was developed to fabricate a resonant cavity LED emitting in the violet [84]. By use of a tunnel-junction, Ozden et al. [85] developed a three-terminal bicolor LED that was grown in one epitaxial run. The two InGaN active regions emitted at 470 nm and 535 nm respectively, and the  $n$ -contact to the top diode and the  $p$ -contact to the bottom diode were accessed from the same electrode by use of tunneling in the  $p^+ - n^+$  tunnel junction.

While at this stage, InGaN-based LEDs emitting in the visible part of

the optical spectra had been largely commercialized, the next step was to fabricate GaN, AlGa<sub>N</sub> and InAlGa<sub>N</sub>-based LEDs emitting in the UV. The issues involved for the shorter wavelength emitter, though, can be challenging. First, obtaining low resistivity material becomes difficult because of the doping issue. Next, AlGa<sub>N</sub> material grown with present technologies have been found to have a low luminescence compared to InGa<sub>N</sub>. Coli et al. [86] performed a detailed analysis of optical processes in AlGa<sub>N</sub>. It was noted that PL intensity goes down with increase of Al content in the alloy due to increase in non-radiative processes. Also, with AlGa<sub>N</sub>, control of oxygen incorporation becomes more difficult because with higher Al content, the material develops an affinity for oxygen. Naturally, therefore, the progress towards UV LED began with the lower Al-content alloys. Nishida et al. [87] of NTT Basic Research Laboratories reported output power of more than 0.1 mW from an AlGa<sub>N</sub> MQW structure. The peak of emission spectra was at 350 nm and the device structure incorporated a *p* and *n* SLS to obtain low-resistivity. The structure was grown on SiC substrate by use of conducting buffer layer. Extending this work, the same group also published on milliwatt operation of AlGa<sub>N</sub> SQW UV LEDs emitting at 342 nm [88]. Kinoshita et al. [89] demonstrated an AlGa<sub>N</sub>-based LED structure grown on SiC substrate emitting at 333 nm. The basic structure employed was similar to the structure used by Nishida et al. [87], however, a bulk-*n* layer was used instead of an *n*-SLS. The nitride research group at the University of South Carolina has developed InAlGa<sub>N</sub> MQW-based LEDs emitting at a variety of wavelengths [90], [91].

The group has used a unique pulsed epitaxial technique for growth of the quaternary InAlGa<sub>N</sub> and has proposed that incorporation of In in the active region greatly improves light emission. These devices make use of an In-Si co-doping scheme to obtain a low-resistivity *n*-type layer [55]. More recently, the same group has developed high performance UV LEDs based on AlGa<sub>N</sub> QWs emitting at  $\sim 324$  nm [92] and  $\sim 285$  nm [93]. An AlGa<sub>N</sub>/AlN superlattice was used in these structures that allow growth of thick AlGa<sub>N</sub> layers without causing cracks [94]. For fabrication of LEDs, one important factor is reduction of forward resistance since a high forward resistance causes significant ohmic heating. For LED structures with both contacts made from the top, the main contributing factor to the resistance is usually the lateral spreading *n*-layer. Since the AlGa<sub>N</sub> requisite for use in deep UV LEDs is difficult to dope highly *n*-type, development of a low resistivity *n*-layer using AlGa<sub>N</sub> with high Al content becomes an important issue. A detailed analysis on this issue was done by Shatalov et al. [95] who concluded that for high power devices, stripe geometry is more suitable for improvement of the current-crowding issue. The present work also describes more study on development of AlGa<sub>N</sub> UV-LEDs.

The first injection laser in the nitride system was developed by Nakamura et al. [96]. The device was an InGa<sub>N</sub>-based MQW structure that lased at room temperature under pulsed conditions. The laser emitted at 417 nm (blue) and was the shortest wavelength of emission for a semiconductor laser at that time. Other groups also have reported InGa<sub>N</sub>-based laser structures emitting in the blue. Akasaki et al. [97] developed an InGa<sub>N</sub> SQW laser diode

that operated in pulsed operation and emitted at  $\sim 376$  nm. This was the first report of a UV laser based on the material system. While other research groups also succeeded in fabricating nitride lasers emitting in blue [98], [99], [100], the Nichia research group's progress occurred at a much faster pace leading to commercialization of continuous-wave blue lasers in 1998. Their recent work includes fabrication of a long-lifetime continuous-wave (CW) near-UV laser consisting of GaN (SQW) [101]. The shortest wavelength nitride injection laser to date was also developed by Nichia — using the quaternary  $\text{In}_{0.03}\text{Al}_{0.03}\text{Ga}_{0.94}\text{N}$  SQW structure, Nagahama et al. [102] demonstrated CW injection lasing at  $25^\circ\text{C}$  and emitting at 366.4 nm (near UV).

# Chapter 4

## Development of the SBD and UV LED

### 4.1 Introduction

The present work was performed based on the foundation of previous research performed in Prof. R. D. Dupuis' research group. This includes modification of the MOCVD reactor, optimization of basic material quality, and development of miscellaneous electronic devices based on the III-nitrides.

InGaN-based quantum wells, blue LEDs and photo-pumped laser structures were developed by Grudowski et al. [103], [104]. GaN-based MSM photodetectors with ultralow dark current was developed on GaN single crystal epitaxial layer on sapphire substrates [105]. Photodetectors developed using GaN  $p-i-n$  structures were also reported having record low dark current

and a high EQE of 35% [103]. Heterojunction field-effect transistors based on GaN/AlGaN heterostructure with modulation doping were also demonstrated [103], [106]. High-performance avalanche photodetectors based on GaN were developed using a  $p-i-n$  structure on sapphire substrates [107]. AlGaN/GaN heterojunction bipolar transistors were fabricated by Shelton et al. [108]. Li et al. [72] demonstrated solar-blind operation from Schottky junction MSM photodetectors based on AlGaN. Lambert et al. [77] have performed extensive investigation of  $p-i-n$  SBD based on AlGaN and have obtained high EQE.

The present work was, in part, an extension of this previous work in the specific areas of improving the performance of SBDs and fabrication of UV LEDs.

## 4.2 Material Growth

### 4.2.1 Growth Conditions

In order to successfully fabricate a device from an epitaxial structure, the growth conditions of different layers or components of the structure first need to be established. The epitaxial layers to be discussed here were grown by low-pressure MOCVD in an EMCORE Model D125 UTM rotating disk reactor on  $c$ -plane sapphire and SiC substrates. Substrate heating is performed by a two-zone resistive heater controlled by Eurotherm PID temperature controllers. The reactor is equipped with two pyrometers for accurate and repro-

ducible temperature measurement and one in-situ reflectance monitor. The system is equipped with purifiers for hydrogen, ammonia and nitrogen.

The growth occurs in a  $H_2$  ambient employing the primary precursors trimethylgallium (TMGa), trimethylindium (TMIn) and trimethylaluminum (TMAI) as alkyl sources and ammonia as the hydride source. Silane ( $SiH_4$ ) is used as a source of Si for *n*-type doping and bis-cyclopentadienyl magnesium ( $Cp_2Mg$ ) is used as a source of Mg for *p*-type doping. The growth pressure ranged from 50 to 200 Torr. For growth on sapphire, a two-step growth was used beginning with a low-temperature GaN or AlN nucleation layer grown at  $\sim 535^\circ C$  followed by growth at high temperature ( $\sim 1050^\circ - 1070^\circ C$ ). Mg-doped samples were in-situ annealed in a nitrogen ambient at  $850^\circ C$  for 10 min to activate the Mg acceptors by driving out the hydrogen. Structures grown on SiC substrates were also grown in two steps; the buffer layer in this case, however, was a high-temperature-grown AlN layer. The growth conditions are summarized in Table 4.1.

### 4.2.2 Material Requirements

A variety of material quality criteria are required for growth of AlGaIn-based photodetectors. First, the material quality has to be good and the dislocation density has to be low enough so that the leakage current is not excessive and the carriers can actually get swept across the depletion region. For the purpose of a UV LED, high material quality is also needed in order to reduce non-radiative recombination processes. This high material quality

<b>Growth temperature for epitaxial layers</b>	1050 – 1100°C
<b>Growth temperature for LTBL</b>	~ 535°C
<b>Growth temperature for high temperature BL</b>	~ 1110°C
<b>Growth pressure</b>	50 – 200 Torr
<b>Ga-precursor</b>	Trimethylgallium (TMGa)
<b>Al-precursor</b>	Trimethylaluminum (TMAI)
<b>In-precursor</b>	Trimethylindium (TMIn)
<b>N-precursor</b>	Ammonia (NH <sub>3</sub> )
<b>Si-dopant precursor</b>	Silane (SiH <sub>4</sub> )
<b>Mg-dopant precursor</b>	Bis-cyclopentadienylmagnesium (Cp <sub>2</sub> Mg)

Table 4.1: Conditions used for MOCVD growth.

on one hand means a low dislocation density and on the other hand means keeping impurities, particularly oxygen, to a minimum level since these act as non-radiative recombination centers. Accurate control of the alloy composition is also desirable.

For the purpose of fabrication of an SBD, the  $p$ -layer thickness can be allowed to be small — as a result, a low-resistivity  $p$ -type layer is not a prime requirement. However, the ability to grow  $p$ -type AlGaN is absolutely needed for the formation of the required  $p - n$  junction. On the other hand, for development of a UV LED, the  $p$ -layer has to be of sufficient thickness so that the active region is not too close to the surface and  $p$ -contact metallization. Also, since the LED is a minority carrier injection device and the hole injection is directly proportional (in a simple approximation) to the hole concentration on the  $p$ -side, a highly  $p$ -doped low-resistivity layer is required.

The resistivity of the  $n$ -layer needs to be reduced and kept strictly under control for both the SBD and UV LED devices. For both these devices in mesa geometry, the  $n$ -layer is supposed to effectively spread the current between the electrode and the device active region, and device series resistance depends largely on the resistivity of the  $n$ -layer. For the SBD, the EQE at zero volt bias involves a short-circuit measurement of current driven by the voltage source created by photogeneration. A high series resistance in the  $n$ -layer will essentially reduce this short-circuit current, effectively giving a low EQE. For the UV LED, the need is even higher because contrary to an SBD, an LED is operated under much higher current conditions. As a result, an ohmic voltage drop and the resulting heating along with current-crowding towards the edge of the mesa becomes a big problem. If using an  $n$ -type SiC substrate, a back-side contact can be used, which eliminates the problem of current-crowding. Also, for the SBD, the  $n$ -layer should be of high enough bandgap so that it does not absorb the light at wavelengths of interest. In case of a UV LED grown on a sapphire substrate, a high enough bandgap in the  $n$ -material so that it is transparent to the generated photons is needed if light is to be extracted from the back side of the substrate.

Unlike the SBD, the active region of a UV LED typically contains quantum wells and superlattices. For this purpose, high-quality interfaces along with good control of the layer thickness is required.

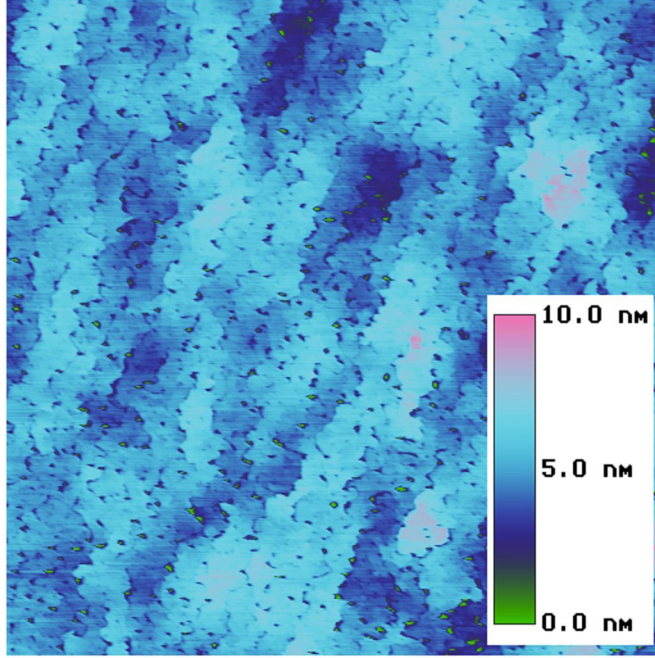


Figure 4.1: AFM image of a typical AlGaIn surface on sapphire in  $5\ \mu\text{m} \times 5\ \mu\text{m}$  scale (sample M2983).

### 4.2.3 Development of High-Quality AlGaIn

The growth conditions for high-quality AlGaIn were optimized both on sapphire substrate and on SiC substrates for use in the devices. The layers were characterized with AFM, CL, XRD, SIMS, TEM, and optical transmittance measurements. A typical surface morphology of an AlGaIn film grown on sapphire with an AlN LTBL is shown in Figure 4.1. The root-mean-squared (RMS) roughness is 1.173 nm. Figure 4.2 shows a SIMS profile of an AlGaIn SBD sample. The oxygen profile is of particular interest. At surface, due to incorporation from atmosphere, a fast decaying oxygen profile is seen. Also,

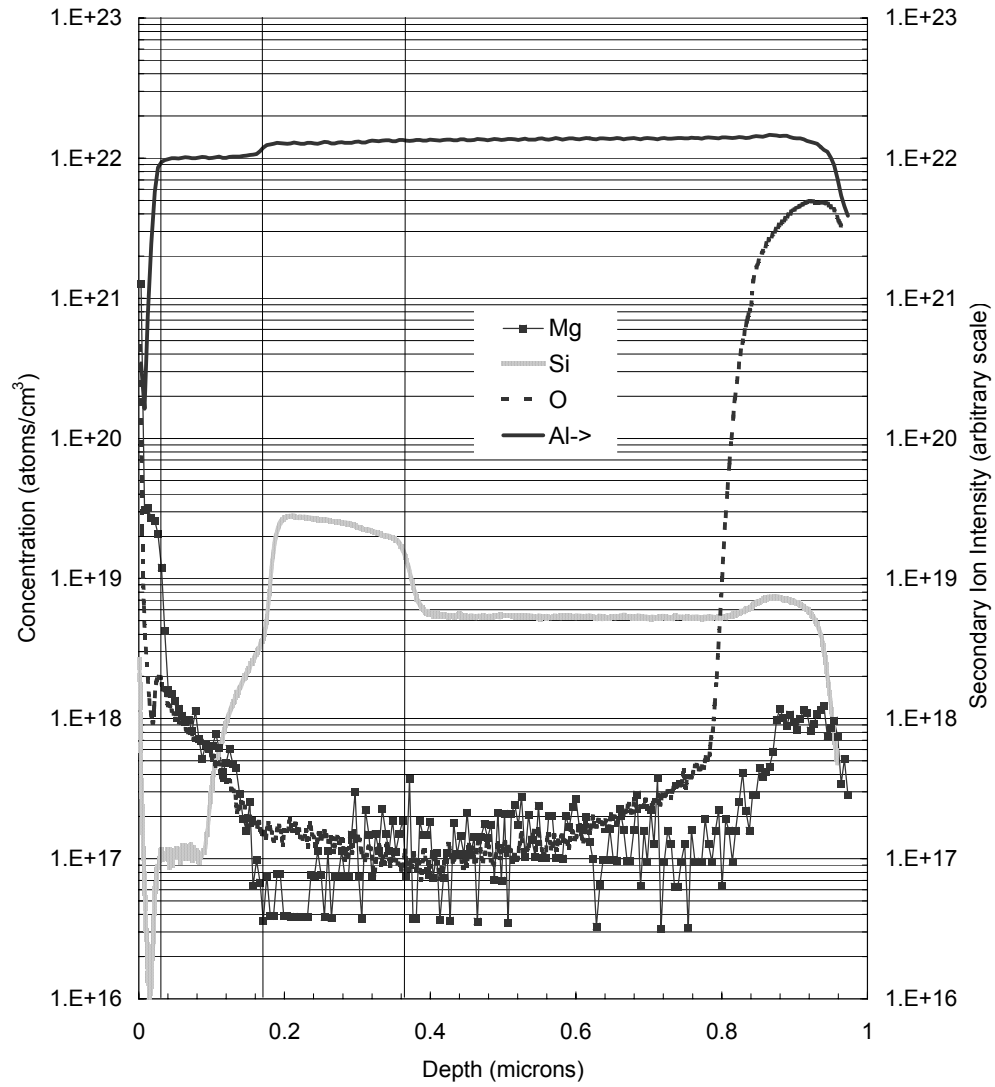


Figure 4.2: SIMS profile of an SBD device showing low oxygen content (sample M2510).

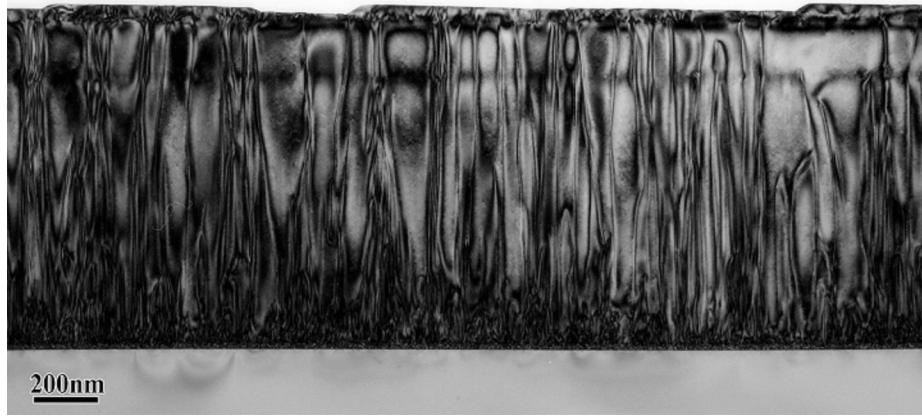


Figure 4.3: TEM image of thick AlGaIn layer in an SBD device showing dislocations and reduction of dislocation density with epitaxial growth (sample M2510) (Measurement by D. N. Zakharov and Z. L. Weber; Lawrence Berkeley National Laboratory).

as the profile approaches the sapphire substrate, the oxygen count again goes up because of the sputter hole reaching the substrate. In between, the oxygen count remains almost flat at a value of  $\sim 1 \times 10^{17} / \text{cm}^3$ , which is the detection limit of oxygen for this material. Also, the Al profile shows a dip as the Al-content changes. The oxygen profile is not seen to follow the Al-composition. Since Al has a high affinity to oxygen, the oxygen profile is usually seen to follow the Al profile if significant oxygen is present in the film. The cross-sectional TEM image of an SBD device is shown in Figure 4.3. The threading dislocation density was calculated to be  $4 \times 10^9 / \text{cm}^2$  near the top of the epitaxial layer, which is indicative of high-quality AlGaIn material by the standard of present technology. The image also shows that a large TDD is generated at the interface between the substrate and the epitaxial layer, and some of the

dislocations annihilate as the epi-layer grows in thickness.

With an XRD technique, a FWHM of  $< 400''$  was obtained for a symmetric (004)  $\omega - 2\theta$  scan for an  $\text{Al}_{0.6}\text{Ga}_{0.4}\text{N}$  layer of  $\sim 450$  nm thickness. Optical transmittance measurements showed sinusoidal oscillations for wavelengths below bandgap and a sharp decay near the bandgap energy (characteristic transmittance drop-off from some of the AlGa $\text{N}$  calibration samples is shown in Figure 4.6).

One important issue regarding calibration of AlGa $\text{N}$  material is determination of the composition and strain state. A set of thick AlGa $\text{N}$  layers were measured using optical transmittance and XRD. First, a number of AlGa $\text{N}$  layers with different Al compositions were grown on sapphire substrate using an AlN LTBL. Then, optical transmittance measurements were performed on the samples, which provides the bandgap information. Then, a reciprocal space map around the (205) reflection was measured, after which an  $\omega - 2\theta$  scan was performed around the (002) reciprocal space point without changing the  $\phi$ -angle. The (002) scan essentially determines the  $c$ -lattice constant of the epitaxial layer. Also, since there can be an arbitrary tilt in  $\omega$ -angle while mounting the sample (zero reference error of the goniometer can also contribute to this) and since  $2\theta$  should be exactly twice the  $\omega$ -angles for a symmetric scan, the center  $\omega$  and  $2\theta$ -angles for the scan allow correction for the arbitrary tilt. The peak position of the (205) RSM also needs to be corrected for this tilt, and since no  $\phi$ -rotation occurred between the (205) scan and the (002) scan, tilt correction is done simply by subtraction. The peak

position in the RSM allows determination of the  $c$  and  $a$ -lattice constants. At this point, the wafer characterization data obtained are:

- $c_{(002)}$ : the  $c$ -lattice constant obtained from (002)  $\omega - 2\theta$  scan.
- $c_{(205)}$ : the  $c$ -lattice constant obtained from (205) RSM scan.
- $a_{(205)}$ : the  $a$ -lattice constant obtained from (205) RSM scan.
- Optical absorption cut-off wavelength.

Applying Vegard's law to the first three of these data sets and using the relationship between bandgap energy and Al-content for the fourth data set, four independent estimates of  $x$  in  $\text{Al}_x\text{Ga}_{1-x}\text{N}$  can be obtained. These estimates of  $x$  are named  $\text{Al}_{c-(002)}$ ,  $\text{Al}_{c-(205)}$ ,  $\text{Al}_{a-(205)}$ , and  $\text{Al}_{\text{xmn}}$  respectively. For various samples, these four quantities are then plotted together against  $\text{Al}_{\text{xmn}}$  in Figure 4.4. The expectations from this plot are:

- $\text{Al}_{c-(205)}$  should be the same as  $\text{Al}_{c-(002)}$ , since both the XRD measurements should yield the same  $c$ -lattice constant.
- $\text{Al}_{c-(205)}$  should be smaller (or larger) than  $\text{Al}_{a-(205)}$  if the epitaxial layer is under compressive (or tensile) stress.
- If the layer is under strain, the quantity  $\text{Al}_{\text{xmn}}$  will show dependence accordingly. Or conversely, if there is no strain, it should align with the other three estimates of Al-content.

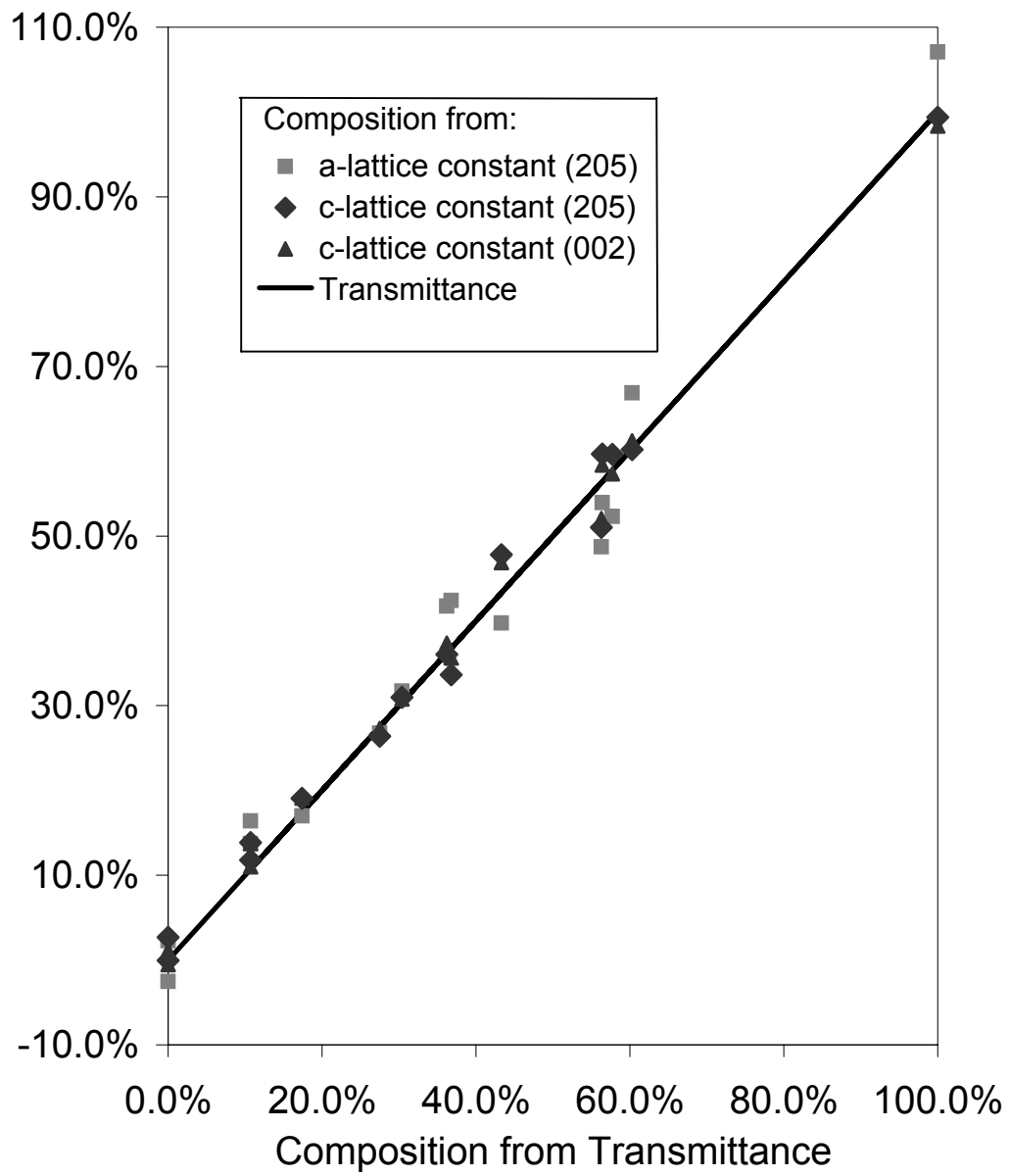


Figure 4.4: Correlation of Al-content in AlGaIn from different methods.

It is curious to note in Figure 4.4 that all the alloy composition estimates are in approximate agreement. Attempt was made to correlate deviations with various factors such as film thickness, Al-content in the AlGa<sub>N</sub>, etc., but no strong correlation was found, which seems to indicate that, within the limits of accuracy in measurement, the films studied are fully relaxed.

#### 4.2.4 Development of Low Resistivity AlGa<sub>N</sub>:Si

As mentioned before, development of a low-resistivity *n*-type AlGa<sub>N</sub> layer with high enough Al-content is a prime requirement for both the SBD and UV LED device. From the perspective of these devices, therefore, an ideal *n*-layer should not absorb light at the wavelengths the device is designed to operate at. For the purpose of the SBD, the wavelength of interest is  $\sim 290$  nm. For an LED, the required bandgap depends on the emission wavelength desired, and for emission around  $\sim 290$  nm, the transparency requirement of the *n*-layer is the same as for an SBD: the wavelength of 50% transmittance (to be denoted by  $\lambda_{1/2}$ ) should be less than  $\sim 270$  nm. Compared to an SBD device, an *n*-layer of sufficient thickness to obtain a low enough resistivity is required since an LED carries a higher current. The high Si-doping required to obtain a low-resistivity layer often leads to material-quality degradation and even cracking if grown to excessive thickness.

In order to serve these purposes, the growth of *n*-type AlGa<sub>N</sub> layers having an appropriate alloy composition was studied. For use in SBDs and  $\sim 290$  nm LEDs, the AlGa<sub>N</sub>:Si+ was calibrated to have a  $\lambda_{1/2} \sim 267$  nm

corresponding to an  $x \sim 0.52$  in  $Al_xGa_{1-x}N$ . Figure 4.6 shows the optical transmittance spectra of this AlGa $N$  layer grown on a thick AlGa $N$ :ud layer of higher Al-content. Compared to other AlGa $N$  layers, the transmittance drop-off at band-edge is seen to be slightly less sharp. A variable-temperature Hall-effect measurement was performed on the calibration AlGa $N$ :Si+ samples yielding a room-temperature mobility of  $6.5 \text{ cm}^2/\text{V} - \text{sec}$  and carrier concentration corrected by SIMS was found to be  $2.3 \times 10^{19} / \text{cm}^3$ . The Hall-effect data is shown in Figure 4.5. The mobility decreased slightly with temperature while the carrier concentration remained almost constant. The absence of an Arrhenius type dependence of carrier concentration seems to indicate that either the donor band is merged with the bottom of the conduction band by degenerate doping or that the conduction is occurring inside the donor band. The AlGa $N$ :Si layer was successfully grown up to  $\sim 400 \text{ nm}$  thickness without any noticeable degradation of material quality. As a result, this low-resistivity AlGa $N$  material is very suitable for use in SBDs and deep-UV LED applications.

Another issue related to the AlGa $N$ :Si+  $n$ -contact layer is the development of a low-resistance ohmic contact to the material. Contacts to the AlGa $N$ :Si+ material grown were studied by Readinger et al. [109] who successfully obtained a very low-resistance ohmic contact to the material using a vanadium-based metalization scheme. The complete metal stack of V/Al/Pt/Au was shown to be capable of giving a very low specific contact resistance of  $4 \times 10^{-5} \Omega - \text{cm}^2$ . The ability to obtain a high conductivity layer

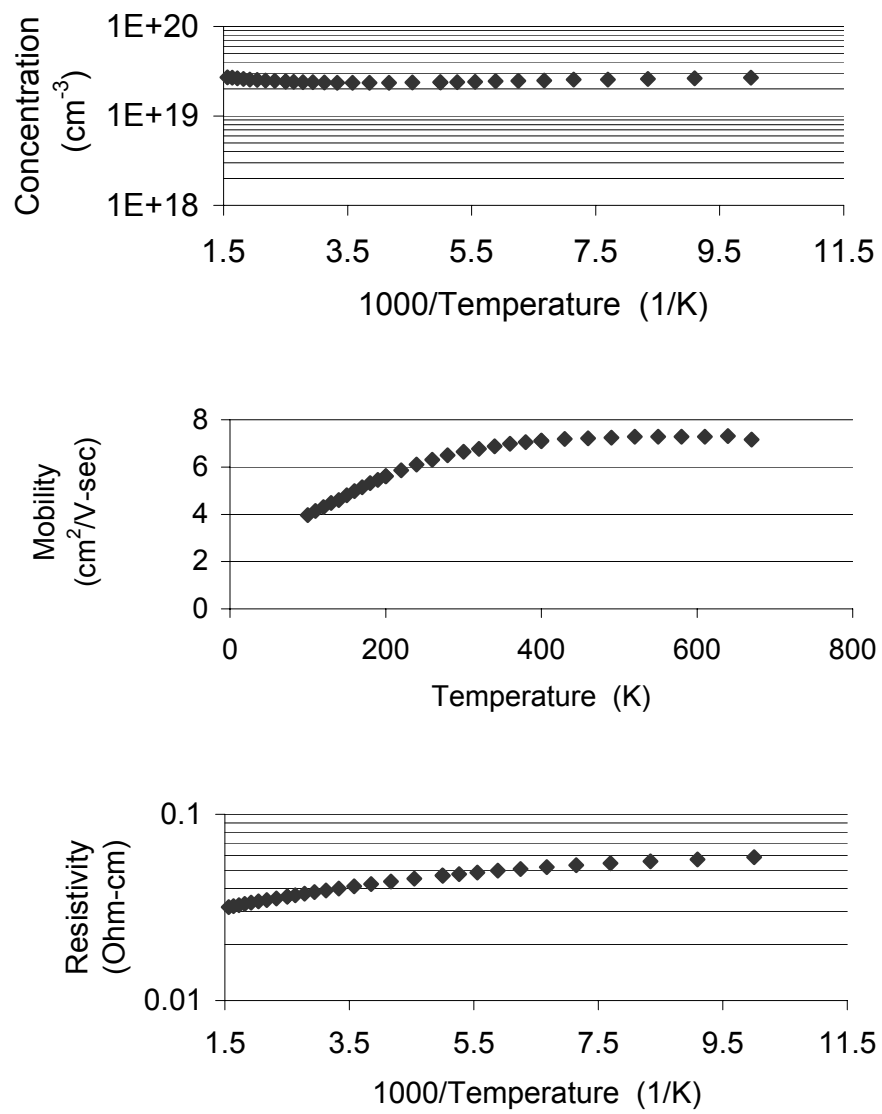


Figure 4.5: Variable temperature Hall-effect measurement on an AlGaIn:Si+ layer. (Measurement by W. Götz; Lumileds Lighting).

along with a metallization scheme with low specific contact resistance is a major step towards development of devices using these AlGaN alloys with high Al-content.

#### 4.2.5 Other Issues Related to SBDs

For successful development of an SBD, it is important to design the device structure with the careful investigation of a variety of issues. The device structure used in the present work was, beginning with the top layer:

- $\sim 25$  nm GaN : Mg top  $p$ -contact layer
- $\sim 10$  nm  $\text{Al}_{0.42}\text{Ga}_{0.58}\text{N}$  : Mg
- $\sim 150$  nm  $\text{Al}_{0.42}\text{Ga}_{0.58}\text{N}$  : ud absorption region
- $\sim 15$  nm graded AlGaN : Si+
- $\sim 100$  nm  $\text{Al}_{0.52}\text{Ga}_{0.48}\text{N}$  : Si+  $n$ -contact layer
- $\sim 700$  nm  $\text{Al}_{0.52}\text{Ga}_{0.48}\text{N}$  : Si- template layer for reduction of TDD
- AlN LTBL
- on both-side polished  $c$ -plane sapphire substrate

The absorption region of the device is made of  $\text{Al}_{0.42}\text{Ga}_{0.58}\text{N}$  and with the AlGaN:Si+ contact layer mentioned above, this gives a wavelength separation of  $\sim 17$  nm between the  $\lambda_{1/2}$  of transmittance drop-off of the two layers.

This is illustrated in the optical transmittance spectra of the calibration samples as well as the fully grown device structure in Figure 4.6. The thickness of the *i*-type absorption layer should also be such that most of the photons are absorbed in the layer while the layer thickness is not so large that it relaxes due to the lattice mismatch with the  $\text{Al}_{0.52}\text{Ga}_{0.48}\text{N}$  layer.

In Figure 4.6, it is also noted that the transmittance spectra of the full device structure closely resembles that of the  $\text{Al}_{0.42}\text{Ga}_{0.58}\text{N}$  calibration sample on the short-wavelength side. This is because in the device structure, the  $\text{Al}_{0.42}\text{Ga}_{0.58}\text{N}$  layer has the lowest bandgap energy of the layers of significant thickness. In the long wavelength side, the sinusoidal part is seen to have more oscillations for the full device structure because the AlGaIn layer thickness in the calibration samples is much smaller.

In this figure, it can also be seen that for the full device structure, a small tail remains between the wavelengths of  $\sim 285$  nm and  $\sim 265$  nm. This feature is indicative of the fact that all of the incident photons are not absorbed in the absorption region. This loss can be remedied by using a thicker absorption region. However, it was experimentally determined with XRD RSM data that if the absorption region is thicker than  $\sim 200$  nm, the layer relaxes by the introduction of defects. As a result, the thickness was kept to  $\sim 150$  nm to stay within a safe limit. The XRD RSM data for the as-grown device is shown in Figure 4.7. It is seen that with the given device structure, the absorption region is almost fully strained to the TDD reducing template layer underneath.

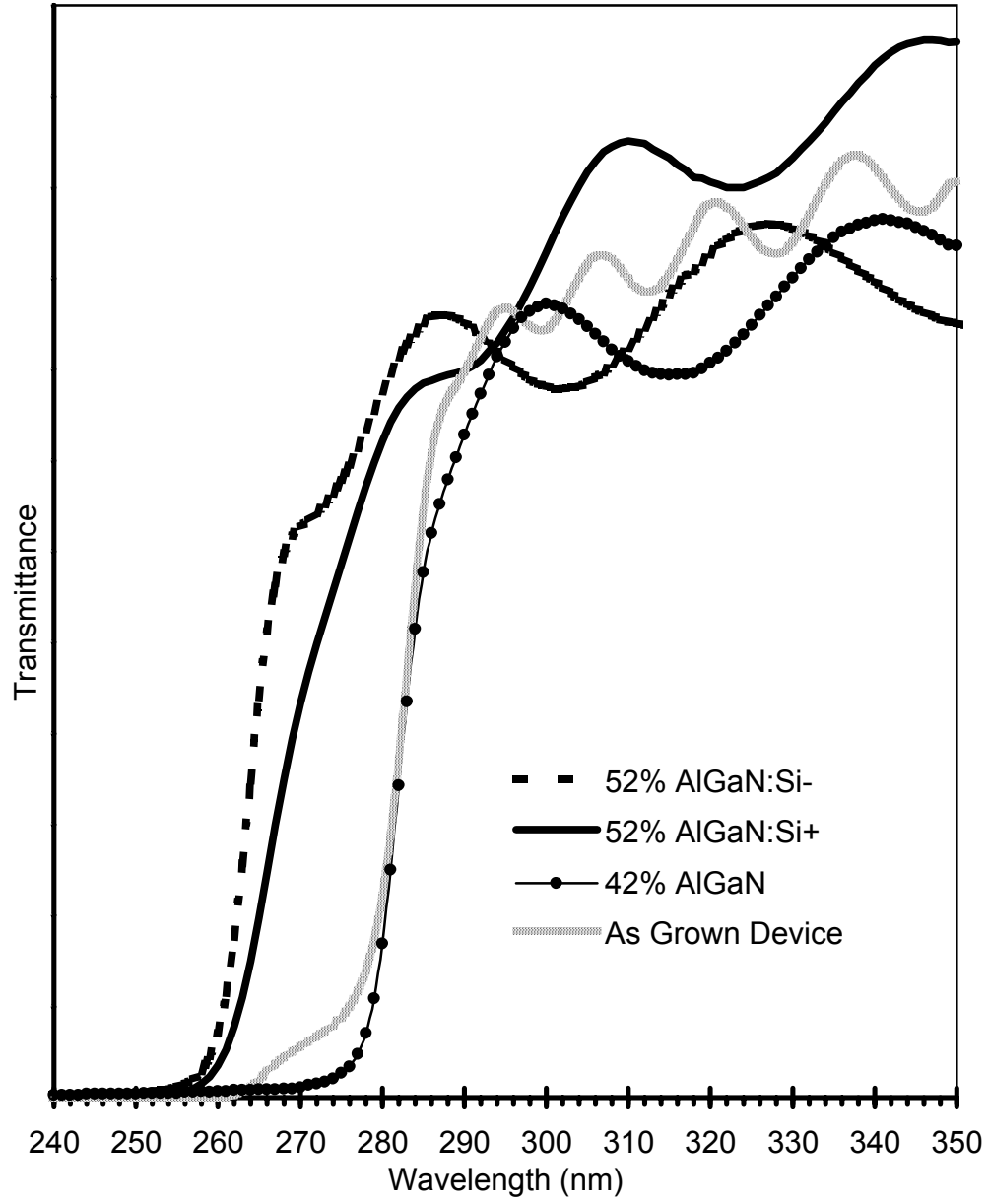


Figure 4.6: Optical transmittance measurements on various layers related to an SBD. The vertical scale is arbitrary.

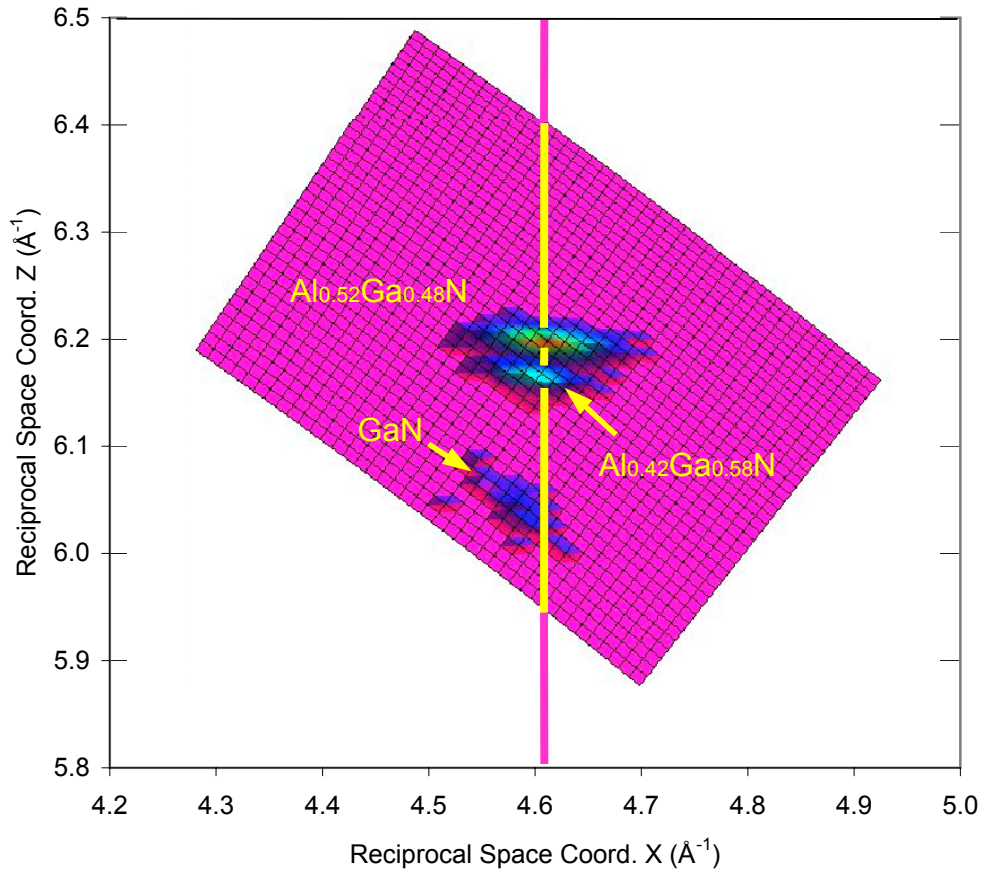


Figure 4.7: XRD RSM around the (205) reciprocal space point for an as-grown SBD device sample. The X and Y axis units are distances in reciprocal space in inverse Å unit (sample M2510).

#### 4.2.6 Superlattice Doping for *p*-type AlGaN

It has been noted before that the use of an SLS in the growth of Mg-doped AlGaN material has the prospect to deliver a high acceptor activation and high free hole concentration. This would be useful for an LED device because, on the one hand, it would increase hole injection into the active region for optical recombination and on the other hand, it would reduce the resistivity of the *p*-layers contributing to lower ohmic heating.

In order to determine whether this theoretical improvement can be practically realized, two test structures were grown. The goal is to compare the difference in vertical resistance of a mesa structure made out of thick AlGaN:Mg and an AlGaN:Mg SLS of comparable Al-content and approximately the same thickness. It is usually found that making ohmic contact to AlGaN:Mg is difficult, and the absence of ohmic contact can significantly hinder interpretation of obtained data. As a result, the thick AlGaN:Mg and the AlGaN:Mg superlattices were sandwiched between a thick GaN:Mg layer at the bottom and a thin GaN:Mg layer on the top. The bulk layer was made of 225 nm thick  $\text{Al}_{0.14}\text{Ga}_{0.86}\text{N} : \text{Mg}$ . The superlattice consisted of 75 repetitions of the two layers of 1.5 nm  $\text{Al}_{0.14}\text{Ga}_{0.86}\text{N} : \text{Mg}$  and 1.5 nm  $\text{Al}_{0.18}\text{Ga}_{0.88}\text{N} : \text{Mg}$ .

The two structures were then etched down to the bottom GaN:Mg layer with a mesa diameter of 75  $\mu\text{m}$  with the RIE technique. Ohmic metallizations were then deposited on the top and bottom contact layers. Specific contact resistance measurement at the bottom of the mesa area in adjacent

positions confirmed that the contribution of contact resistance of metallization and spreading resistance in the bottom GaN:Mg layer is small compared to the contribution of the AlGaIn:Mg structure. The I-V relationship between the two contacts were then measured with standard semiconductor parameter analyzer hardware.

The I-V characteristics are shown in Figure 4.8. It is noted that the I-V relation obtained was not completely linear for either, making extraction of the resistance complicated. However, the general nature of the significant reduction in resistance by the use of the SLS-es is clearly evident.

While the results of this experiment establishes the potential of SLS for improvement of acceptor activation in the AlGaIn material system, whether or not this can be extended to high Al-containing alloys and whether or not the improvement is significant in that part of the alloy system remains to be determined. The experiment cannot be readily extended to the use of high Al-content AlGaIn because the structures to be compared essentially needs to be sandwiched between GaN:Mg layers. This is because, on the one hand, the use of AlGaIn would make fabrication of ohmic contact to the contact layer difficult, which would make it difficult to extract meaningful results from the experiment; on the other hand, since an AlGaIn:Mg layer would have a higher resistance, the contribution of the spreading resistance of the bottom contact layer would not be negligible as it is in the case of GaN:Mg. The use of GaIn, on the other hand, obviates the growth of a reasonable thickness of  $\text{Al}_x\text{Ga}_{1-x}\text{N}$  with  $x \sim 0.4$ . Because of lattice mismatch and tensile stress, the AlGaIn layer

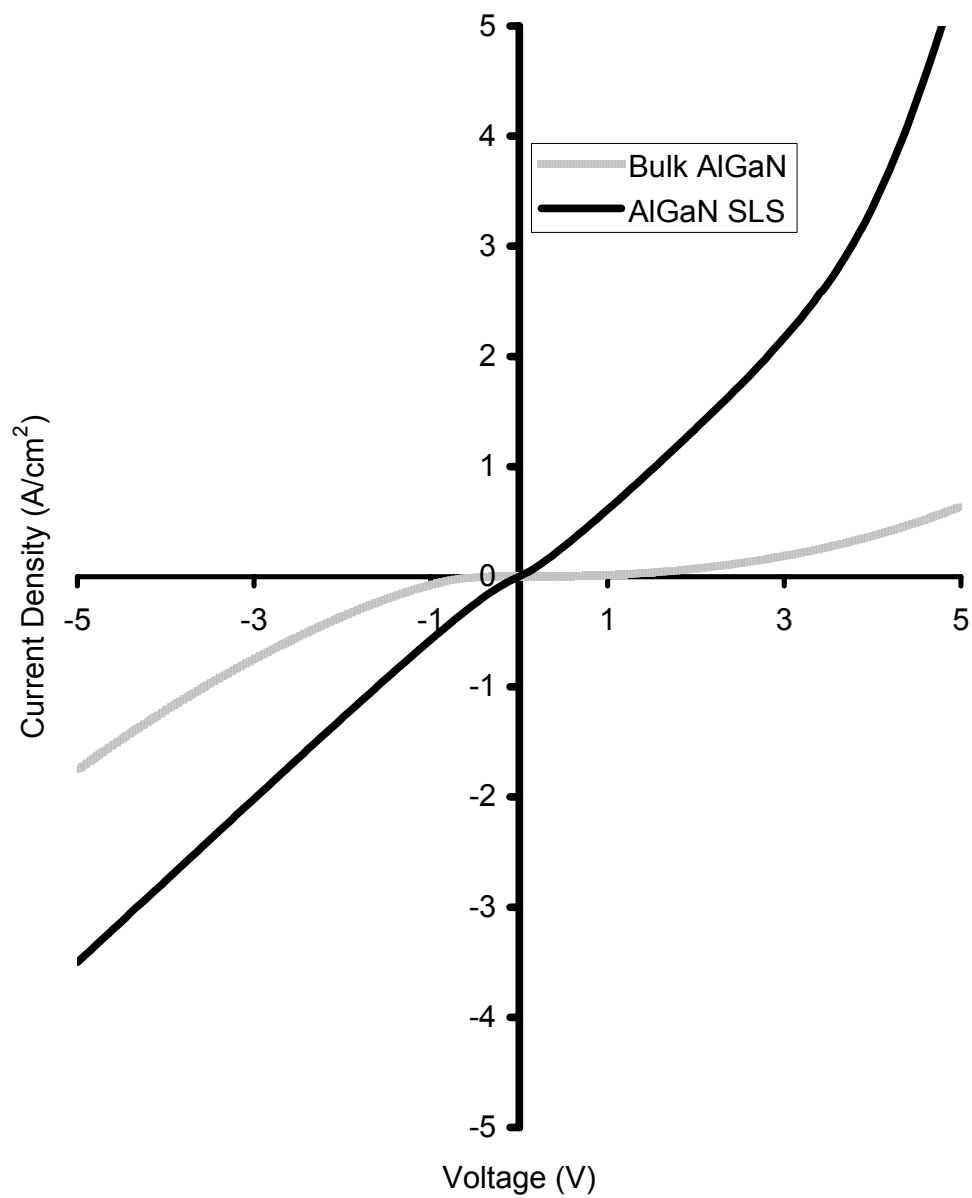


Figure 4.8: I-V characteristics for comparison of vertical resistivity reduction in *p*-type AlGaIn SLS.

would relax by the introduction of numerous dislocations.

While it has not been possible to directly verify the improvement in vertical conduction in AlGaIn:Mg SLS-es with higher Al-content, it is to be expected that the results of the lower Al composition regime would also hold for higher Al-content from a simple theoretical point of view.

### 4.3 Solar-Blind Photodetectors

Using the material development mentioned earlier, high performance SBDs were fabricated. These devices showed a high EQE  $\eta_{ext}$ , low dark current, high differential forward resistance, and a high detectivity,  $D^*$ .

The as-grown crystal was processed into mesa-geometry photodiodes by Collins et al. [110], [111] following standard processing techniques. First, 250  $\mu\text{m}$  and 400  $\mu\text{m}$  diameter diode mesas were defined by etching the AlGaIn layers through window openings patterned in a 200 nm thick  $\text{SiO}_2$  mask with reactive-ion etching (RIE). Then the etch mask was removed and the Mg acceptor atoms were activated again by rapid thermal annealing at 850°C for 10 min. Through openings defined in the  $\text{SiO}_2$  passivation layer, Ti/Al/Ti/Au  $n$ -contact metal was evaporated, which was followed by an  $n$ -contact anneal at 850°C for 30 sec. Then Ni/Au  $p$ -metallization was evaporated and annealed at 675°C for 2 min. The current-voltage (I-V) characteristics of the device in absence of illumination and under UV illumination were obtained using an HP4156C semiconductor parameter analyzer system. As shown in

Figure 4.9, the devices had a low forward resistance, very low dark current up to  $-5$  V reverse bias, and a strong UV photoresponse. For the measurement of EQE, light from a broad-spectrum xenon lamp was passed through a SPEX 0.25 m-monochromator and was focused onto the substrate-side of the sample through a UV-grade optical fiber and other optical components. Device contacts were made with mechanical probes. An SRS Model 870 lock-in amplifier synchronized with a mechanical chopper operating at a frequency of 200 Hz was used to measure the photocurrent. This photocurrent was then converted to EQE by standardizing with the photocurrent data obtained from a calibrated silicon photodetector with known responsivity in the wavelength range of interest. Low-current measurements were performed to determine the zero-volt device resistance  $R_0$ . Specific detectivity,  $D^*$ , was determined from the measured responsivity and  $R_0$ .

The EQE spectra obtained are shown in Figure 4.10. Under zero-volt bias, an EQE of 58% at  $\lambda = 274$  nm (responsivity  $\sim 0.13$  A/W) was obtained without the use of an anti-reflection coating. The EQE was seen to depend on bias voltage, having a value of 64% at  $-5$  V reverse bias. The zero volt responsivity showed a sharp cut-off by one order of magnitude for a change in wavelength by  $\sim 4$  nm in both the longer and shorter wavelength side. This is the highest EQE reported from a semiconductor-based SBD to date.

For SBD operation, it is generally assumed that thermal noise dominates over other forms of noise. As a result, the detectivity  $D^*$  can be calculated by using the noise equivalent power obtained from the zero-volt resistance

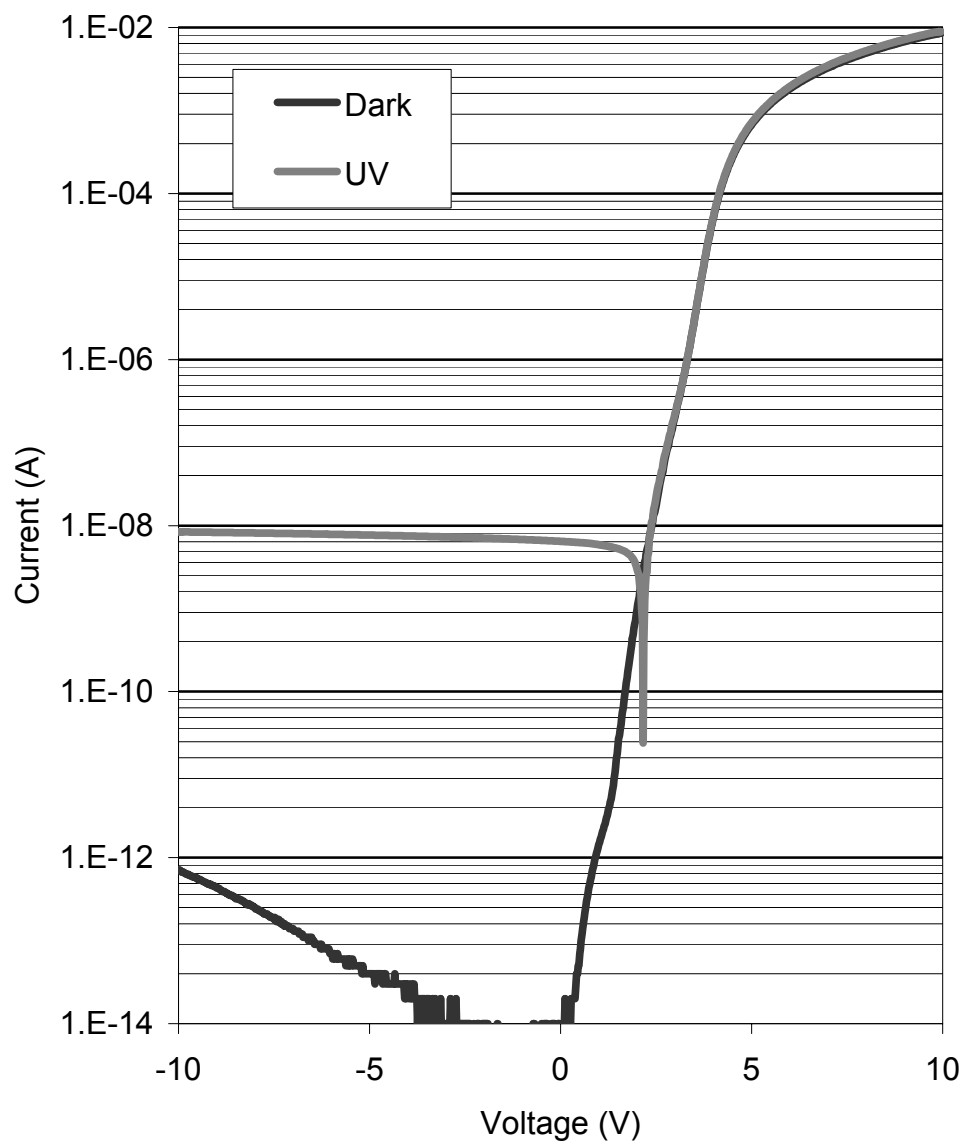


Figure 4.9: Voltage-current characteristics of a fabricated SBD device under dark and UV-illuminated conditions.

$R_0$  measured by a high-precision low current measurement device. The fabricated SBD devices showed a high  $R_0 = 2.51 \times 10^{14} \Omega$ . Using the device diameter of  $250 \mu\text{m}$ , the value of  $R_0 A$  was  $1.23 \times 10^{11} \Omega - \text{cm}^2$  where  $A$  is the device area. Using the appropriate formula, the value of detectivity obtained was  $D^* = 3.22 \times 10^{14} \text{ cm} - \text{Hz}^{1/2}/\text{W}$  at peak wavelength.

Since one of the goals for development of SBDs is fabrication of flip-chip bonded photodetector arrays, it is important to have a good uniformity among adjacent devices and a high yield. Characterization of discrete devices processed showed that indeed adjacent devices processed had a good yield and uniformity. Encouraged by this fact, arrays of photodetectors were fabricated by collaborators at BAE Systems. Several  $256 \times 256$  photodetector arrays were successfully fabricated. Statistical analysis of distribution of responsivity of individual elements of the array had a ratio of standard deviation to mean of  $\sigma/\mu = 6\%$ . A response operability of 99.8% was obtained for these fabricated arrays [112]. A map of responsivity over one such detector array under solar-blind operation is shown in Figure 4.11.

The device parameters are summarized in Table 4.2.

## 4.4 Development of UV LEDs

A number of GaN/AlGaIn-based LED emitting in the UV were developed in the present work. The device structure, performance characteristics and other relevant information are presented in this section. The first struc-

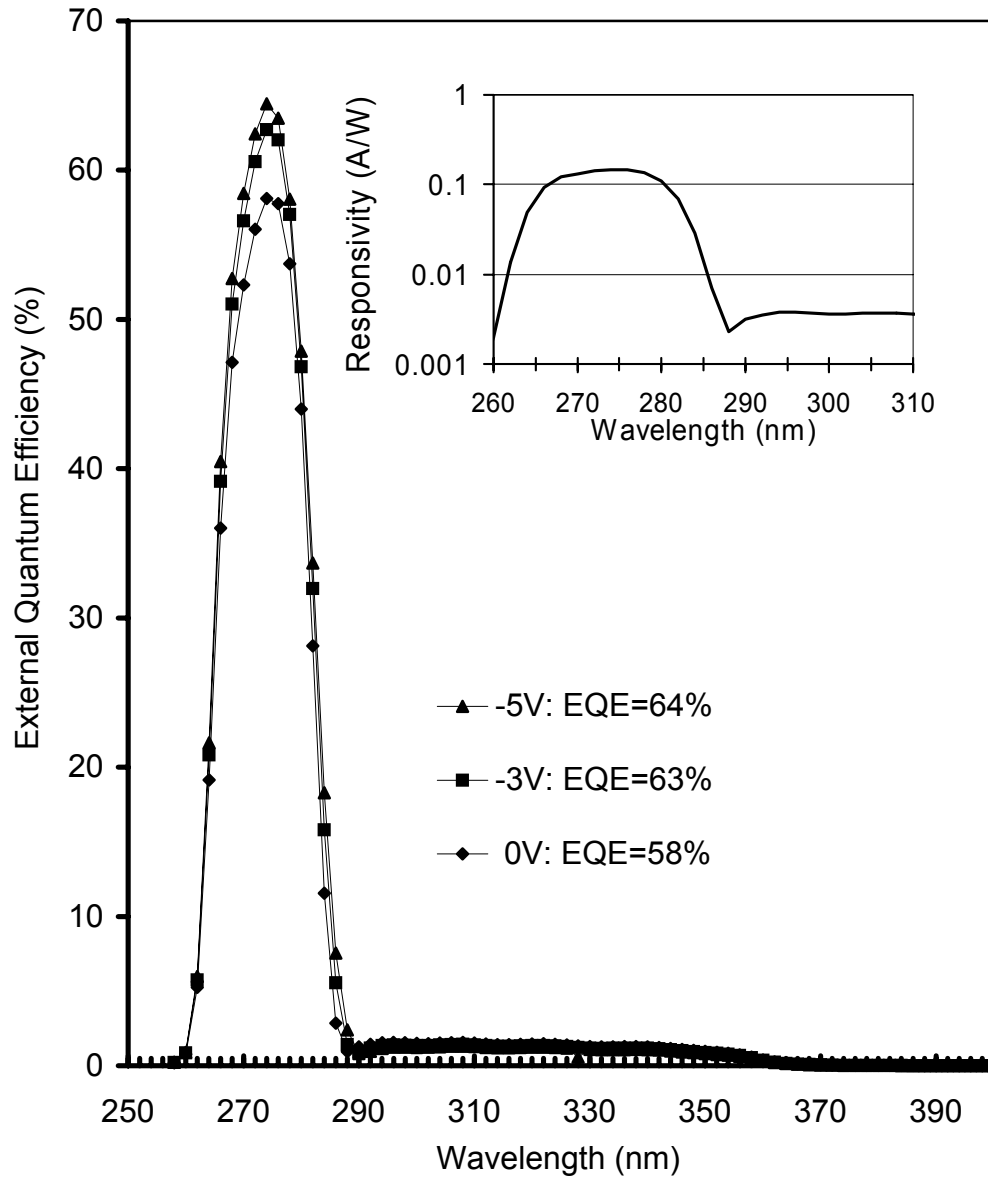


Figure 4.10: EQE spectra of fabricated SBD devices at different bias voltages. Inset shows corresponding responsivity spectra at zero volt bias. (Measurement by P. Lamarre, M. Reine, and K. Wong; BAE Systems).

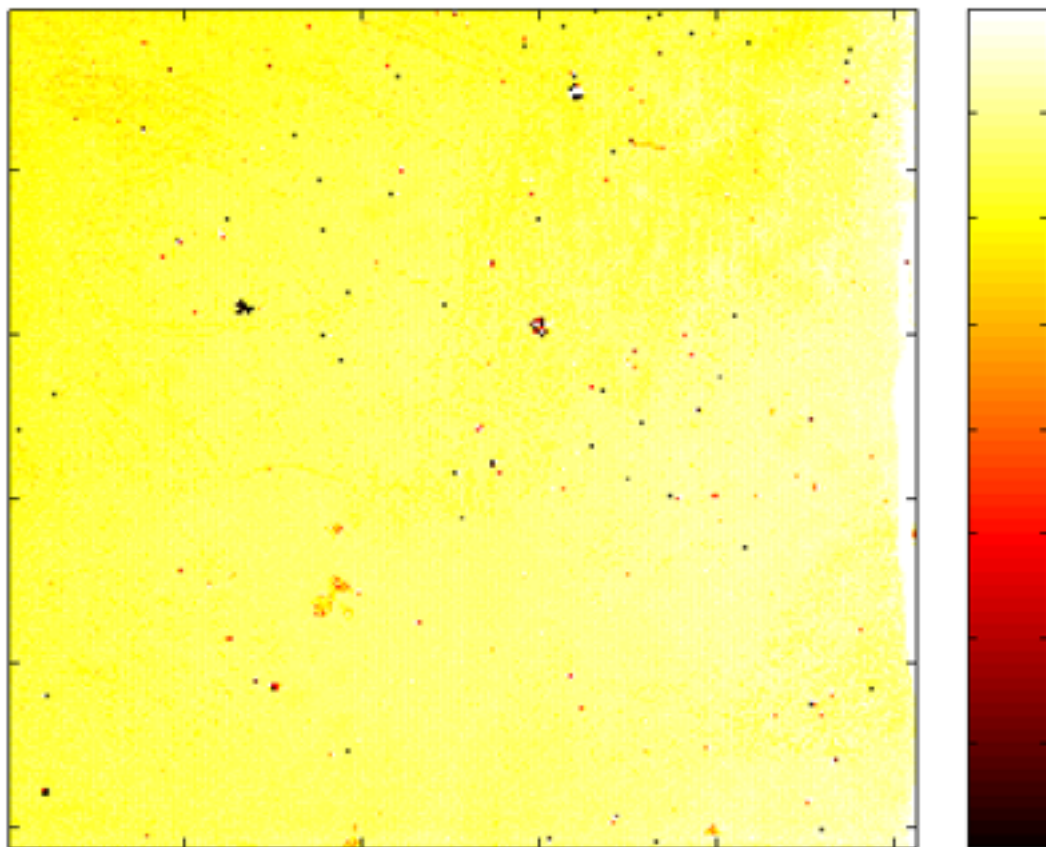


Figure 4.11: Responsivity plot for a  $256 \times 256$  SBD array. The color bar on the right hand side indicates responsivity in an arbitrary linear scale. (Measurement by A. Hairston, and C. Cooke; BAE Systems).

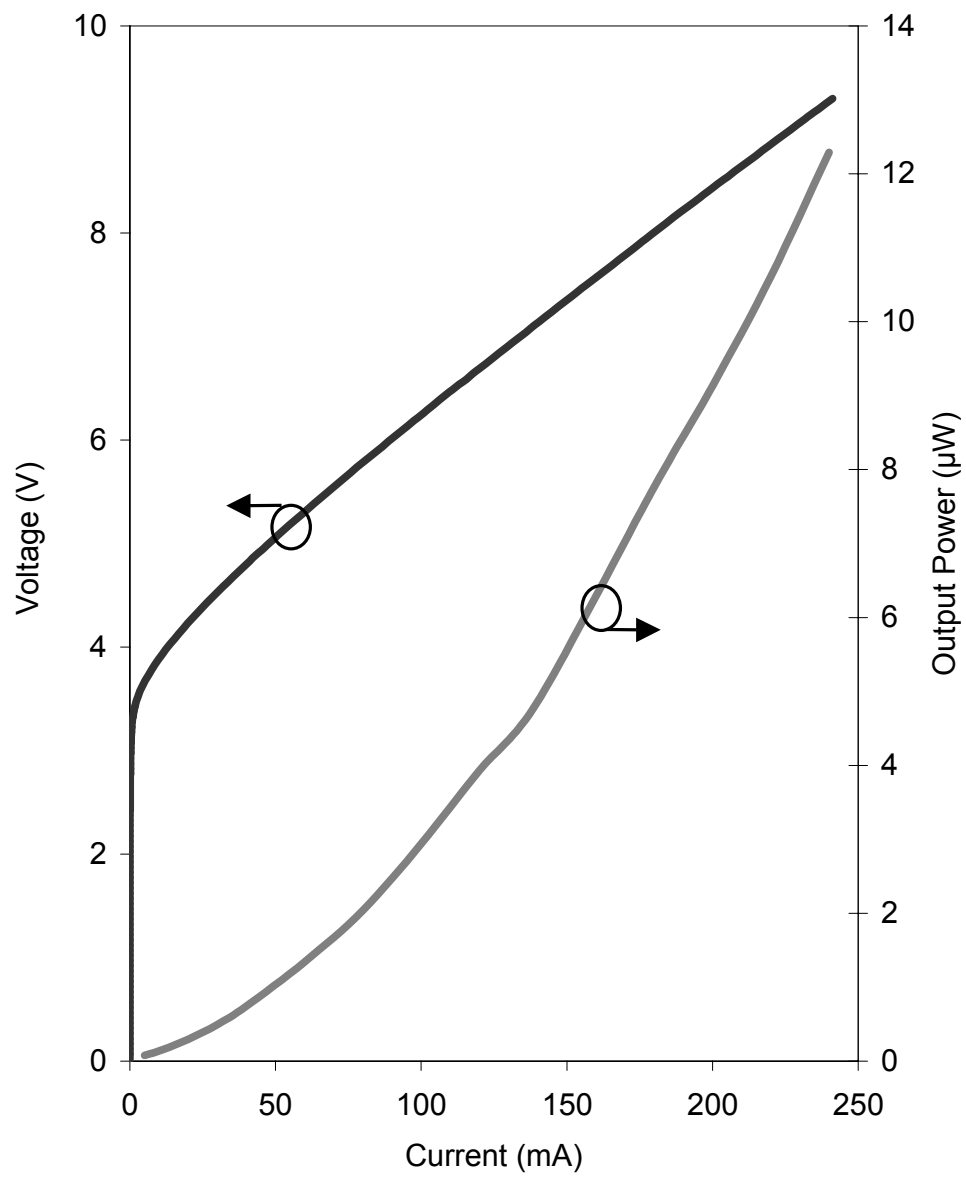


Figure 4.12: Plot of bias voltage and output power vs. device current for GaN SQW LED.

<b>Peak EQE at 0 V bias</b>	58%
<b>Wavelength of peak EQE</b>	274 nm
<b>FWHM of EQE peak</b>	20 nm
<b>Peak responsivity</b>	0.13 A/W
<b>Detectivity <math>D^*</math></b>	$3.22 \times 10^{14} \text{ cm} - \text{Hz}^{1/2}/\text{W}$
<b>Turn-on voltage</b>	5.2 V
<b>Open circuit voltage</b>	2.16 V
<b>Differential forward resistance (250 <math>\mu\text{m}</math> dia device)</b>	360 $\Omega$
<b>Operability (for <math>256 \times 256</math> array)</b>	99.8%

Table 4.2: Performance characteristics of SBD.

ture to be described is a GaN SQW structure grown on 6H SiC substrates by use of an AlN HTBL. A bulk  $n$ -type layer was used for the bottom contact layer while on the  $p$ -side, a Mg-doped SLS structure was used for reduction of resistivity and improvement of hole injection. The first few periods of the SLS were kept undoped in order to prevent diffusion of Mg into the active region of the device. The active region consisted of a 10 nm thick GaN layer. The complete device structure is shown below:

- $\sim 15$  nm GaN : Mg  $p$ -contact layer
- 20 repetitions of  $\sim 2$  nm  $\text{Al}_{0.10}\text{Ga}_{0.90}\text{N}$  : Mg and  $\sim 2$  nm  $\text{Al}_{0.25}\text{Ga}_{0.75}\text{N}$  : Mg  $p$ -SLS
- 5 repetitions of  $\sim 2$  nm  $\text{Al}_{0.10}\text{Ga}_{0.90}\text{N}$  : ud and  $\sim 2$  nm  $\text{Al}_{0.25}\text{Ga}_{0.75}\text{N}$  : ud Mg diffusion stop layer
- $\sim 50$  nm  $\text{Al}_{0.30}\text{Ga}_{0.70}\text{N}$  : ud
- $\sim 10$  nm GaN : Si— offset SQW

- $\sim 20$  nm  $\text{Al}_{0.10}\text{Ga}_{0.90}\text{N} : \text{Si}-$
- $\sim 50$  nm  $\text{Al}_{0.30}\text{Ga}_{0.70}\text{N} : \text{Si}+$
- $\sim 100$  nm  $\text{Al}_{0.25}\text{Ga}_{0.75}\text{N} : \text{Si}+$
- $\sim 1$   $\mu\text{m}$   $\text{GaN} : \text{Si}+$   $n$ -contact layer
- 100 nm  $\text{AlN}$  high temperature buffer layer
- 6H  $\text{SiC}$  substrate

A standard device processing technique was employed to fabricate  $70$   $\mu\text{m}$ -diameter mesa structure diodes from the grown epitaxial layers. The details on device processing and measurement along with a comparison with a similar MQW LED structure have been previously reported by Zhu et al. [63].

The variation of current and output power for a typical LED diode is shown in Figure 4.12. The diodes had a forward differential resistance of  $\sim 25$   $\Omega$ . The bias voltage at 20 mA forward current was 4.2 V. An output power of  $5$   $\mu\text{W}$  was obtained at 140 mA forward current. No special light extraction scheme was used to measure this output power; and since the bottom GaN layer and SiC substrate are expected to contribute significantly to light absorption, a much higher output power is expected in a structure with improved light extraction capability. Figure 4.13 shows the EL spectra from the LED structure under various excitation current levels. The structure emitted at a peak wavelength of 363 nm with a FWHM of  $\sim 9$  nm of the emission peak.

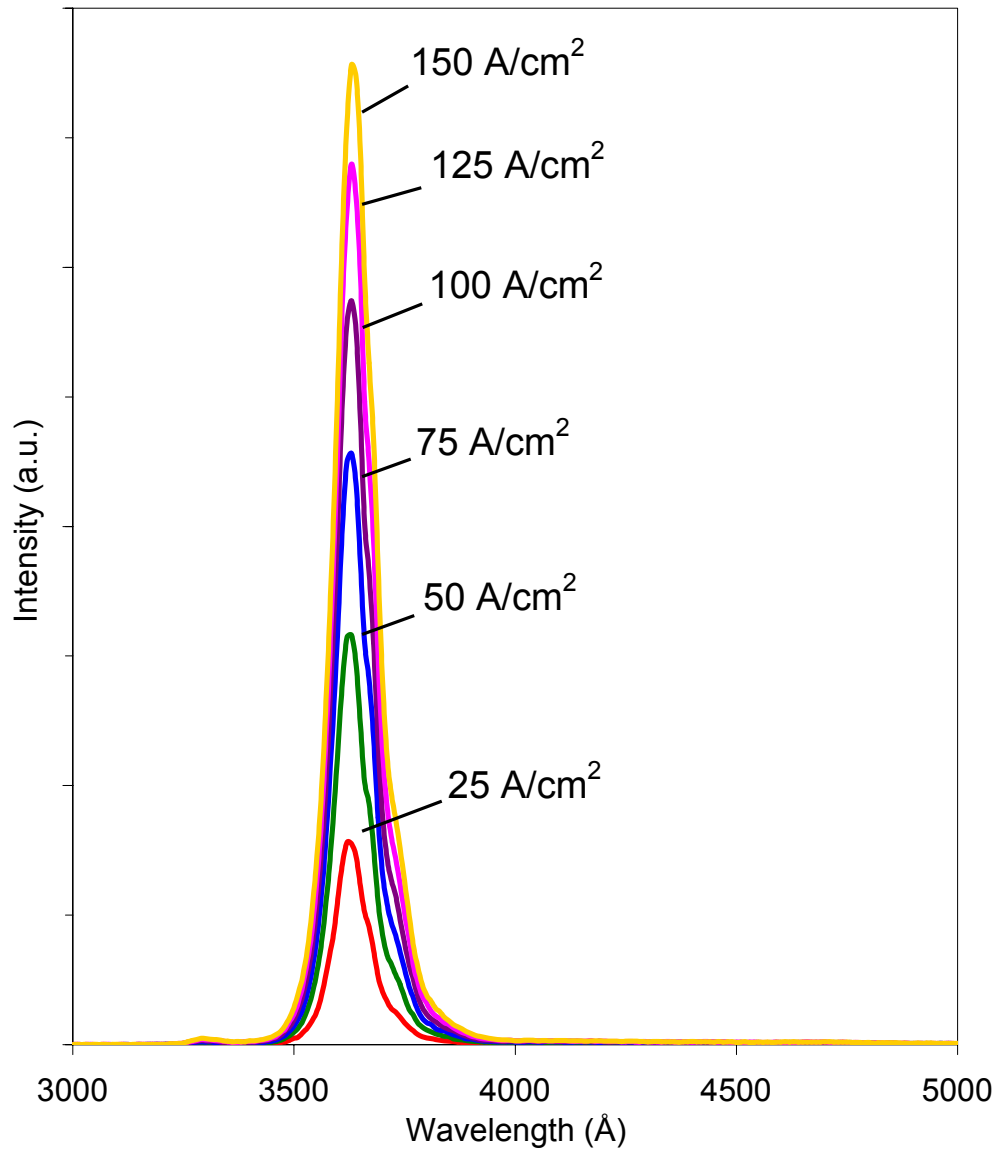


Figure 4.13: EL spectra obtained from the fabricated GaN SQW LED under different injection current densities.

After the demonstration of a near UV LED, research was undertaken to develop LEDs emitting in the  $\sim 280$  nm –  $\sim 300$  nm wavelength range. The challenges involved in this development are:

- Low luminescence efficiency of  $\text{Al}_{0.42}\text{Ga}_{0.58}\text{N}$  required for  $\sim 290$  nm emission,
- Difficulty in obtaining a  $p$ -type AlGa $\text{N}$ , which limits hole injection and increases device series resistance, and
- Difficulty in obtaining low-resistivity  $n$ -contact layer.

Of these, only the third issue could be solved adequately in this current work. The inadequacy of the material quality of AlGa $\text{N}$  was evident from CL measurements performed at room temperature on thick  $\text{Al}_{0.42}\text{Ga}_{0.58}\text{N} : \text{Si}$ -samples. The luminescence had a peak at  $\sim 293$  nm with a FWHM of 15 nm. The CL spectra are shown in Figure 4.14. The intensity in the CL spectra is in arbitrary units in this figure, and under similar excitation conditions, high-quality Si-doped bulk Ga $\text{N}$  has a CL peak five or more orders of magnitude brighter.

Nevertheless, DH-LED layers were grown with an  $\text{Al}_{0.52}\text{Ga}_{0.48}\text{N} : \text{Si}+$  layer for  $n$ -contact layer. A Mg-doped SLS was incorporated on the  $p$ -side. The active region consisted of a  $\sim 100$  nm thick  $\text{Al}_{0.42}\text{Ga}_{0.58}\text{N} : \text{ud}$  layer. The device structure consisted of, from the top,

- $\sim 25$  nm Ga $\text{N} : \text{Mg}$  top  $p$ -contact layer

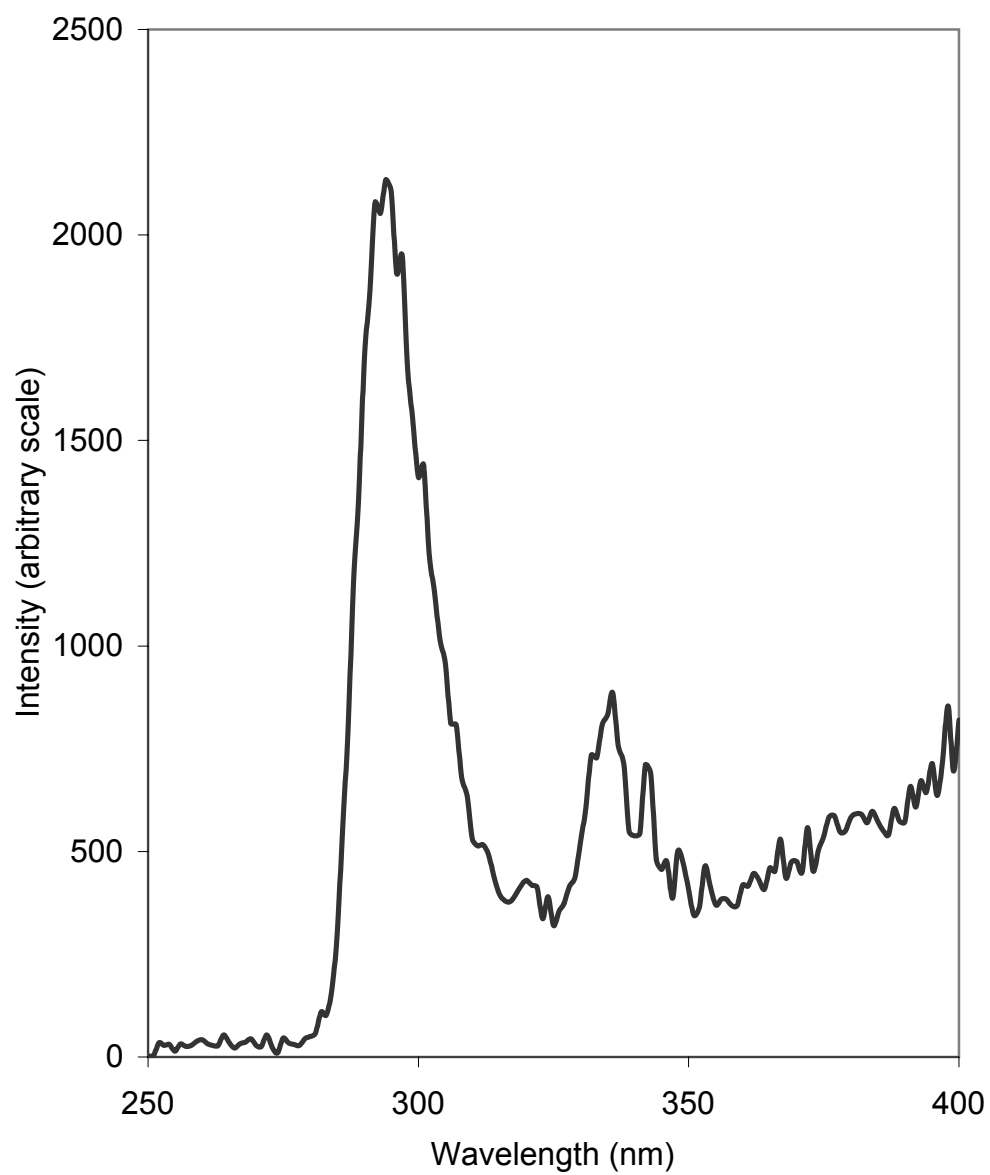


Figure 4.14: Room temperature CL spectra of a thick  $\text{Al}_{0.42}\text{Ga}_{0.58}\text{N} : \text{Si}$  sample (sample M2983).

- 10 repetitions of  $\sim 2.5$  nm  $\text{Al}_{0.60}\text{Ga}_{0.40}\text{N} : \text{Mg}$  and  $\sim 2.5$  nm  $\text{Al}_{0.45}\text{Ga}_{0.55}\text{N} : \text{Mg}$   $p$ -SLS
- $\sim 100$  nm  $\text{Al}_{0.42}\text{Ga}_{0.58}\text{N} : \text{ud}$  active region
- $\sim 200$  nm  $\text{Al}_{0.52}\text{Ga}_{0.48}\text{N} : \text{Si}+$   $n$ -contact layer
- $\sim 600$  nm  $\text{Al}_{0.52}\text{Ga}_{0.48}\text{N} : \text{Si}-$  template layer for reduction of TDD
- $\text{AlN}$  LTBL
- Both-side polished  $c$ -plane sapphire substrate

LED devices were fabricated from the epitaxial layers with a standard processing technology and electrical characterization was performed as before. Again, no special device fabrication procedure was followed for improvement of light-extraction. The devices had an EL peak at  $\lambda = 302$  nm with FWHM of  $\Delta\lambda = 10$  nm. The EL spectra are shown in Figure 4.16. The relative redshift compared with the CL peak is probably due to excessive heating at the high current density used to obtain the luminescence.

The devices had a turn-on voltage of  $\sim 8$  V and a forward differential resistance of  $\sim 300 \Omega$ . A peak output power of 720 nW was measured under 80 mA DC current injection. Pulsed measurement of power to obtain higher current density without deterioration of the device by excessive heating was not performed. Also, no special technique for heat dissipation was used for these measurements. The dependence of the device current and output power with bias voltage is shown in Figure 4.15.

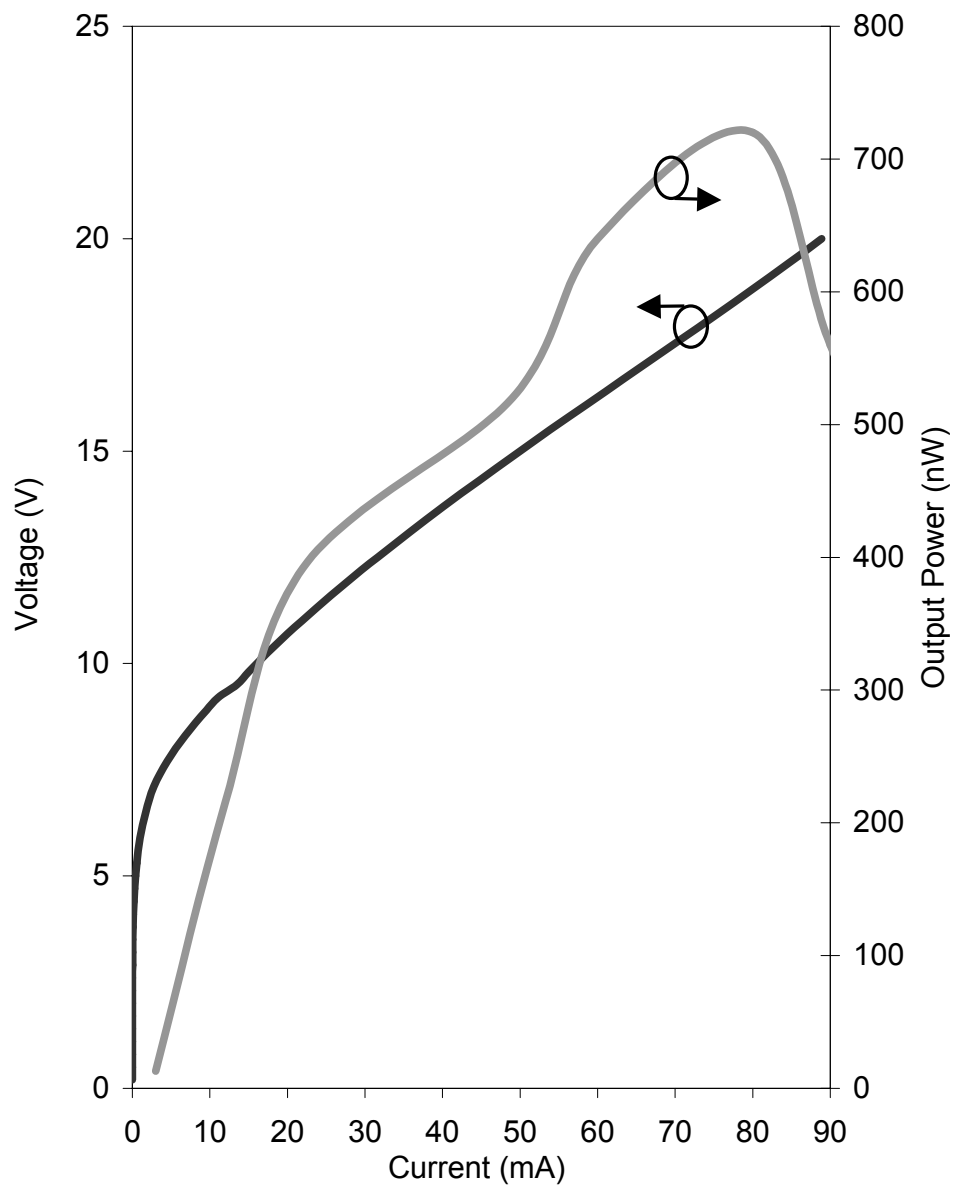


Figure 4.15: Plot of bias voltage and output power vs. device current for AlGaIn DH LED emitting at 302 nm.

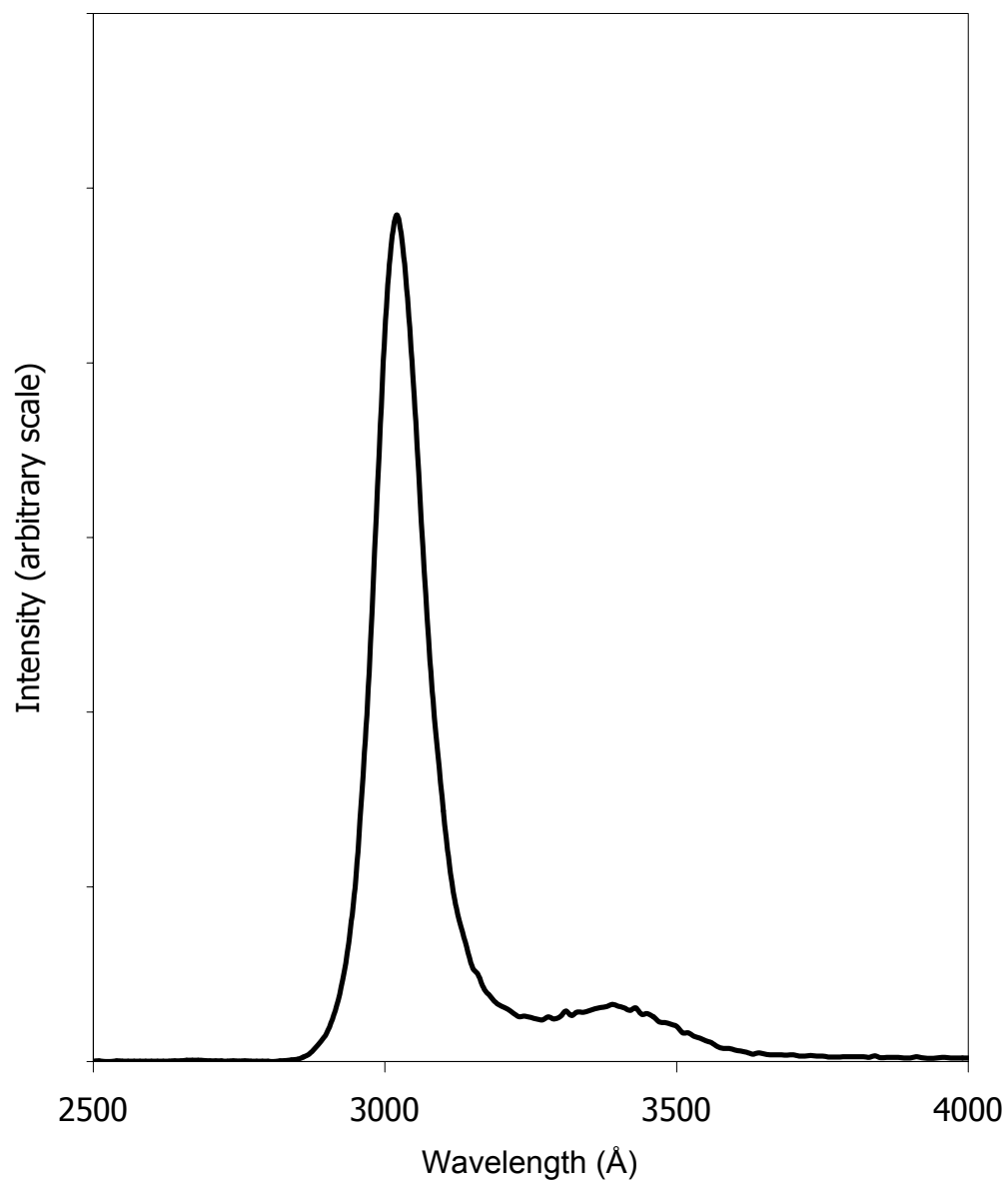


Figure 4.16: EL spectra of AlGaIn DH LED emitting at 302 nm at 80 A/cm<sup>2</sup> excitation current density.

Encouraged by these results, experiments were performed to push the emission wavelength shorter. The Al-content in the active region was increased and, in order to keep resistivity arising from the  $p$ -layers low, the thickness of the AlGaN  $p$ -layer was reduced to  $\sim 10$  nm. For such a small thickness, the SLS was eliminated. The active region thickness was increased to  $\sim 150$  nm.

Devices fabricated from this structure also showed EL at room temperature under DC injection conditions. The EL spectra had a peak wavelength of 290 nm with a FWHM of  $\sim 8$  nm. Figure 4.17 shows the EL spectra obtained from the sample. It is seen in this plot that a broad longer wavelength peak is also obtained. This luminescence is presumably from the extension of the diffusion region for electron injection into the  $p$ -type GaN layer which gave recombination in the GaN.

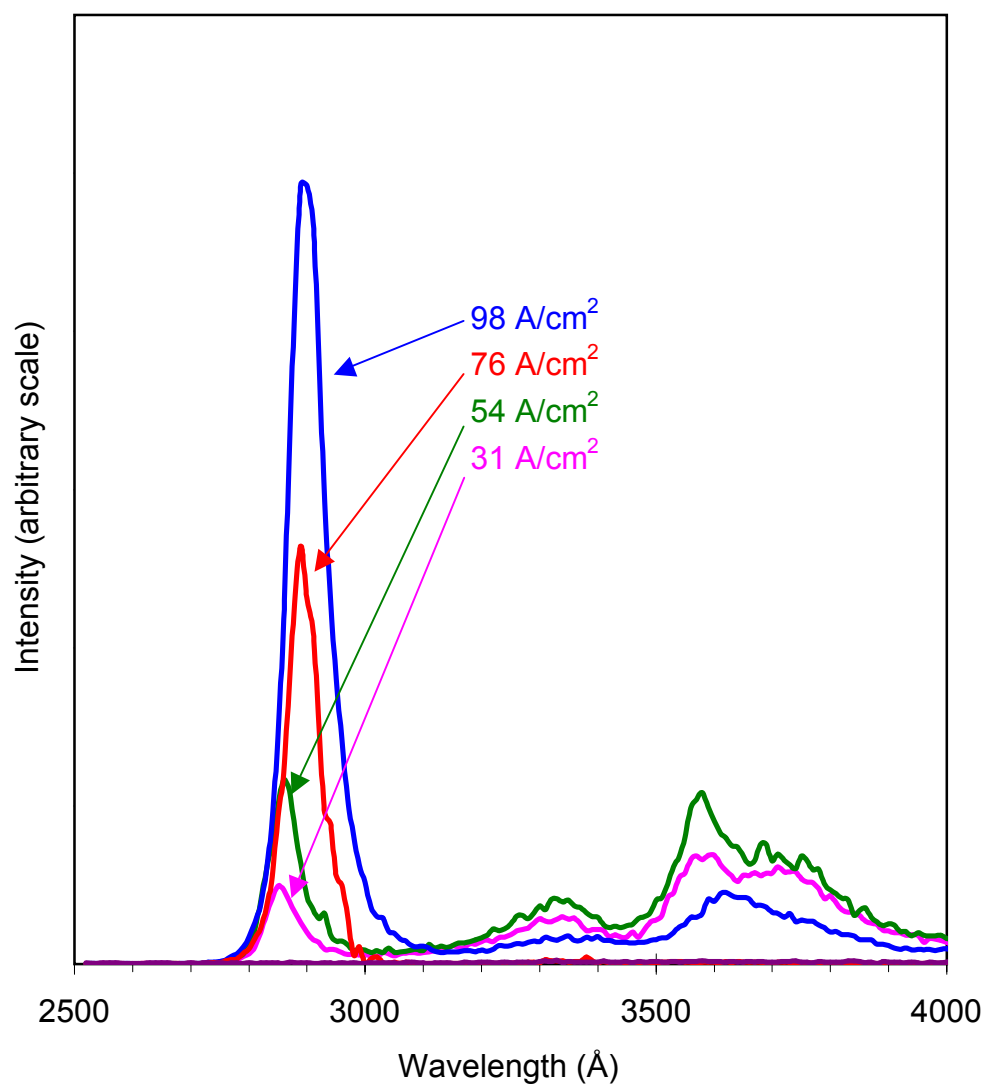


Figure 4.17: EL spectra at different injection current densities for AlGaIn DH LED emitting at 290 nm.

## Chapter 5

# Recommendation for Future Research and Summary

### 5.1 Photodetectors

The development of very high performance SBDs have been described in this work. The high EQE of 58% obtained is indicative of a high internal quantum efficiency also. This result suggests that while there may still be room for improvement of performance by improvement of material quality and optimization of device structures, there is not much space for a major breakthrough. It has been difficult to obtain AlGaIn:Si+ with an even shorter cut-off wavelength, which would have increased the FWHM of the device to give the SBD a broader spectral sensitivity on the shorter wavelength side. More effort can be devoted to this problem since the broader responsivity

profile would be useful for a number of applications.

In the responsivity spectra of the fabricated SBD devices, sometimes a small responsivity is seen in the 290 nm to 350 nm wavelength range. While some devices have shown this behavior, other devices fabricated from the same epitaxial layer have not. It can be suggested that this long wavelength response arises from alteration of side-walls during reactive-ion etching. However, the reason for this long-wavelength response has not been clarified. More research is needed in order to determine the reason behind this response and also to eliminate this effect.

The SBD device design can then be extended to other related structures including resonant-cavity detectors and avalanche detectors. So far, efforts to develop avalanche photodetectors with AlGaIn have failed due to excessive leakage currents. With the recent commercial availability of both native “bulk” GaN and AlN substrates, it may be possible to expend new research efforts in the development of avalanche diodes since the lower dislocation density afforded by the bulk substrates has the potential of reducing the reverse leakage significantly. However, material is not the only issue in reducing the leakage current — the quality of the side-wall etch potentially plays a very significant role in this. Improvement of device processing technology as well as development of side-wall passivation materials and processes are required for this development.

Photodetectors other than avalanche diodes that are capable of providing gain are also of high interest. One such device is the phototransistor,

which is generally a specially designed heterojunction bipolar transistor (HBT) without any base contact. The equivalent of base current is created by the photogenerated carriers, and intrinsic gain from the transistor action is obtained. Doping issues and also leakage has so far hindered the growth of both HBT and phototransistor technology to date. However, it can be safely said that more development in both fields is expected from the nitride research community.

## 5.2 Light Emitters

The development of nitride-based deep-UV emitter technology is still in its infancy. To date, the major problems faced by the research community are the relatively poor luminescence properties of present AlGaN material and the fundamental problem of the inability to obtain high  $p$ -type doping. Various techniques such as IR illumination of  $p$ -type material and use of SLS for improved acceptor ionization needs to be studied.

Although it is very difficult to obtain high  $p$ -type doping in this material system, it is important to note that due to the typically high acceptor concentration, the depletion width on the  $p$ -side is expected to be quite narrow. Since high  $n$ -type doping has already been obtained, the depletion width should be narrow enough on the  $n$ -side. A tunnel-junction device has already been demonstrated with this feature [85]. Tunnel-junction contact to the  $p$ -side of the device will allow the use of a thin  $p$ -layer with a thick  $n$ -layer, which

will keep the active region far enough from the surface and metalization while providing the ability to inject holes. Also, if the  $p$ -layer can be made thin enough, AlGaIn with lower Al-content may be used without relaxation which will have higher acceptor ionization. If the  $p$ -layer in this scheme is kept thin enough, it will not contribute significantly to absorption of generated photons. However, appropriate structural modifications need to be made so that significant optical recombination does not take place in this layer instead of the device active region, effectively reducing the energy of luminescence.

Material quality improvement is of paramount importance in order to improve the luminescent properties of the material. Native substrates for homoepitaxy can definitely play a significant role in this quality improvement. Improvement of the growth technique, particularly in control of the nucleation of initial material, can play a role also. Since a high concentration of Al is present in the alloy and since oxygen is known to be detrimental to both electrical and optical properties, strict control of oxygen incorporation and precursor purity is required. The effect of intentional impurities in improving the luminescence properties also has the potential to revolutionize the technology.

### 5.3 Summary

To summarize, the group-III nitrides are direct-bandgap semiconductors with bandgap equivalent wavelengths spanning the spectral range of red

to deep UV. The material is chemically and thermally stable. While other semiconductor material systems are, at present, more suitable for fabrication of optoelectronic devices in the red to yellow region of the spectrum, the nitrides have established their position at the shorter wavelength side of the current device technology.

MOCVD is the dominant technology for growth of epitaxial III-nitrides, and the technique has been demonstrated to be capable of growing high-quality nitride layers, including GaN, InGaN, AlGaN, and InAlGaN.

Large-area single-crystal substrates of the III-nitrides are difficult to produce, and to-date heteroepitaxy on sapphire or SiC substrates is the dominant method of growth of III-nitrides. Despite the large lattice mismatch with these substrates, growth of high-quality nitride films have been demonstrated. Material quality however, is yet not nearly at the level of other conventional semiconductors. Despite the imperfection of material, the III-nitrides are under intense research in areas of device fabrication, growth and analysis of material properties. Researchers have demonstrated the fabrication of a wide variety of electronic devices with the nitrides. Blue and UV laser operation has been obtained; solar-blind and avalanche photodetectors have been demonstrated. Inadequacy of material quality and low doping efficiency at high Al compositions hinder the extension of these works to an even shorter wavelength region.

For the present dissertation, research in growth of high-quality binary nitrides and their alloys was performed. Improvement of the doping efficiency

in superlattices has been studied. SIMS, XRD, Hall-effect measurement, and optical measurements (e.g. CL, transmittance measurement etc.) are some of the techniques that were used to characterize the grown material and structures.

High Si-doping and low resistivity were obtained from  $\text{Al}_{0.52}\text{Ga}_{0.48}\text{N}$  layers, which enabled the realization of a significant improvement in SBD performance. SBD structures in the form of  $p-i-n$  diodes were grown with MOCVD, and the device performance was found to be record-setting. The same work led to the development of the first solar-blind photodetector array with high performance.

Improvement of vertical conduction in Mg doped AlGaIn SLS compared to a bulk AlGaIn structure was studied by fabrication of test structures and a significant improvement in conductivity was observed. This result is attributed to improved acceptor ionization by energy band modulation. The SLS structure was employed in a GaN-based SQW LED structure. The fabricated LED device had emitted at 363 nm with a narrow FWHM.

Extending this research, a DH LED was grown and fabricated with both-side polished sapphire substrates that emitted at 302 nm and 290 nm, respectively. Despite the use of a very simple DH structure, the devices had a fair performance and a narrow FWHM of emission.

With the development of high performance SBDs, future work on photodetectors using this material system should concentrate on fabrication of avalanche photodiodes. Reduction of leakage current by material quality im-

provement will be a prime requirement for this purpose. Research on fabrication of a phototransistor also merits attention.

For light emitting structures, the most important issue impeding development is probably the material quality. Improvement of material quality by use of native substrates, improvement of epitaxial growth technology and incorporation of intentional dopants for improvement of luminescence properties holds promise. Further development of a low resistivity  $n$ -layer and development of a tunnel-junction contact to the  $p$ -material will also be needed.

# Bibliography

- [1] S. J. Rosner, E. D. Carr, M. J. Ludowise, G. Girolami, and H. I. Erikson, *Appl. Phys. Lett.*, **70**, 420 (1997).
- [2] T. Sugahara, H. Sato, M. Hao, Y. Naoi, S. Kurai, S. Tottori, K. Yamashita, K. Nishino, L. T. Romano, and S. Sakai, *Jpn. J. Appl. Phys.*, **37**, L398 (1998).
- [3] F. Bernardini, V. Fiorentini, and D. Vanderbilt, *Phys. Rev. B*, **56**, R10024 (1997).
- [4] F. Bernardini, and V. Fiorentini, *Phys. Stat. Sol. B*, **216**, 391 (1999).
- [5] “*Solid State Physics*”, J. W. Ashcroft and D. N. Mermin, Holt, Rinehart and Winston, New York, 1976.
- [6] “*Organometallic Vapor-Phase Epitaxy: Theory and Practice*”, G. B. Stringfellow, Academic Press, Inc., San Diego, 1989.

- [7] “*High-Resolution X-Ray Scattering from Thin Films and Multilayers*”, V. Holý, U. Pietsch, and T. Baumbach, Springer-Verlag, Berlin Heidelberg, 1999.
- [8] “*Fundamentals of Transmission Electron Microscopy*”, R. D. Hidenreich, Interscience Publishers, New York, 1964.
- [9] “*Scanning Electron Microscopy and X-Ray Analysis*”, J. I. Goldstein, Plenum Press, New York, 1992, p. 89.
- [10] “*Solid State Electronic Devices*”, Fifth Edition, B. G. Streetman, and S. Banerjee, Prentice Hall, Inc., New Jersey, 2000.
- [11] “*Semiconductor Optoelectronic Devices*”, P. Bhattacharya, Prentice Hall, Inc., New Jersey, 1994.
- [12] H. P. Maruska, and J. J. Tietjen, *Appl. Phys. Lett.*, **15**, 327 (1969).
- [13] S. Yoshida, S. Misawa, and S. Gonda, *Appl. Phys. Lett.*, **42**, 427 (1983).
- [14] H. Amano, N. Sawaki, I. Akasaki, and Y. Toyoda, *Appl. Phys. Lett.*, **48**, 353 (1986).
- [15] S. Nakamura, *Jpn. J. Appl. Phys.*, **30**, L1705 (1991).
- [16] R. Dingle, D. D. Sell, S. E. Stokowski, and M. Ilegems, *Phys. Rev. B*, **4**, 1211 (1971).

- [17] R. Dingle, K.L. Shaklee, R.F. Leheny, and R.B. Zetterstrom, *Appl. Phys. Lett.*, **19**, 5 (1971).
- [18] R. Madar, D. Michel, G. Jacob, and M. Boulou, *J. Cryst. Growth*, **40**, 239, (1977).
- [19] K. Hiramatsu, H. Amano, I. Akasaki, H. Kato, N. Koide, and K. Manabe, *J. Cryst. Growth*, **107**, 509 (1991).
- [20] P. A. Grudowski, A. L. Holmes, C. J. Eiting, and R. D. Dupuis, *Appl. Phys. Lett.*, **69**, 3626 (1996).
- [21] T. Sasaki and T. Matsuoka, *J. Appl. Phys*, **64**, 4531 (1988).
- [22] M. A. Khan, R. A. Skogman, and J. M. Van Hove, *Appl. Phys. Lett.*, **56**, 1257 (1990).
- [23] J. I. Pankove, E. A. Miller, and J. E. Berkeyheiser, *J. Lumin.*, **5**, 84 (1972).
- [24] J. J. Pankove and J. A. Hutchby, *J. Appl. Phys.*, **47**, 5387 (1976).
- [25] P. Bergman, G. Ying, B. Monemar, and P. O. Holtz, *J. Appl. Phys.*, **61**, 4589 (1987).
- [26] O. Lagerstedt and B. Monemar, *J. Appl. Phys.*, **45**, 2266 (1974).
- [27] R. D. Cunningham, R. W. Brander, N. D. Knee, and D. K. Wickenden, *J. Lumin.*, **5**, 21 (1972).

- [28] S. Nakamura, T. Mukai, and M. Senoh, *Jpn. J. Appl. Phys.*, **31**, 2883 (1992).
- [29] E. Ejder and P. O. Fagerström, *J. Phys. Chem. Solids*, **36**, 289 (1975).
- [30] T. Matsumoto, M. Sano, and M. Aoki, *Jpn. J. Appl. Phys.*, **13**, 373 (1974).
- [31] M. Ilegems, and H. C. Montgomery, *J. Phys. Chem. Solids*, **34**, 885 (1973).
- [32] U. V. Desnica, N. B. Urli, and B. Etlinger, *Phys. Rev. B.*, **15**, 4119 (1977).
- [33] H. Amano, I. Akasaki, T. Kozawa, K. Hiramatsu, N. Sawaki, K. Ikeda, and Y. Ishii, *J. Lumin.*, **40**, 121 (1988).
- [34] H. Amano, M. Kito, K. Hiramatsu, and I. Akasaki, *Jpn. J. Appl. Phys.*, **28**, L2112 (1989).
- [35] J. A. Van Vechten, J. D. Zook, R. D. Horning, and B. Goldenberg, *Jpn. J. Appl. Phys.*, **31**, 3662 (1992).
- [36] S. Nakamura, T. Mukai, M. Senoh, and N. Iwasa, *Jpn. J. Appl. Phys.*, **31**, L139 (1992).
- [37] S. Nakamura, N. Iwasa, M. Senoh, and T. Mukai, *Jpn. J. Appl. Phys.*, **31**, 1258 (1992).

- [38] H. Amano, M. Kito, K. Hiramatsu, and I. Akasaki, *Jpn. J. Appl. Phys.*, **28**, L2112 (1989).
- [39] S. Nakamura, T. Mukai, and M. Senoh, *Jpn. J. Appl. Phys.*, **30**, L1998 (1991).
- [40] K. Hiramatsu, S. Itoh, H. Amano, I. Akasaki, N. Kuwano, T. Shiraishi and K. Oki, *J. Cryst. Growth*, **115**, 628 (1991).
- [41] W. Qian, G. S. Rohrer, M. Skowronski, K. Doverspike, L. B. Rowland, and D. K. Gaskill, *Appl. Phys. Lett.*, **67**, 2284 (1995).
- [42] S. D. Lester, F. A. Ponce, M. G. Craford, and D. A. Steigerwald, *Appl. Phys. Lett.*, **66**, 1249 (1995).
- [43] H. Amano, M. Iwaya, T. Kashima, M. Katsuragawa, I. Akasaki, J. Han, S. Hearne, J. Floro, E. Chason, and J. Figiel, *Jpn. J. Appl. Phys.*, **37**, L1540 (1998).
- [44] Y. Kato, S. Kitamura, K. Hiramatsu, and N. Sawaki, *J. of Cryst. Growth*, **144**, 133 (1994).
- [45] J. Park, P. A. Grudowski, C. J. Eiting, and R. D. Dupuis, *Appl. Phys. Lett.*, **73**, 333 (1998).
- [46] Z. Yu, M. A. L. Johnson, J. D. Brown, N. A. El-Masry, J. F. Muth, J. W. Cook, Jr., J. F. Schetzina, K. W. Haberern, H. S. Kong, and J. A. Edmond, *MRS Internet J. Nitride Semicond. Res.*, **4S1**, G4.3 (1999).

- [47] S. Nakamura, M. Senoh, S. Nagahama, N. Iwasa, T. Yamada, T. Matsushita, H. Kiyoku, Y. Sugimoto, T. Kozaki, H. Umemoto, M. Sano, and K. Chocho, *Appl. Phys. Lett.*, **72**, 211 (1998).
- [48] K.J. Linthicum, T. Gehrke, D.B. Thomson, K.M.Tracy, E.P. Carlson, T. P. Smith, T.S. Zheleva, C.A. Zorman, M. Mehregany, and R.F. Davis, *MRS Internet J. Nitride Semicond. Res.*, **4S1**, G4.9 (1999)..
- [49] C. I. H. Ashby, C. C. Mitchell, J. Han, N. A. Missert, P. P. Provencio, D. M. Follstaedt, G. M. Peake, and L. Griego, *Appl. Phys. Lett.*, **77**, 3233 (2000).
- [50] G. A. Slack and T. F. McNelly, *J. Cryst. Growth*, **34**, 263 (1976).
- [51] I. Grzegory and S. Porowski, *Thin Sol. Films*, **367**, 281 (2000).
- [52] M. K. Kelly, R. P. Vaudo, V. M. Phanse, L. Görgens, O. Ambacher, and M. Stutzmann, *Jpn. J. Appl. Phys.*, **38**, L217 (1999).
- [53] M. D. Bremser, W. G. Perry, T. Zheleva, N. V. Edwards, O. H. Nam, N. Parikh, D. E. Aspnes, and R. F. Davis, *MRS Internet J. Nitride Semicond. Res.*, **1**, 8 (1996).
- [54] C. Stampfl and C. G. Van de Walle, *Appl. Phys. Lett.*, **72**, 459 (1998).
- [55] V. Adivarahan, G. Simin, G. Tamulaitis, R. Srinivasan, J. Yang, and A. Khan, *Appl. Phys. Lett.*, **79**, 1903 (2001)

- [56] T. Tanaka, A. Watanabe, H. Amano, Y. Kobayashi, I. Akasaki, S. Yamazaki, and M. Koike, *Appl. Phys. Lett.*, **65**, 593 (1994).
- [57] K. S. Kim, M. S. Han, G. M. Yang, C. J. Youn, H. J. Lee, H. K. Cho, and J. Y. Lee, *Appl. Phys. Lett.*, **77**, 1123 (2000).
- [58] R. Y. Korotkov, J. M. Gregie, and B. W. Wessels, *Appl. Phys. Lett.*, **78**, 222 (2001).
- [59] G. Kipshidze, V. Kuryatov, B. Borisov, Y. Kudryavtsev, R. Asomoza, S. Nikishin, and H. Temkin, *Appl. Phys. Lett.*, **80**, 2910 (2002).
- [60] E. F. Schubert, W. Grieshaber, and I. D. Goepfert, *Appl. Phys. Lett.*, **69**, 3737 (1996).
- [61] P. Kozodoy, M. Hansen, S. P. DenBaars, and U. K. Mishra, *Appl. Phys. Lett.*, **74**, 3681 (1999).
- [62] A. Saxler, W. C. Mitchel, P. Kung, and M. Razeghi, *Appl. Phys. Lett.*, **74**, 2023 (1999).
- [63] T. G. Zhu, J. C. Denyszyn, U. Chowdhury, M. M. Wong, and R. D. Dupuis, *IEEE J. Sel. Top. Quant. Electron.*, **8**, 298 (2002).
- [64] Private communication, S. Leboeuf, G. E. Corporate Research and Development.
- [65] M. A. Khan, J. N. Kuznia, D. T. Olson, J. M. Van Hove, M. Blasingame, and L. F. Reitz, *Appl. Phys. Lett.*, **60**, 2917 (1992).

- [66] M. A. Khan, J. N. Kuznia, D. T. Olson, M. Blasingame, and A. R. Bhattarai, *Appl. Phys. Lett.*, **63**, 2455 (1993).
- [67] Q. Chen, M. A. Khan, C. J. Sun, and J. W. Yang, *Electron. Lett.*, **31**, 1781 (1995).
- [68] B. Yang, T. Li, K. Heng, C. Collins, S. Wang, J. C. Carrano, R. D. Dupuis, J. C. Campbell, M. J. Schurman, and I. T. Ferguson, *IEEE J. Quant. Electron*, **36**, 1389 (2000).
- [69] W. Yang, T. Nohava, S. Krishankutty, R. Torreano, S. McPherson, and H. Marsh, *Appl. Phys. Lett.*, **73**, 978 (1998).
- [70] L. Chernyak, A. Osinsky, S. J. Pearton, and F. Ren, *Electron. Lett.*, **37**, 1411 (2001).
- [71] C. H. Chen, H. Liu, D. Steigerwald, M. Imler, C. P. Kuo, and M. G. Craford, *J. Electron. Mat.*, **25**, 1004 (1996).
- [72] T. Li, D. J. H. Lambert, A. L. Beck, C. J. Collins, B. Yang, M. M. Wong, U. Chowdhury, R. D. Dupuis, and J. C. Campbell, *Electron. Lett.*, **36**, 1581 (2000).
- [73] D. Walker, V. Kumar, K. Mi, P. Sandvik, P. Kung, X. H. Zhang, and M. Razeghi, *Appl. Phys. Lett.*, **76**, 403 (2000).
- [74] C. Pernot, Akira Hirano, M. Iwaya, T. Detchprohm, H. Amano, and I. Akasaki, *Jpn. J. Appl. Phys.*, **39**, L387 (2000).

- [75] J. D. Brown, J. Li, P. Srinivasan, J. Matthews, and J. F. Schetzina, *MRS Internet J. Nitride Semicond. Res.*, **5**, 9 (2000).
- [76] D. Pulfrey, J. J. Kuek, M. P. Leslie, B. D. Nener, G. Parish, U. K. Mishra, P. Kozodoy, and E. J. Tarsa, *IEEE Trans. Electron. Dev.*, **48**, 486 (2001).
- [77] D. J. H. Lambert, M. M. Wong, U. Chowdhury, C. Collins, T. Li, H. K. Kwon, B. S. Shelton, T. G. Zhu, J. C. Campbell, and R. D. Dupuis, *Appl. Phys. Lett.*, **77**, 1900 (2000).
- [78] S. Nakamura, T. Mukai, and M. Senoh, *Appl. Phys. Lett.*, **64**, 1687 (1994).
- [79] S. Nakamura, T. Mukai, and M. Senoh, *J. Appl. Phys.*, **76**, 8189 (1994).
- [80] S. Nakamura, *Microelec. J.*, **25**, 651 (1994).
- [81] S. Nakamura, M. Senoh, N. Iwasa, and S. Nagahama, *Jpn. J. Appl. Phys.*, **34**, L797 (1995).
- [82] S. Nakamura, M. Senoh, N. Iwasa, S. Nagahama, T. Yamada, and T. Mukai, *Jpn. J. Appl. Phys.*, **34**, L1332 (1995).
- [83] Y. K. Song, M. Diagne, H. Zhou, A. V. Nurmikko, R. P. Schneider, Jr., and T. Takeuchi, *Appl. Phys. Lett.*, **77**, 1744 (2000).
- [84] M. Diagne, Y. He, H. Zhou, E. Makarona, A. V. Nurmikko, J. Han, K. E. Waldrip, J. J. Figiel, T. Takeuchi, and M. Krames, *Appl. Phys. Lett.*, **79**, 3720 (2001).

- [85] I. Ozden, E. Makarona, A. V. Nurmikko, and T. Takeuchi, *Appl. Phys. Lett.*, **79**, 2532 (2001).
- [86] G. Coli, K. K. Bajaj, J. Li, J. Y. Lin, and H. X. Jiang, *Appl. Phys. Lett.*, **78**, 1829 (2001).
- [87] T. Nishida, H. Saito, and N. Kobayashi, *Appl. Phys. Lett.*, **78**, 399 (2001).
- [88] T. Nishida, H. Saito, and N. Kobayashi, *Appl. Phys. Lett.*, **78**, 3927 (2001).
- [89] A. Kinoshita, H. Hirayama, M. Ainoya, Y. Aoyagi, and A. Hirata, *Appl. Phys. Lett.*, **77**, 175 (2000).
- [90] M. Shatalov, J. Zhang, A. S. Chitnis, V. Adivarahan, J. Yang, G. Simin, and M. A. Khan, *IEEE J. Sel. Top. Quant. Electron.*, **8**, 302 (2002).
- [91] M. Shatalov, A. Chitnis, V. Adivarahan, A. Lunev, J. Zhang, J. W. Yang, Q. Farid, G. Simin, A. Zakheim, and M. A. Khan, *Appl. Phys. Lett.*, **78**, 817 (2001).
- [92] A. Chitnis, J. P. Zhang, V. Adivarahan, W. Shuai, J. Sun, M. Shatalov, J. W. Yang, G. Simin, and M. A. Khan, *Jpn. J. Appl. Phys.*, **41**, L450 (2002).
- [93] V. Adivarahan, J. Zhang, A. Chitnis, W. Shuai, J. Sun, R. Pachipulusu, M. Shatalov, and M. A. Khan, *Jpn. J. Appl. Phys.*, **41**, L435 (2002).
- [94] J. P. Zhang, H. M. Wang, M. E. Gaevski, C. Q. Chen, Q. Fareed, J. W. Yang, G. Simin, and M. A. Khan, *Appl. Phys. Lett.*, **80**, 3542 (2002).

- [95] M. Shatalov, G. Simin, V. Adivarahan, A. Chitnis, S. Wu, R. Pachipulusu, V. Mandavilli, K. Simin, J. P. Zhang, J. W. Yang, and M. A. Khan, *Jpn. J. Appl. Phys.*, **41**, 5083 (2002).
- [96] S. Nakamura, M. Senoh, S. Nagahama, N. Iwasa, T. Yamada, T. Matsushita, H. Kiyoku, and Y. Sugimoto, *Jpn. J. Appl. Phys.*, **35**, L74 (1996).
- [97] I. Akasaki, S. Sota, H. Sakai, T. Tanaka, M. Koike, and H. Amano, *Electron. Lett.*, **32**, 1105 (1996).
- [98] M. P. Mack, A. Abare, M. Aizcorbe, P. Kozodoy, S. Keller, U. K. Mishra, L. Coldren and S. DenBaars, *MRS Internet J. Nitride Semicond. Res.*, **2**, 41 (1997).
- [99] K. Itaya, M. Onomura, J. Nishio, L. Sugiura, S. Saito, M. Suzuki, J. Rennie, S. Nunoue, M. Yamamoto, *Jpn. J. Appl. Phys.*, **35**, L1315 (1996).
- [100] G. E. Bulman, K. Doverspike, S. T. Sheppard, T. W. Weeks, H. S. Kong, H. M. Dieringer, J. A. Edmont, J. D. Brown, J. T. Swindell, and J. F. Schetzina, *Electron. Lett.*, **33**, 1556 (1997).
- [101] S. Nagahama, T. Yanamoto, M. Sano, and T. Mukai, *Jpn. J. Appl. Phys.*, **40**, L785 (2001).
- [102] S. Nagahama, T. Yanamoto, M. Sano, and T. Mukai, *Jpn. J. Appl. Phys.*, **40**, L788 (2001).

- [103] “*The Metallorganic Chemical Vapor Deposition of III-V Nitrides for Optoelectronic Device Applications*”, Paul A. Grudowski, University of Texas, Doctoral Dissertation, 2000.
- [104] P. A. Grudowski, C. J. Eiting, J. Park, B. S. Shelton, D. J. H. Lambert, and R. D. Dupuis, *Appl. Phys. Lett.*, **71**, 1537 (1997).
- [105] J. C. Carrano, P. A. Grudowski, C. J. Eiting, R. D. Dupuis, and J. C. Campbell, *Appl. Phys. Lett.*, **70**, 1992 (1997).
- [106] B. S. Shelton, M. M. Wong, T. G. Zhu, C. J. Eiting, D. J. H. Lambert, D. E. Lin, H. K. Kwon, and R. D. Dupuis, *Phys. Stat. Sol. (a)*, **176**, 213 (1999).
- [107] J. C. Carrano, D. J. H. Lambert, C. J. Eiting, C. J. Collins, T. Li, S. Wang, B. Yang, A. L. Beck, R. D. Dupuis, and J. C. Campbell, *Appl. Phys. Lett.*, **76**, 924 (2000).
- [108] B. S. Shelton, J. J. Huang, D. J. H. Lambert, T. G. Zhu, M. M. Wong, C. J. Eiting, H. K. Kwon, M. Feng, and R. D. Dupuis, *Electron. Lett.*, **36**, 80 (2000).
- [109] E. D. Readinger, S. E. Mohny, T. G. Pribicko, J. H. Wang, K. O. Schweitz, U. Chowdhury, M. M. Wong, R. D. Dupuis, M. Pophristic, and S. P. Guo, *Electron. Lett.*, **38**, 1230 (2002).

- [110] C. J. Collins, U. Chowdhury, M. M. Wong, B. Yang, A. L. Beck, R. D. Dupuis and J. C. Campbell, *Electron. Lett.*, **38**, 824 (2002).
- [111] U. Chowdhury, M. M. Wong, C. J. Collins, B. Yang, J. C. Denyszyn, J. C. Campbell, and R. D. Dupuis, accepted for publication in *J. Cryst. Growth*.
- [112] Private communication, M. Reine, BAE Sysetms.

# Vita

Uttiya Chowdhury was born in Chittagong, Bangladesh, on May 11, 1972, son of Urna Chowdhury and Dr. Tapan K. Chowdhury. After graduating with honors from Chittagong College in 1989, he enrolled at Bangladesh University of Engineering and Technology to study electrical and electronic engineering. After graduation with the degree of B.Sc.Engg., he joined Spectrum Engineering Consortium, a software company in Bangladesh as a Junior Programmer. He enrolled in the Graduate School at The University of Texas at Austin in the fall of 1997. At the same time, he also joined Dr. Russell Dupuis' MOCVD group as a graduate research assistant. He earned his M.S. degree from the University of Texas at Austin in December 1999 and proceeded on to doctoral studies in the same research group.

Permanent Address: The Chowdhury Residence

North Dhemsha, Satkania

Chittagong, BANGLADESH

This dissertation was typeset with L<sup>A</sup>T<sub>E</sub>X 2<sub>ε</sub> by the author.